INFLUENCE OF SURFACE WETTABILITY ON DROP DYNAMICS AND CONDENSATION

A Dissertation

Presented to the Faculty of the Graduate School

of Cornell University

in Partial Fulfillment of the Requirements for the Degree of

Doctor of Philosophy

by

Jonathan Michael Ludwicki

August 2020

© 2020 Jonathan Michael Ludwicki

ALL RIGHTS RESERVED

INFLUENCE OF SURFACE WETTABILITY ON DROP DYNAMICS AND CONDENSATION

Jonathan Michael Ludwicki, Ph.D.

Cornell University 2020

The ability of a liquid to wet a solid substrate is determined by the chemistry and physical texturing of the surface. At the two theoretical extremes, a liquid drop on a surface can completely spread to a film or bead to a perfect sphere. In practice, some form of intermediate or partial wetting is obtained with the liquid adopting a spherical cap shape. Two metrics are commonly employed to specify the surface wettability: rest or static contact angle (θ_0) and contact angle hysteresis ($\Delta\theta$). Partially non-wettable surfaces are characterized by static contact angles $\theta_0 > 90°$ while partially wettable surfaces have $\theta_0 < 90°$. Contact angle hysteresis, defined as the difference in dynamic advancing and receding contact angles, specifies contact line stick-slip behavior with higher hysteresis corresponding to a greater extent of contact line pinning. Understanding how liquids wet and dynamically behave on solid surfaces has widespread importance in application areas ranging from natural to industrial to technological. As such, it has historically attracted much scientific attention. This dissertation studies how surface wettability influences drop behaviors in the interrelated areas of coalescence, condensation heat transfer, and inertial-capillary (rapid) spreading.

In the first part of this dissertation, experiments and numerical simulations are employed to examine how changing the surface wettability, via modification of θ_0 & $\Delta\theta$, influences sweeping during sessile drop coalescence. Coalescence

sweeping results from the dynamic shape reconfiguration associated with the drop merging process and has relevance to self-cleaning, anti-frost, condensation, and water harvesting applications. In the second part of this dissertation, a surface with switchable superhydrophilic to hydrophobic wetting behavior is developed that responds to temperature stimulus. This surface is successfully applied as a condenser that exhibits variable performance in its heat transfer coefficient by switching between the filmwise and dropwise modes of condensation, with ultimate relevance to space-based thermal management applications. Theory is also applied to understand how surface wettability affects fundamental drop processes during dropwise condensation, and to elucidate dropwise to filmwise condensation transitions. Finally, in the third part of this dissertation, a contact line mobility parameter is hypothesized as a means to understand and predict liquid spreading in situations where inertia and capillarity compete. Drop vibration experiments will be performed on the International Space Station (ISS) in 2020 to measure the mobility parameter, and subsequent drop-drop coalescence experiments will examine the utility of the mobility parameter as a predictive tool. ISS microgravity manifests a magnified capillary length scale which transforms the inertial-capillary spreading problem from a small and fast event on Earth to one that is larger and slower in space thereby enabling easier characterization. Preliminary results are reported for an analogous ground-based study that assesses the validity of mobility parameter utilization for predictive application.

BIOGRAPHICAL SKETCH

Jonathan Ludwicki was raised outside of Rochester, NY in the Village of Churchville. During his junior year at the Churchville-Chili Senior High School he was awarded the Rensselaer Medal and Scholarship which recognizes superlative academic achievement in science, engineering, and technology. With the generous funding provided by the Rensselaer Medal, he attended the Rensselaer Polytechnic Institute in Troy, NY where he graduated *summa cum laude* with a Bachelor of Science Degree in Chemical Engineering. After working two years in the semiconductor industry, he returned to school at Cornell University in Ithaca, NY to pursue a Doctor of Philosophy Degree in Chemical Engineering. During his time at Cornell University, he was honored as a NASA Space Technology Research Fellow and performed work in the areas of fluid mechanics, heat transfer, and surface engineering under the advisement of Professor Paul H. Steen.

This doctoral dissertation is dedicated to my parents who have always encouraged me to drive the bus.

ACKNOWLEDGEMENTS

To my parents, John and Susan Ludwicki, thank you for the positive example you set. I have learned many things from you that have benefited me throughout my life and made me successful in graduate school. I am lucky to have such a constant and loving support system.

To my wife, Morgan Baltz Ludwicki, I cannot think of anyone better to have spent my years in Ithaca with. Thank you for helping me to become more healthy and efficient in my working habits. You showed me the importance of work-life balance, and I am better for it. Cheers to the years ahead!

To my lifelong friend, Keith Prouty, thank you for pushing me to apply to graduate school and motivating me to power through the applications when I doubted myself. The Dr. J jersey can finally be displayed with pride!

To my academic advisor, Paul H. Steen, thank you for giving me the freedom to explore many areas of research, especially those that fell more outside your areas of expertise. I am also greatly appreciative of your present but non-overbearing mentoring style which was critical to my success.

To my NASA research collaborator, Franklin L. Robinson (aka The Sensei of Goddard), thank you for welcoming me into your lab and teaching me about things ranging from vacuum pumps to Swagelok fittings. You were always unselfish with your time and it was of great benefit to the success of my research.

Finally, I am grateful for the generous funding and NASA facility access provided by the NASA Space Technology Research Fellowship Program (NASA Award #80NSSC17K0144). I also acknowledge National Science Foundation (NSF) Award #1637960 which provided financial support for future experiments to be run on the International Space Station, and Glenn Swan for his assistance with hardware fabrication related to this project.

TABLE OF CONTENTS

Biographical Sketch . . . iii
Dedication . . . iv
Acknowledgements . . . v
Table of Contents . . . vi
List of Tables . . . ix
List of Figures . . . xi
Preface . . . xvii

1 Sweeping by Sessile Drop Coalescence **1**
1.1 Abstract . . . 1
1.2 Introduction . . . 2
1.3 Numerical Method . . . 6
1.3.1 Simulation Perspective . . . 6
1.3.2 Volume of Fluid Formulation . . . 6
1.3.3 Dynamic Contact Angle Model . . . 8
1.3.4 Computational Domain and Procedure . . . 9
1.4 Characteristic Scales and Non-Dimensional Numbers . . . 11
1.5 Sweeping Metrics . . . 12
1.6 Mechanical Energy Balance . . . 12
1.7 Results and Discussion . . . 15
1.7.1 Model Validation . . . 15
1.7.2 Parametric Study . . . 17
1.8 Concluding Remarks . . . 24

2 Sweeping by Sessile Drop Coalescence. Part 2: Effect of Contact Angle Hysteresis **28**
2.1 Abstract . . . 28
2.2 Introduction . . . 29
2.3 Numerical Method . . . 32
2.4 Sweeping Metrics and Energy Accounting . . . 33
2.5 Results and Discussion . . . 35
2.5.1 Parametric Study . . . 35
2.5.2 Modes of Sweeping . . . 36
2.5.3 Swept Areas and Extensions . . . 39
2.5.4 Wetted versus Projected Sweeping . . . 40
2.5.5 Jumping and Non-Jumping Regimes . . . 42
2.6 Concluding Remarks . . . 43

3 Switchable Wettability for Condensation Heat Transfer **46**
3.1 Abstract . . . 46
3.2 Introduction . . . 46
3.3 Surface Fabrication . . . 49

3.4 Condensation Experiment 51
3.5 Results and Discussion 54
3.6 Conclusions 56

4 How Surface Wettability Affects Fundamental Drop Processes during Dropwise Condensation 58
4.1 Abstract 58
4.2 Introduction 59
4.3 Drop Nucleation, Growth, and Departure 61
4.4 Dropwise Condensation Heat Transfer Modeling 65
4.5 Conclusions and Future Work 68

5 Catastrophe Theory Model of the Transition from Dropwise to Filmwise Condensation 69
5.1 Abstract 69
5.2 Introduction 70
5.3 Potential Function 72
5.4 Comparison to Experiments 79
5.5 Conclusions and Future Work 80

6 Unmasking Contact Line Mobility for Inertial-Capillary Spreading using Drop Vibration and Coalescence 81
6.1 Abstract 81
6.2 Introduction 82
6.3 The ISS Advantage 85
6.4 Technical Impacts 87
6.5 ISS Experiments 89
6.6 Expected Outcomes and Future Outlook 91

7 Is Mobility a Material-Like Parameter? 95
7.1 Abstract 95
7.2 Introduction 95
7.3 Experimental Method and Numerical Model 100
7.4 Results and Discussion 104
7.4.1 Limits of the Davis-Hocking Model 104
7.4.2 Experiment versus Simulation 105
7.4.3 Commentary 109
7.5 Conclusion 111

8 Future Directions 112
8.1 Sessile Drop Coalescence and Sweeping 112
8.2 Condensation Heat Transfer and Switchable Wettability 114

A Appendix for Chapter 1 **115**
A.1 Effect of Artificial Interface Compression in OpenFOAM 115
A.2 Description of Supplemental Videos 115

B Appendix for Chapter 2 **117**
B.1 Dimensional Analysis of Sessile Drop Coalescence 117

C Appendix for Chapter 3 **119**
C.1 Condensation Chamber 119
C.2 Flow Loop 121
C.3 Condensation Operational Procedure 122
C.4 Uncertainty Analysis 123
C.5 Electrical Potential-Responsive Wettability 124

D Appendix for Chapters 6 & 7 **127**
D.1 Dynamic Contact Angle Models 127

E Data Archiving for Federal Grants **130**

LIST OF TABLES

1 Wetting terminology utilized in this dissertation. xviii

1.1 Simulation fluid properties: water (subscript l) and air (subscript g). 9
1.2 Experimental surfaces (chemistry, roughness) and wettability by water: initial contact angle θ_0, advancing θ_a, receding θ_r, and contact angle hysteresis $\Delta\theta$. 15
1.3 Simulation parameters: surface wettability angles θ_0, θ_a, θ_r, and $\Delta\theta$; initial diameter D; characteristic velocity u_{ch}; Reynolds Re, Ohnesorge Oh, and Capillary Ca numbers. 18

2.1 Fluid properties of water, subscript l, and air, subscript g, used in the simulations: density (ρ), viscosity (μ), and surface tension (σ). 32
2.2 Simulation parameters: surface wettability θ_0 and $\Delta\theta$; initial drop diameter D. Advancing and receding contact angles are, respectively, $\theta_a = \theta_0 + 5°$ and $\theta_r = \theta_a - \Delta\theta$. 36

3.1 Chemical composition of the polymerization solution used to synthesize the surface-grafted PNIPAAm brushes via ARGET-ATRP. The reaction was performed at room temperature. 49

4.1 Parameter values used to analytically model the steam dropwise condensation heat transfer behavior of Miljkovic et al. (2013). The rightmost column justifies the choice of each parameter value. 66

6.1 Experimental surfaces and water contact angle data. 90

7.1 Coalescence as a test of the mobility parameter: comparison to alternative drop-surface experiments with inertial-capillary contact line motions. 100
7.2 Experimental surfaces and wettability by water: initial θ_0, advancing θ_a, and receding θ_r contact angles, contact angle hysteresis $\Delta\theta$, and mobility M. 101
7.3 Simulation fluid properties: water (subscript l) and air (subscript g). 102
7.4 Non-dimensional characterization: Reynolds ($Re = \rho_l U_{CL} D/\mu_l$), Capillary ($Ca = \mu_l U_{CL}/\sigma_{lg}$), and Ohnesorge ($Oh = \mu_l/\sqrt{\rho_l \sigma_{lg} D}$) numbers for the simulations of binary sessile drop coalescence. Note that, here, U_{CL} is the maximum magnitude of contact line velocity in the x-axis for $y = 0$ and $z = 0$. 103
7.5 Davis-Hocking model limits: range of U_{CL} values that produce a valid dynamic contact angle where $0° \leq \theta \leq 180°$ for the parameter values presented in Table 7.2. 105

7.6 Cumulative projected swept areas (normalized): experiment versus simulation. 109

B.1 Simulation parameters relevant to the three cases of sessile drop coalescence reported in Figure B.1. In all cases, $\theta_0 = 141°$, $\Delta\theta^+ = 5°$, and $\Delta\theta^- = 10°$. 118

LIST OF FIGURES

1 Traditional diagram for contact line behavior: dynamic contact angle θ plotted against contact line velocity U_{CL}. Contact line stick (i.e. $U_{CL} = 0$) occurs for $\theta_r < \theta < \theta_a$. Starting from a static configuration, the contact line begins to advance or recede at contact angle θ_a or θ_r, respectively. Marginally different contact angles are obtained by instead slowing to a static configuration, denoted $\theta_{a'}$ and $\theta_{r'}$. xix

2 (a) Number of yearly publications on the topic of 'textured surfaces', per Web of Science. (b) Wettability behavior for various solid-water-air systems. The red dashed line indicates the boundary of $\Delta\theta$ versus θ_0 assuming $\theta_0 \equiv (\theta_a + \theta_r)/2$. xx

3 Static, near-static, and dynamic wetting regimes investigated in this dissertation. xxi

1.1 a) Sessile drop: initial contact angle $\theta_0 > 90°$, projected $\mathcal{P}$ and wetted $\mathcal{W}$ contact areas. b) Projected view (top) of coalescing drops $A - A'$ with cumulative swept area (dashed) just reaching drop B, perhaps initiating another coalescence. 2

1.2 Instantaneous projected $\mathcal{P}(t)$ (top row) and wetted $\mathcal{W}(t)$ (bottom row) swept areas, with cumulative projected $\mathcal{P}_\infty$ (top right) and wetted $\mathcal{W}_\infty$ (bottom right) swept areas. Circles on the silhouettes (red dashed) represent the initial areas. 3

1.3 Computational domain: flow is bounded by symmetry, open-flow, and solid contact boundaries. At the moving contact line, the Kistler model is implemented, Equations 1.6, 1.7, and 1.8, sketched (lower right) and showing stick for $\theta_r \leq \theta \leq \theta_a$ and slip otherwise. 9

1.4 Experimental setup (side view): liquid fed drop (left) grows until it touches a pre-positioned drop (right), initiating the coalescence event. 16

1.5 Validation: simulation (solid line) and experiment (markers) for three runs each (triangle, circle, and square markers) and three surfaces (Table 1.2). Projected swept areas, for experiment $\mathcal{P}^*_e$ and simulation $\mathcal{P}^*_s$, as listed. No fitting parameters. 16

1.6 Swept areas (squares) and maximum extensions (x, circles; y, triangles), as influenced by wettability θ_0, with guide (solid fit lines). Binary free drop coalescence case (white dashed). Regimes: hydrophobic (blue) and superhydrophobic (green). . . 19

1.7 Cumulative swept areas: wetted $\mathcal{W}_\infty$ (thick dashed) and projected $\mathcal{P}_\infty$ (thick solid), with initial wetted (thin dashed) and initial projected (thin solid) areas, for reference. All areas are scaled, for comparison. 20

1.8 Evolution (left) of kinetic energy $\mathcal{K}^*$ and change in interfacial energy $\Delta\mathcal{A}^*$. Evolution (right) of total plane-normal momentum p_{y+} (y-component in positive y-direction). 21
1.9 Evolution of cumulative energy losses: bulk viscous $\overline{\mathcal{D}}^*_\mu$ (left) and contact line $\overline{\mathcal{D}}^*_\theta$ (right) contributions to the overall dissipation $\overline{\mathcal{D}}^* = \overline{\mathcal{D}}^*_\mu + \overline{\mathcal{D}}^*_\theta$. 21
1.10 Evolution of net swept areas: projected $\mathcal{P}^{**}$ (left) and wetted $\mathcal{W}^{**}(\mathcal{W}_0/\mathcal{P}_0)$ (right). Solid circles indicate drop jumping, at which wetted trajectories terminate (extensions, dashed). 23

2.1 Evolution of wetted (blue) and projected (black) swept areas during binary sessile drop coalescence, resulting in wetted $\mathcal{W}_\infty$ and projected $\mathcal{P}_\infty$ cumulative swept areas (right). Wetted footprints are indicated by the dashed blue lines overlaying the bulk dynamics. 30
2.2 3D computational domain with boundaries (solid contact, open-flow, or symmetry) as indicated. 33
2.3 Definition sketch: maximum x- and y-axis extensions of the wetted (subscript w) and projected (subscript p) cumulative swept areas. 34
2.4 (a) Ratio of extensions, $max(y_p)/y_{p,f}$, for various θ_0 and $\Delta\theta$. Bulk dynamics-dominated sweeping = • symbol, final rest state-dominated sweeping = – symbol. (b) Dissipation fraction of the total interfacial energy release, $|\overline{\mathcal{D}}/\Delta\mathcal{A}|$, in time for $\theta_0 = 131°$. . . . 37
2.5 Effect of surface wettability, θ_0 & $\Delta\theta$, on swept areas and extensions: (a) net projected swept area $\mathcal{P}^{**}$, (b) regularized net wetted swept area $\mathcal{W}^{**}(\mathcal{W}_0/\mathcal{P}_0)$, (c) maximum projected extensions, and (d) maximum wetted extensions. 38
2.6 Cumulative swept areas for (θ_0, $\Delta\theta$): wetted $\mathcal{W}_\infty$ (thick dashed) and projected $\mathcal{P}_\infty$ (thick solid), with initial wetted (thin dashed) and initial projected (thin solid) areas, for reference. All areas are scaled, for comparison. 41
2.7 Ratio of wetted and projected areas: (a) cumulative $\mathcal{W}_\infty/\mathcal{P}_\infty$ and (b) net $(\mathcal{W}_\infty - \mathcal{W}_0)/(\mathcal{P}_\infty - \mathcal{P}_0)$. 42
2.8 Regime boundaries: i) modes of coalescence sweeping, as separated by the red line. ii) jumping versus non-jumping coalescence, as separated by the shaded (gray) and non-shaded regions. 43

3.1 Structural formula of PNIPAAm and its reversible conformation changes below and above the LCST. 47
3.2 Switchable wettability: (top left) pure spreading, below the LCST. (top right) hydrophobicity, above the LCST. (bottom) reversibility of the water contact angle below, 25°C, and above, 50°C, the LCST. 50

3.3 Condensation chamber schematic: flow loop with sample section housed inside a vacuum enclosure. Resistance temperature detector (RTD) probes (Class 1/10DIN, Omega Engineering Inc.) measure T_{in} and T_{out}, an integrated flow meter (104-8, McMillan Co.) measures $\dot{Q}$, and a chamber pressure sensor (UNIK 5000, Druck Ltd.) measures the vapor saturation pressure which is then converted to T_s using a best-fit polynomial to experimental data[1]. Electrical outputs from the measurement devices are sent to a digital multimeter operated at 6½-digit resolution (PXIe-4081, National Instruments Co.) for data acquisition. 52
3.4 Switchable condensation: (left) filmwise condensation, below the LCST. (right) flooded dropwise condensation, above the LCST. Same scale bar as at left. 54
3.5 Switchable condensation: h versus q'' for temperatures above (• symbol) and below (◦ symbol) the LCST. The dashed line is the Nusselt model for filmwise condensation on a horizontally-oriented tube. 55

4.1 Single drop heat flux (q'') versus drop radius (R) for various static contact angles at $\Delta T = 1°C$, $\delta = 1$ μm, $k_{coat} = 0.2$ W/m·K, $k_l = 0.68$ W/m·K, $h_{\dot{m}} = 15.7$ MW/m^2·K, and $r_{min} = 20$ nm. 60
4.2 Drop nucleation rate (J) versus static contact angle (θ_0) for steam condensation (pressure = 1 bar) at various surface temperatures (0 °C, 20 °C, and 40 °C). 62
4.3 Single drop growth rate (G) versus drop radius (R) for various static contact angles at $\Delta T = 1°C$, $\delta = 20$ nm, $k_{coat} = 0.2$ W/m·K, $k_l = 0.68$ W/m·K, $\rho_l = 959$ kg/m^3, $h_{\dot{m}} = 15.7$ MW/m^2·K, $r_{min} = 20$ nm, and $h_{fg} = 2.26$ MJ/kg. 63
4.4 Drop departure size ($\hat{r}$) versus contact angle hysteresis ($\Delta\theta$) for various static contact angles with $\rho_l = 998$ kg/m^3, $g = 9.81$ m/s^2, and $\sigma_{lv} = 0.072$ J/m^2. 64
4.5 Analytical dropwise condensation heat transfer modeling results. Red solid line: model behavior versus experimental data reported in the literature. Green solid line: predicted enhancements in condensation heat transfer with $\theta_0 = 90°$ and $\Delta\theta = 0.1°$. Figure adapted from Cho et al. (2016). 67

5.1 A typical heat transfer curve for a condensation phase change process plotting heat flux (q'') versus surface subcooling (ΔT). The various heat transfer regimes associated with Labels A, B, C, and D are pictorially depicted below the plot. Gravity vector $\boldsymbol{g}$ is also labeled. 71

5.2 Condensation heat transfer curves showing (left) smooth and (right) abrupt transitions from the dropwise to filmwise mode. Labels A, B, C, and D correspond to the regimes identified in Figure 5.1. Sketch based on the experimental observation of Utaka et al. (1988). 71
5.3 The evolving potential function U for p = 0 and q = [-2, 2] illustrating a smooth response in $x \equiv \Delta T - \Delta T_0$. 75
5.4 The evolving potential function U for p = 2 and q = [-2, 2] illustrating a catastrophic response in $x \equiv \Delta T - \Delta T_0$. 76
5.5 (p = 0 case) As the control parameter q is smoothly varied, there is a smooth response in x. 77
5.6 (p = 2 case) As the control parameter q is smoothly varied, there is a catastrophic response in x. 77
5.7 Two views of the equilibrium surface for the derived potential function showing the characteristic pleat for a cusp-type catastrophe. The red dots are unstable, while the blue dots are stable equilibria. 78
5.8 (left) MATLAB and (right) AUTO plots of the projecting curve in the q-p plane showing the three-solution bifurcation regime. The AUTO plot confirms the equilibrium curve presented in Figure 5.7. 78
5.9 Experimental condensation heat transfer curves for a polytetrafluoroethylene coated surface showing (left) smooth and (right) abrupt transitions from the dropwise to filmwise modes. Condensing vapor is propylene glycol at saturation temperature $T_{sat} \approx 365K$. Data from Utaka et al. (1988). 79
5.10 Potential function-predicted condensation heat transfer curves showing (left) smooth and (right) abrupt transitions from the dropwise to filmwise modes. 79

6.1 Small gap (< 1 mm) applications having inertial-capillary spreading: (left) immersion lithography with advancing and receding contact lines, wherein the wafer scans at speeds nearly 1 m/s underneath the immersion liquid. Figure from Clarke et al. (2006); (right) planar flow melt-spinning with an advancing contact line, wherein liquid metal solidifies against a substrate moving at speeds upwards of 10 m/s. 83
6.2 Contact line disturbances: (left) induced by support-normal oscillation; (right) induced by coalescence of drop A and drop B, evolving to a final shape (shadow). 84
6.3 Water blobs under low gravity conditions during a parabolic flight. These liquid shapes are unearthly in that they are held by surface tension at exceptionally large scales due to the increased capillary length. Images from Weislogel and Lichter (1998). . . . 86

6.4 Additional applications with inertial-capillary contact line motion: (left) drop impact on a substrate yields different splat patterns depending on Weber number, relevant to crime scene forensics and ink-jet printing (scale bar = 1 cm). Image from Hulse-Smith and Illes (2007); (middle) dropwise condensation on a cold plate, relevant to phase change heat transfer (1 x 1 cm view); (right) a solid sphere (2.54 cm diameter) enters a liquid bath from air, relevant to immersion coating processes. Image from Aristoff et al. (2010). 88
6.5 Vibration experiment setup: a sinusoidal input signal drives the mechanical shaker as a high-speed camera images dynamic drop shapes for analysis. Figure from Xia and Steen (2018). 89
6.6 ISS sessile drop coalescence simulations: y_p^* & y_w^* versus t^* for four cases of sessile drop coalescence (Table 6.1, nos. 1 - 4). 92
6.7 Coalescence transients, simulation versus experiment, for identical water drops merging on a PDMS treated surface. The simulation employs a Davis-Hocking type dynamic contact angle model which utilizes the measured mobility parameter M. 94

7.1 Traditional dynamic contact angle θ response to contact line velocity U_{CL}. 96
7.2 3D computational domain for simulating binary sessile drop coalescence, with two symmetry planes as indicated. 102
7.3 Coalescence extensions and swept areas: evolution of the x-axis and y-axis projected extensions ($x_p(t)$ & $y_p(t)$, respectively) during sessile drop coalescence. The contact line position (dashed blue line) is superimposed on the top view coalescence dynamics. Instantaneous cumulative projected swept areas $\mathcal{P}(t)$ are indicated by the black silhouettes, with the final cumulative projected swept area $\mathcal{P}_\infty$ at the right. The circles on $\mathcal{P}_\infty$ (red dashed) represent the initial projected drop areas. 104
7.4 Family of contact angle models: (core) sketch of θ response to Ca for the Davis-Hocking, Kistler, and perfect slip models, no contact angle hysteresis case. (perimeter) model response, incorporating contact angle hysteresis, for the four surfaces investigated in this study. The corners, red squared, indicate model behavior for the Ca range probed by the simulations. 106
7.5 Comparison of side view coalescence dynamics (x-z plane): experiments (left) versus simulations (right). The Davis-Hocking model is represented by the blue line, while the Kistler model by the orange line. Scale bar (red line) is 0.5 mm in all cases. 107

7.6 Time evolution of projected extensions: experiments (open circles) versus simulations (solid lines). The Davis-Hocking model is represented by the blue lines, while the Kistler model by the orange lines. 108

8.1 Top-view time progressions of sessile drop coalescence during steam dropwise condensation onto a quartz surface vapor silanized with dodecyltrichlorosilane ($\theta_0 \sim 100°$). Condenser surface temperatures are (top) 20 °C and (bottom) 50 °C. 112

A.1 Time response of the non-dimensional projected x-axis extension for the (left) unmodified interFoam solver with artificial anti-diffusive surface fluxes and (right) modified interFoam solver without artificial anti-diffusive surface fluxes. It is noted that the modified solver resolves the time lag between simulation and experiment. The system tested is Teflon-water-air where $\theta_0 = 110°$, $\theta_a = 120°$, and $\theta_r = 75°$. 115

B.1 Non-dimensional collapse in OpenFOAM: x_p^* & y_p^* versus t^* for three cases of sessile drop coalescence (Table B.1). 118

C.1 Experimental setup: condensation chamber and exterior equipment. 120
C.2 Condensation chamber interior: flow loop with sample section and temperature probes. 121
C.3 C1s XPS spectra*: (left) post-TESUD deposition and (right) post-aldehyde oxidation to carboxylic acid. 125
C.4 Water static wettability: copper surface coated with an electrical potential-responsive monolayer for two switching cycles. 126

PREFACE

Wetting and Engineered Surfaces

Wetting is the study of how liquids spread on a solid surfaces. When a capillary liquid drop is touched to a surface, it deforms and adopts a spherical cap shape with wettability characterized by a static contact angle θ_0. Liquids are described as partially wetting for $0° < \theta_0 < 90°$ and partially non-wetting for $90° < \theta_0 < 180°$ (Table 1). At the theoretical extremes, total wetting ($\theta_0 = 0°$) and total non-wetting ($\theta_0 = 180°$) can occur. The ability of a particular liquid to wet a solid is determined first by the surface chemistry of the solid. As specified by Young's relation[2], surface chemistries with higher free energies are more wettable while those with lower free energies are less so. Further, for a given surface chemistry, surface roughness (specifically, asperity geometry and scale) can enhance the degree of wetting or non-wetting by amplifying the material's intrinsic wettability[3]. For example, as roughness increases, a surface that starts as non-wettable can become super-non-wettable[4]. This understanding of wetting has enabled researchers to design solid surfaces with wettability tailored for specific applications. Such surfaces are formally defined as "engineered", "textured", and/or "structured"[5]. Specific examples of engineered surfaces include:

- Knife-like nanostructures covered with a fluorinated molecular coating for highly efficient jumping-drop condensation heat transfer[6]

- Biphilic micro- and nanostructures for site-selective drop nucleation to enhance fog collection during water harvesting processes[7]

- Micro-etched aluminum coated with polytetrafluoroethylene to promote the self-cleaning of drops for anti-icing systems[8]

Table 1: Wetting terminology utilized in this dissertation.

	$0° < \theta_0 < 90°$	$\theta_0 = 90°$	$90° < \theta_0 < 180°$
Liquids	Partially wetting	Neutrally wetting	Partially non-wetting
Solids	Partially wettable	Neutrally wettable	Partially non-wettable

Another important wettability metric for solid-liquid-gas systems is known as contact angle hysteresis. On real or non-ideal surfaces, a stationary liquid drop can exhibit a range of θ_0 values due to imperfections in the surface chemistry and/or roughness[9]. The angle at which a drop's line of contact begins to advance is known as the advancing contact angle θ_a. Analogously, the contact line begins to retract at a receding contact angle θ_r. The difference between these limiting angles is known as the contact angle hysteresis $\Delta\theta \equiv \theta_a - \theta_r$. Generally, larger $\Delta\theta$ values correspond to enhanced pinning of the contact line. In regards to anticipating static and near-static wetting behaviors, Louge recently outlined a statistical mechanics approach to contact line motion on rough surfaces where angles of advancement and recession can be predicted[10]. Specifically, the analysis indicated how the exemplary geometry of a bed of microscopic rods can be manipulated in pitch and size to create a wide range of contact angles and their hysteresis.

In cases of dynamic wetting, a liquid's line of contact traverses along a surface with contact line velocity U_{CL}. For advancing contact lines, $U_{CL} > 0$ and liquid displaces gas. Conversely, for receding contact lines, $U_{CL} < 0$ and gas displaces liquid. Contact line behavior is often depicted in a so-called 'traditional diagram' with dynamic contact angle θ plotted against U_{CL}, see Figure 1 for typical experimental results[11]. It is noted that for advancing and receding contact lines, it is always the case that $\partial\theta/\partial U_{CL} \geq 0$. Due to the broad relevance of dy-

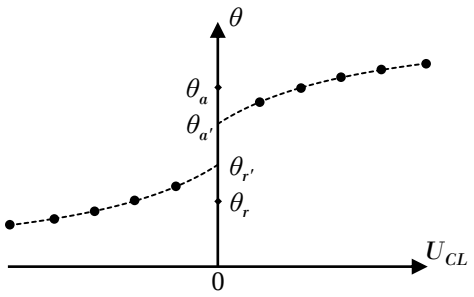

Figure 1: Traditional diagram for contact line behavior: dynamic contact angle θ plotted against contact line velocity U_{CL}. Contact line stick (i.e. $U_{CL} = 0$) occurs for $\theta_r < \theta < \theta_a$. Starting from a static configuration, the contact line begins to advance or recede at contact angle θ_a or θ_r, respectively. Marginally different contact angles are obtained by instead slowing to a static configuration, denoted $\theta_{a'}$ and $\theta_{r'}$.

namic wetting (e.g. in natural, industrial, and technological applications), numerous models have been developed to predict θ response to U_{CL} as highlighted in several reviews[12–14]. Existing models have basis in areas such as hydrodynamic theory, molecular dynamics, and/or experiment. Together, knowledge of static (θ_0), near-static ($\Delta\theta$), and dynamic (θ vs. U_{CL}) wetting behaviors allows for prediction of various drop-solid interactions.

Scope of Work

Over the past two-and-a-half decades, the number of studies published per year on engineered surfaces has increased exponentially with over 2,000 total papers published since 1995 (c.f. Figure 2a)[15]. That is to say, engineered surfaces are on the rise! With this, it is the case that most wettabilities (that is, combinations of θ_0 and $\Delta\theta$) are now realized, c.f. Figure 2b[6,16–31]. Many of these surfaces are targeted to areas that involve drop dynamics, with specific examples provided in the bulleted list on Page xvii. As a result, two cooperative needs have arisen in regards to informing surface design for application: experimental characterization of drop dynamics on engineered surfaces and ac-

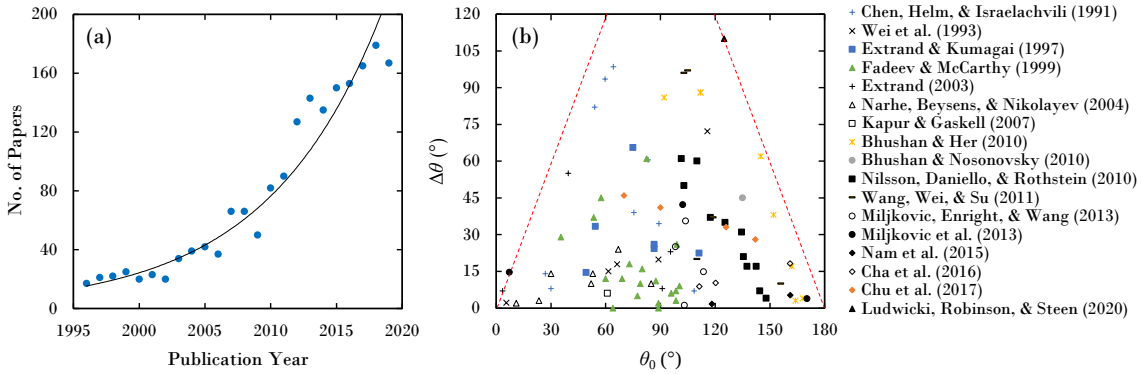

Figure 2: (a) Number of yearly publications on the topic of 'textured surfaces', per Web of Science. (b) Wettability behavior for various solid-water-air systems. The red dashed line indicates the boundary of $\Delta\theta$ versus θ_0 assuming $\theta_0 \equiv (\theta_a + \theta_r)/2$.

companying predictive modeling. As experimental results become available, simulations can be developed and verified to provide predictive capabilities for drop behaviors on engineered surfaces. Once valid models exist, simulations can be used to provide information not easily obtainable by the experimentalist (e.g. drop velocity fields or energy evolutions). Further, in cases where experiments may be difficult to run, simulations can be utilized instead of a lab-based study. Ultimately, by understanding the influence of surface wettability on drop dynamics, surfaces can be better designed for applications. This dissertation has a specific focus on surfaces engineered for condensation heat transfer applications, as motivated by the receipt of a NASA Space Technology Research Fellowship for work proposed in the area of thermal management. For condensation processes, fundamental drop dynamics of interest include nucleation, coalescence, and rapid wetting/dewetting, among others, as described below. Primarily, the drop dynamics studied in this work involve fast-moving contact lines on partially non-wettable surfaces where Reynolds number $Re \gg 1$ and Capillary number $Ca \ll 1$, c.f. Figure 3.

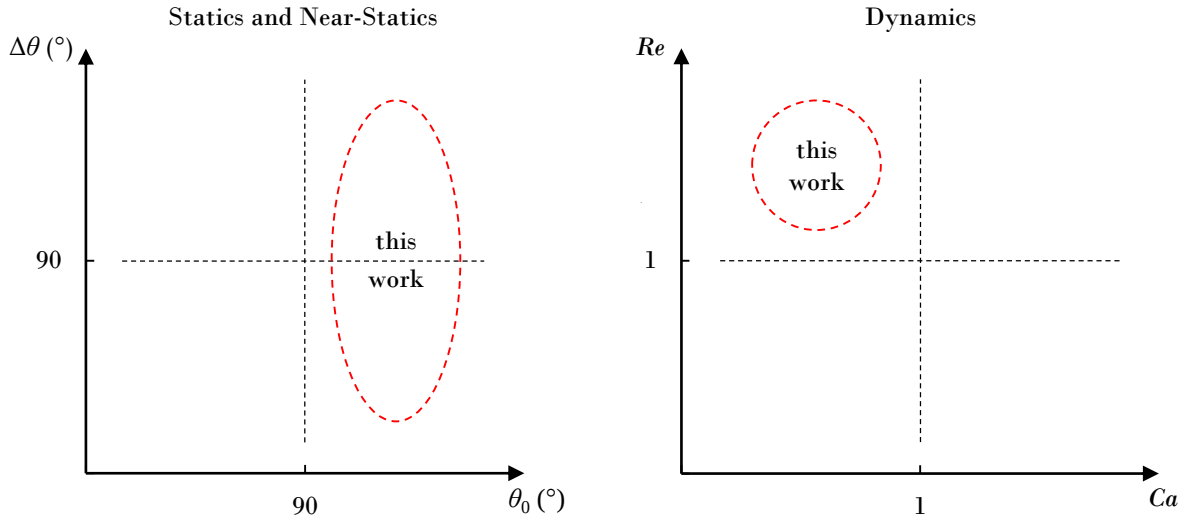

Figure 3: Static, near-static, and dynamic wetting regimes investigated in this dissertation.

Overview of Condensation Heat Transfer

Condensation is a phase change heat transfer process where vapor condenses to liquid on a cooled surface with a corresponding release of latent heat. Depending on the chemistry and physical texturing of the condensing surface, the mode of condensation evolves as either discrete drops or a continuous film[32]. It is well established that dropwise condensation can enhance the heat transfer coefficient by an order-of-magnitude compared with the filmwise mode[33]. This is because a continuous liquid film has much higher thermal resistance than a population of discrete drops[34]. Given that efficient condensation heat transfer processes are often preferred in practice, there have been numerous efforts to engineer condenser surfaces that promote and sustain the dropwise mode.

Dropwise condensation typically proceeds on surfaces classified as partially non-wettable or hydrophobic where the static contact angle θ_0 of the condensate is greater than 90°[35]. The minimum requirement for such non-wettable

surfaces is a low surface energy. For example, the lowest surface energy ever recorded (6.7 mJ/m^2 for regularly aligned closest hexagonal packed $-CF_3$ groups) gives $\theta_0 = 119°$ for a water drop on a flat and smooth surface[36]. To obtain larger θ_0 values, roughness is introduced so the effects of the surface chemistry can be amplified. On a roughened surface, liquid either wets the texturing (Wenzel state[37]) or is suspended above it (Cassie state[38]). Drops in the Wenzel state are more adherent to the surface and have higher contact angle hysteresis $\Delta\theta$ than those in the Cassie state[39]. Partially wetting drop morphologies (i.e. a mixed Cassie-Wenzel state[40]) can also exist.

During dropwise condensation, several drop processes occur simultaneously: nucleation, growth, and departure[41]. Freshly nucleated drops grow first by condensation, and once they become large enough coalescence dominates the growth until departure occurs[42]. In terrestrial environments drop departure is often promoted by gravity, with the departure size dependent on θ_0, $\Delta\theta$, and properties of the condensate[43]. As a drop departs, it slides along the surface and coalesces with additional drops in its path. This frees condenser surface area for renucleation which is an essential process in maintaining dropwise mode condensation[44]. Other means of inducing drop departure include surface energy gradients[45], temperature gradients[46], electrostatic potential gradients[47], surface vibrations[48], and jumping-drop ejection[49].

At any given time, the heat transfer characteristics of a dropwise condensation process are dictated by the number and size of drops on the surface[50]. This is because drops act as thermal resistance to heat transfer. Small drops have the highest heat fluxes, thus it is desirable to maximize their population to enhance heat transfer[51]. To accomplish this, larger drops must be frequently removed from the surface to provide area for the nucleation of small drops[52]. Besides

size, individual drop heat transfer is also affected by wetting morphology, static contact angle, and thermophysical properties of the condensation system[27]. With regards to dropwise condensation heat transfer, several open questions remain[53]:

- How does the role of surface design influence fundamental drop processes that occur during dropwise condensation (e.g. nucleation, coalescence, and departure)?
- What are the appropriate surface design guidelines for maximizing heat transfer during dropwise condensation?
- Can transitions from dropwise to filmwise condensation be predicted at a critical heat flux?
- Can condenser materials be found that avoid degradation and fouling during dropwise condensation operation?

Outline of Dissertation

This dissertation is organized as a series of relatively independent chapters that are written in the form of journal articles. Each chapter provides background and motivation related to the work, a description of the research and key results, and concludes with a discussion and future outlook.

Chapters 1 and 2 address the phenomenon of coalescence sweeping, whereby sessile drops combine and the dynamics of the merging process sweep surface area. The influence of initial contact angle is first investigated (Chapter 1), followed by the effects of contact angle hysteresis (Chapter 2). Conclusions describe how each wettability parameter specifies the extent of sweeping. Both experiments and numerical simulations are employed, with primary contributions to engineering.

Chapter 3 discusses work associated with a NASA Space Technology Research Fellowship. In this research, a surface was developed that exhibits switchable superhydrophilic to hydrophobic wetting behavior via a temperature stimulus. This surface was then successfully employed to manipulate the heat transfer coefficient during condensation processes, relevant to thermal management in condensing heat exchangers aboard spacecraft. This work is experimentally based with contributions to application.

Chapters 4 and 5 report the results of two additional projects on condensation heat transfer. Chapter 4 theoretically probes how surface wettability affects drop nucleation, growth, and departure during dropwise condensation to guide the design of more efficient condensers. Chapter 5 investigates transitions from dropwise to filmwise condensation at a critical heat flux by employing catastrophe theory. This analytical modeling has contributions to science.

Chapter 6 motivates drop vibration and coalescence experiments to be performed on the International Space Station (ISS) in 2020. The goal of this work is to elucidate inertial-capillary spreading processes, which are small-scale and fast on Earth, by exploiting the microgravity condition of the ISS. A contact line mobility parameter will be determined for several solid-liquid-gas systems to aid in predictions of rapid spreading. Chapter 7 reports the results of an analogous ground-based study where the utility of the mobility parameter is preliminarily assessed for drop coalescence processes via comparison of simulation to experiment. Contributions are to science and engineering.

Finally, Chapter 8 outlines additional future research directions not previously discussed in Chapters 1–7. For chapters with multiple authors, the individual author contributions are stated at the end of the chapter.

CHAPTER 1

SWEEPING BY SESSILE DROP COALESCENCE

(this Chapter is accepted for publication in *Eur. Phys. J. Special Topics: Challenges in Nanoscale Physics of Wetting Phenomena*[54])

1.1 Abstract

During coalescence of liquid drops contacting a solid, the liquid sweeps wetted and solid-projected areas. The extent of sweeping dictates the performance of devices such as self-cleaning surfaces, anti-frost coatings, water harvesters, and dropwise condensers. For these applications, weakly- and non-wetting solid substrates are preferred as they enhance drop dynamical behavior. Accordingly, our coalescence studies here are restricted to drops with contact angle $90° \leq \theta_0 \leq 180°$. Binary sessile drop coalescence is the focus, with volume of fluid simulations employed as the primary tool. The simulations, which incorporate a Kistler dynamic contact angle model, are first validated against three different experimental substrate systems and then used to study the influence of solid wettability on sweeping by modifying θ_0. With increasing θ_0 up to 150°, wetted and projected swept areas both increase as drop center of mass heightens. For $\theta_0 \geq 150°$, coalescence-induced drop jumping occurs owing to the decreasing wettability of the substrate and a focusing of liquid momentum due to the symmetry-breaking solid. In this regime, projected swept area continues to increase with θ_0 while wetted swept area reaches a maximum and then decreases. The sweeping results are interpreted using the mechanical energy balance from hydrodynamic theory and also compared to free drop coalescence.

1.2 Introduction

For coalescing capillary drops, liquid advances and recedes along a solid surface evolving complicated patterns of wetted and projected areas. Instantaneous wetted $\mathcal{W}$ is the area on the surface enclosed by the contact line, while instantaneous projected $\mathcal{P}$ is the area of an imaginary shadow cast from above by parallel projection of light onto the surface. Projected exceeds wetted area for drops on non-wetting and hydrophobic surfaces where initial contact angle $\theta_0 > 90°$, Figure 1.1a. There is recent interest in the behaviors of drops on surfaces where wetted and projected areas differ[55–59], including sessile drop coalescence. During sessile drop coalescence, two or more drops in contact with a surface merge to form a final drop. This is a dynamic event where the liquid exhibits a complex shape evolution while progressing towards a final rest configuration[60–62]. In some instances, wetted area must change topology from initially disconnected disks to a connected disk, for example, Figure 1.2. As drops merge into a single body of fluid, liquid sweeping accumulates both a cumulative wetted $\mathcal{W}_\infty$ and cumulative projected $\mathcal{P}_\infty$ area. Wetted sweeping occurs due to contact line motion, while projected sweeping results from dynamics of the

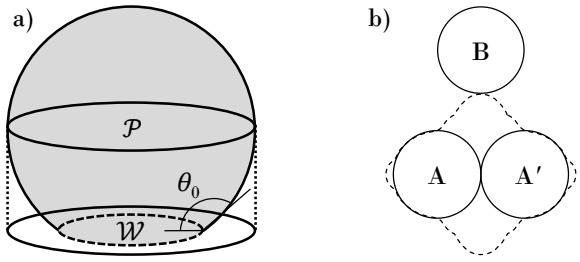

Figure 1.1: a) Sessile drop: initial contact angle $\theta_0 > 90°$, projected $\mathcal{P}$ and wetted $\mathcal{W}$ contact areas. b) Projected view (top) of coalescing drops $A - A'$ with cumulative swept area (dashed) just reaching drop B, perhaps initiating another coalescence.

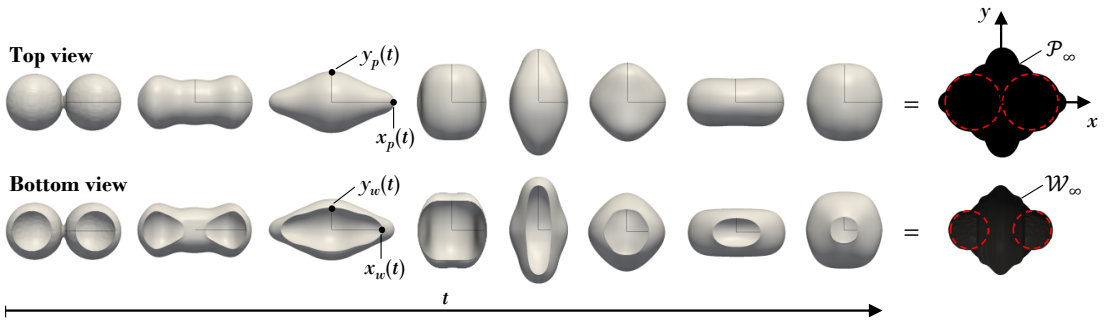

Figure 1.2: Instantaneous projected $\mathcal{P}(t)$ (top row) and wetted $\mathcal{W}(t)$ (bottom row) swept areas, with cumulative projected $\mathcal{P}_\infty$ (top right) and wetted $\mathcal{W}_\infty$ (bottom right) swept areas. Circles on the silhouettes (red dashed) represent the initial areas.

bulk liquid above the surface. $\mathcal{P}_\infty = \mathcal{W}_\infty$ on wetting and hydrophilic surfaces, where $\theta_0 < 90°$. However, $\mathcal{P}_\infty > \mathcal{W}_\infty$ for sessile drop coalescence on non-wetting and hydrophobic surfaces where $\theta_0 > 90°$ since, for these, the body of the liquid overhangs the contact line during the coalescence event. Depending on the interplay of solid, liquid, and gas phases, the area swept during a coalescence event can vary dramatically, reflecting how interfacial energy is partitioned into kinetic energy and dissipation.

Understanding swept areas is important both fundamentally and from an applications perspective. For example, self-cleaning surfaces leverage sweeping by sessile drop coalescence to collect contaminants and other foreign debris for removal[63]. Anti-frost coatings rely on coalescence to eject drops before freezing can occur, with multiple drops merging via sweeping during the removal process[64]. The growth rate of drops on water harvesting devices is strongly accelerated by multi-drop coalescence events, which leads to enhanced liquid collection rates[65]. Finally, in dropwise condensation heat transfer processes, a principal mechanism of fresh surface generation for renucleation is the sweeping up of drops by a coalescence event[45,66]. These swept regions have a signif-

icant impact on heat transfer as smaller, renucleated drops have a higher heat flux as compared to larger, more insulating drops[34]. A sketch of multi-drop coalescence sweeping is shown in Figure 1.1b.

A typical coalescence sequence is demonstrated in Figure 1.2. At the initiation of coalescence between two sessile drops, a small liquid neck forms with large curvature. This curvature generates a significant capillary force in the neck which drives a rapid expansion of the liquid bridge[67,68]. As the bridge expands, capillary waves travel outward along the x-axis towards the ends of the drops. Once the capillary waves reach the ends, they are reflected back towards the coalescence initiation point. This causes the liquid to contract along the x-axis and drives a continued expansion in the y-direction until a maximum is reached. The liquid then exhibits damped oscillations that alternate between the x- and y-directions, with the contact line eventually pinning or, perhaps, with the liquid jumping off the surface. After contact line pinning, remaining kinetic energy is dissipated solely by bulk viscosity and the liquid settles to a final rest shape. For high surface tension liquids like water or mercury, the coalescence event is a strongly underdamped oscillation where inertia and interfacial energy compete while being mitigated by contact line and bulk viscous dissipation. The contact line contribution can be significant, as shown later.

An early formal study on sessile drop coalescence was published in 2001 by Menchaca-Rocha and collaborators[60]. In this work, experiments and numerical simulations were employed to elucidate the shape evolution of two identical mercury drops coalescing on a super-non-wettable surface. Since then, numerous papers on sessile drop coalescence have appeared. Topics of investigation have included power law growth of the liquid bridge after coales-

cence initiation[69–75], overall shape evolution[22,61,76–81], and long-time contact line relaxation dynamics[21,82–85]. Following the 2009 discovery of self-propelled dropwise condensate removal on superhydrophobic surfaces[49,86], a majority of these studies have explored coalescence-induced out-of-plane drop jumping[28,29,87–109]. For their utility in interpreting experimental observations, computational fluid dynamics simulations of sessile drop coalescence have also become popular over the last decade[110–113]. The coalescence sweeping phenomenon has not been studied previously, as far as we are aware.

In this paper, numerical simulations are performed to investigate sweeping by binary sessile drop coalescence for identical drops having no approach velocity in a solid-water-air system. First, the numerical model, simulation domain, and computational procedure are described. The model is then validated versus three experimental cases of sessile water drop coalescence. After verifying the model, the influence of the surface wettability on sweeping is explored by changing the initial contact angle of the coalescing drops (θ_0). It is noted that testing is limited to cases where $90° \leq \theta_0 \leq 180°$ since hydrophobic and/or superhydrophobic surfaces are typically employed for self-cleaning, anti-frost, water harvesting, and dropwise condensation applications. Wetted and projected swept areas are then quantified, with an energy accounting performed to help understand the sweeping behavior. The sessile drop coalescence results are further contrasted with the free drop coalescence case to investigate how the surface constraint influences sweeping. Finally, the time duration of sweeping is explored. This study is a first to quantify sweeping by sessile drop coalescence and to address the role of surface wettability in determining the extent of area swept, to our knowledge.

1.3 Numerical Method

1.3.1 Simulation Perspective

Simulating interface dynamics for incompressible two-phase flows is an active research topic[114]. Adding moving contact lines further complicates the problem. We choose a volume of fluid (VOF) approach with a diffuse interface based on its success in prior studies with moving contact lines. Alternative approaches to incorporating moving contact lines split between those where the dynamic contact angle is an input[115,116] and those where it is an output[117,118] of the numerical simulation. We choose as an 'input' contact-line model the Kistler empirical correlation[119] since this experimentally determined correlation has demonstrated engineering utility. The smearing of the liquid-gas interface inherent to our VOF model allows for compatibility of Kistler with a no-slip boundary condition imposed on the solid surface. For comparison, a sharp interface model would require some form of stress relief, for example, by way of a slip length. Notably, the Kistler method depends only on the advancing and receding contact angles, two parameters which can be measured independently in experiment. As a consequence, an important and distinguishing feature of our simulation setup is that no parameters are left free for fitting to experiment.

1.3.2 Volume of Fluid Formulation

Sessile drop coalescence is simulated in OpenFOAM, an open source computational fluid dynamics software[120,121]. A modified version of the interFoam VOF solver is employed where artificial anti-diffusive surface fluxes are re-

moved to allow for a more accurate prediction of the capillary-dominated coalescence flow[102]. This brings the time response of the simulation dynamics into line with the experimental results, Figure A.1 in Appendix A.1. A VOF method is chosen for its advantages in mass conservation. The interFoam solver is employed for incompressible, laminar, two-phase fluid flow with each computational cell containing some volume fraction of liquid (α) where $0 \leq \alpha \leq 1$. In any cell, fluid properties like density (ρ) and dynamic viscosity (μ) are a weighted average based on the volume fraction of liquid,

$$\rho = \alpha\rho_l + (1-\alpha)\rho_g, \tag{1.1}$$

$$\mu = \alpha\mu_l + (1-\alpha)\mu_g, \tag{1.2}$$

where subscripts l and g denote liquid and gas phases, respectively. Since α is a conserved scalar via the incompressibility condition, it satisfies the advection equation

$$\frac{\partial\alpha}{\partial t} + \boldsymbol{\nabla}\cdot(\alpha\boldsymbol{u}) = 0. \tag{1.3}$$

Note the lack of an artificial interface compression term in this equation. In the simulations reported below, interface thicknesses vary in time but stay below a maximum of 5% of the computational domain size. In the standard way for a VOF method, continuity and momentum equations govern the flow,

$$\boldsymbol{\nabla}\cdot\boldsymbol{u} = 0, \tag{1.4}$$

$$\frac{\partial\rho\boldsymbol{u}}{\partial t} + \boldsymbol{\nabla}\cdot(\rho\boldsymbol{u}\boldsymbol{u}) = -(\boldsymbol{\nabla}\cdot P) + \boldsymbol{\nabla}\cdot(\mu\,(\boldsymbol{\nabla}\boldsymbol{u} + \boldsymbol{\nabla}\boldsymbol{u}^T)) + \rho\,\boldsymbol{g} + \boldsymbol{F_b}, \tag{1.5}$$

where $\boldsymbol{u} = (u_x, u_y, u_z)$ is the velocity, t is time, P is pressure, and $\boldsymbol{g}$ is the gravity vector. Here, $\boldsymbol{F_b} = \sigma_{lg}\kappa\boldsymbol{\nabla}\alpha$ is the surface tension body force vector modeled by the continuum surface force method of Brackbill[122] where σ_{lg} is liquid-gas surface tension and $\kappa = -\boldsymbol{\nabla}\cdot(\frac{\boldsymbol{\nabla}\alpha}{|\boldsymbol{\nabla}\alpha|})$ is the liquid-gas interfacial curvature. By

definition, the surface tension body force acts solely on liquid-gas interfacial cells. Equations (1.3), (1.4), and (1.5) are solved subject to a moving contact line model, specified next.

1.3.3 Dynamic Contact Angle Model

To account for fluid interactions with the surface, the dynamic contact angle model of Kistler[119] is employed for cases of advancing and receding contact line. The Kistler model relates the dynamic contact angle θ to the velocity of the contact line U_{CL}, using in its scaled form the Kistler capillary number $Ca_K = \mu U_{CL}/\sigma_{lg}$. Kistler has been shown to accurately represent the behavior of moving contact lines in other drop-based simulations, including sessile drop coalescence, without any fitting parameters[112,123–127]. For advancing and receding contact lines, respectively,

$$\theta = f[f^{-1}(\theta_a) + Ca_K] \; for \; U_{CL} > 0, \tag{1.6}$$

$$\theta = f[f^{-1}(\theta_r) + Ca_K] \; for \; U_{CL} < 0, \tag{1.7}$$

where θ_a is the advancing contact angle, θ_r is the receding contact angle, and f is the empirical Hoffman function, based on a systematic study of silicone oils displacing air in glass capillaries[128], expressed mathematically by Kistler as

$$f(x) = \cos^{-1}\left\{1 - 2\tanh\left[5.16\left(\frac{x}{1 + 1.31x^{0.99}}\right)^{0.706}\right]\right\} \tag{1.8}$$

with $0 \leq f \leq \pi$. When $U_{CL} = 0$, the contact line is stationary and the contact angle is free to exhibit values between θ_r and θ_a. Note that θ_0 does not appear explicitly in the model but is bounded by $\theta_r < \theta_0 < \theta_a$. See Figure 1.3 (inset) for a sketch of θ vs. Ca_K response.

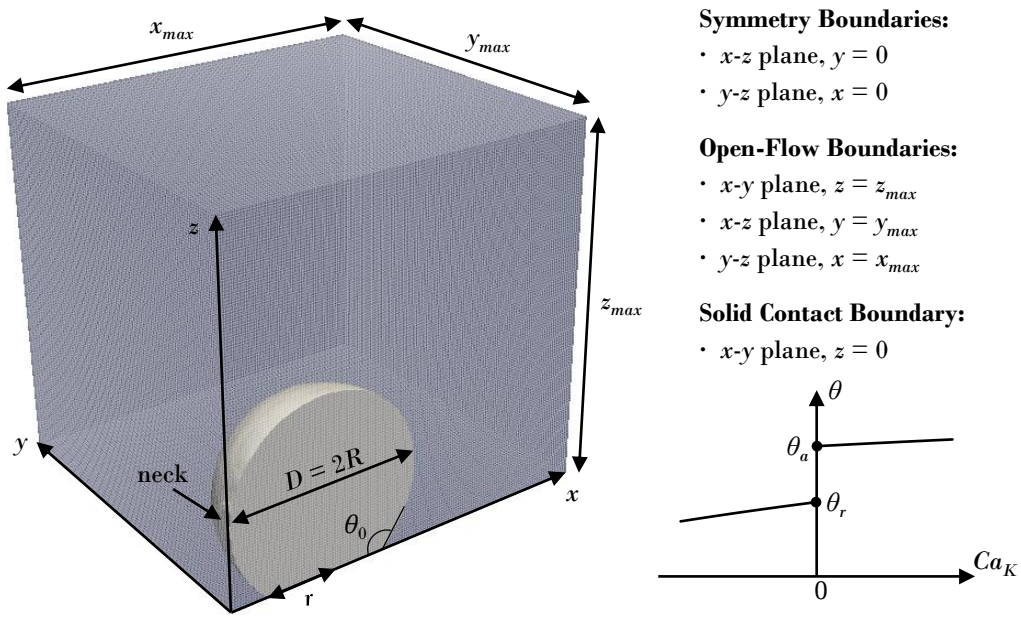

Figure 1.3: Computational domain: flow is bounded by symmetry, open-flow, and solid contact boundaries. At the moving contact line, the Kistler model is implemented, Equations 1.6, 1.7, and 1.8, sketched (lower right) and showing stick for $\theta_r \leq \theta \leq \theta_a$ and slip otherwise.

Table 1.1: Simulation fluid properties: water (subscript l) and air (subscript g).

ρ_l (kg/m^3)	ρ_g (kg/m^3)	μ_l (mPa · s)	μ_g (mPa · s)	σ_{lg} (J/m^2)
998.0	1.204	0.998	0.0181	0.072

1.3.4 Computational Domain and Procedure

A 1.4 mm x 1.3 mm x 1.3 mm (x by y by z) computational domain comprised of cubic cells with edge length $\epsilon = 10\,\mu$m is used to study the influence of surface wettability on coalescence sweeping (Figure 1.3). In simulating the coalescence of two identical drops with no approach velocity, two symmetry planes are employed to reduce the computational load. At the top and sides of the domain, a fixed pressure boundary with zero velocity gradient is applied. The bottom of

the domain is a no-slip solid contact boundary. Near the contact line, Kistler's dynamic contact angle model is implemented with a specified value of θ_a and θ_r. In the absence of a slip boundary condition, the VOF solver utilizes the cell face normal velocities in computational cells immediately above the solid contact boundary to estimate U_{CL} for use in the Kistler model and to advect volume fractions. Fluid properties are for a water-air system at approximately ambient temperature, see Table 1.1. Initial drop diameters, D, range from 0.7 mm to 1.0 mm, meaning at least 70 cells per drop diameter. This has been shown to give convergence in other coalescence simulations[97,105,112,126]. Finally, gravity is neglected to facilitate comparison against prior computational literature on sessile drop coalescence. For model verification versus experiment, the domain size is amended to 2.6 mm x 2.6 mm x 2.6 mm with cubic cells of edge length $\epsilon = 20$ μm to accommodate D values ranging from 1.5 mm to 2.0 mm. Also, the gravity vector is enforced in the negative z-axis direction with magnitude 9.807 m/s^2 to match the experimental conditions in our Earth-based experiments.

In the numerical solution scheme, the advection equation for α is first solved via the multi-dimensional universal limiter with explicit solution (MULES) method at a timestep, Δt, that satisfies a Courant number of $C \leq 0.2$ in each computational cell. For computations in three dimensions, the Courant number is defined as

$$C = \frac{|u_x|\Delta t}{\epsilon} + \frac{|u_y|\Delta t}{\epsilon} + \frac{|u_z|\Delta t}{\epsilon} \tag{1.9}$$

and governs how rapidly data is translated in the simulation domain to ensure numerical stability. Next, to maintain the contact angle prescribed by the Kistler model, the interface orientation obtained from the advection equation is corrected at each time step. Then, the liquid-gas interface is smoothed before calculation of the interfacial curvature κ. Finally, the pressure implicit with

splitting of operators (PISO) algorithm[129] is employed to solve the momentum and continuity equations. Output files containing data from the computations are generated at user-specified time intervals for subsequent post-processing.

1.4 Characteristic Scales and Non-Dimensional Numbers

For the inertial coalescence of capillary drops, motions respond on the inertial-capillary timescale $\tau = (\rho_l R^3/\sigma_{lg})^{1/2}$ where, for two identical coalescing drops, R is the initial radii of the drops. This allows the dynamics to be described in terms of the non-dimensional timescale $t^* = t/\tau$. The characteristic length scale is taken as the initial diameter of a drop, $D = 2R$. Capillary drops are distinguished by Bond numbers $Bo = (\rho_l - \rho_g)|\boldsymbol{g}|D^2/\sigma_{lg}$ less than unity for which surface tension dominates over gravity. Other relevant non-dimensional numbers include the Reynolds number $Re = \rho_l u_{ch} D/\mu_l$, Ohnesorge number $Oh = \mu_l/(\rho_l \sigma_{lg} D)^{1/2}$, and Capillary number $Ca = \mu_l u_{ch}/\sigma_{lg}$ where u_{ch} is a characteristic velocity in the liquid phase. In this work, u_{ch} is specified as the maximum value of the mass-averaged velocity in the liquid phase over the course of a coalescence event,

$$u_{ch} \equiv max\left(\frac{\int_{V_l} \rho|\boldsymbol{u}|dV}{\int_{V_l} \rho\, dV}(t)\right), \tag{1.10}$$

where V_l is the total liquid phase volume and dV is the volume of a mesh element.

1.5 Sweeping Metrics

From a top view of the coalescing drops, a projected swept area $\mathcal{P}_\infty$ is traced as the combining liquid drops progress to a rest state, Figure 1.2. The fractional increase in projected swept, relative to initial projected area $\mathcal{P}_0 = 2\pi R^2$, is

$$\mathcal{P}^* \equiv \frac{\mathcal{P}_\infty}{\mathcal{P}_0}. \tag{1.11}$$

Similarly, from a bottom view, a wetted area $\mathcal{W}_\infty$ is swept in time, Figure 1.2. The fractional increase in wetted swept, relative to initial wetted area $\mathcal{W}_0 = 2\pi r^2$, is

$$\mathcal{W}^* \equiv \frac{\mathcal{W}_\infty}{\mathcal{W}_0}, \tag{1.12}$$

with $r = R\sin\theta_0$ the base wetted radius of the initial drop. Alternatively, a net cumulative metric can be used, $\mathcal{P}^{**} \equiv \mathcal{P}_\infty/\mathcal{P}_0 - 1$, $\mathcal{W}^{**} \equiv \mathcal{W}_\infty/\mathcal{W}_0 - 1$. Since the denominator $\mathcal{W}_0$ vanishes as $\theta_0 \to 180°$, we also use regularized forms, $\mathcal{W}^*\,(\mathcal{W}_0/\mathcal{P}_0)$ and $\mathcal{W}^{**}\,(\mathcal{W}_0/\mathcal{P}_0)$, for respective comparison to $\mathcal{P}^*$ and $\mathcal{P}^{**}$. Time progressions of the projected (x_p & y_p) and wetted (x_w & y_w) extensions in the x-and y-axes are also evaluated, Figure 1.2. As discussed in the results, projected extensions are normalized by $2R$ while wetted extensions are normalized by $r + R$ with non-dimensional parameters indicated by an asterisk superscript (*).

1.6 Mechanical Energy Balance

To interpret the coalescence sweeping results, we evaluate the mechanical energy balance of Dussan V. and Davis[130] using the VOF simulations. This continuum mechanical energy balance involves sharp interface integrals over volumes, surfaces, and contours. For these evaluations, the VOF contour $\alpha = 0.5$

is identified as the sharp interface location and the contact line is estimated as intersection of the drop surface and the substrate. This energy balance separates reversible energy changes from dissipative losses,

$$\frac{d}{dt}\left(\mathcal{A}+\mathcal{K}\right)=-\mathcal{D}<0, \tag{1.13}$$

where $\mathcal{A}=A_{sl}\sigma_{sl}+A_{lg}\sigma_{lg}+A_{sg}\sigma_{sg}$ is interfacial energy, $\mathcal{K}=\int_V \frac{1}{2}\rho\left(\boldsymbol{u}\cdot\boldsymbol{u}\right)dV$ the kinetic energy, and $\mathcal{D}$ the dissipation rate. The interfacial energy is defined as the sum of the solid-liquid (sl), liquid-gas (lg), and solid-gas (sg) interfacial areas, A, weighted by respective surface energies, σ. The dissipation rate $\mathcal{D}=\mathcal{D}_\theta+\mathcal{D}_\mu+\mathcal{D}_\beta$ has possible contributions from contact line motion, $\mathcal{D}_\theta$, slip at the liquid-solid surface, $\mathcal{D}_\beta$, and from volumetric viscous effects, $\mathcal{D}_\mu$. The work done at the contact line by the uncompensated Young's force is fully dissipated enabling an evaluation, $\mathcal{D}_\theta=\int_\gamma \sigma_{lg}(\cos\theta_e-\cos\theta)U_{CL}\,d\gamma$, where γ is the contact line arc length and θ_e is the equilibrium contact angle from the Young-Dupré equation, $\sigma_{sg}=\sigma_{sl}+\sigma_{lg}\cos\theta_e$. Regarding slip dissipation, $\mathcal{D}_\beta=0$ is consistent with the no-slip condition $\beta=0$ implemented in the VOF simulations. Additionally, taking $\beta=0$ maintains a simulation scheme with no adjustable parameters. The viscous dissipation, $\mathcal{D}_\mu=\int_V \mu\,\Phi\,dV$, is calculated in the standard way from the viscous dissipation function,

$$\begin{aligned}\Phi=2\Big[\Big(\frac{\partial u_x}{\partial x}\Big)^2+\Big(\frac{\partial u_y}{\partial y}\Big)^2+\Big(\frac{\partial u_z}{\partial z}\Big)^2\Big]+\Big(\frac{\partial u_y}{\partial x}+\frac{\partial u_x}{\partial y}\Big)^2\\+\Big(\frac{\partial u_z}{\partial y}+\frac{\partial u_y}{\partial z}\Big)^2+\Big(\frac{\partial u_x}{\partial z}+\frac{\partial u_z}{\partial x}\Big)^2-\frac{2}{3}(\boldsymbol{\nabla}\cdot\boldsymbol{u})^2.\end{aligned} \tag{1.14}$$

The volume V in the integrals of $\mathcal{D}_\mu$ and $\mathcal{K}$ is taken as the combined volume V of liquid and gas phases; that is, the full computational domain. Integration of Equation (1.13) in time yields that the change in kinetic plus interfacial energy must balance the dissipative losses over that time interval. Introducing the

notation $\Delta\mathcal{A}(t) \equiv \mathcal{A}(t) - \mathcal{A}(0)$ and recognizing $\mathcal{K}(0) = 0$ leads to

$$\Delta\mathcal{A}(t) + \mathcal{K}(t) = -\int_0^t \mathcal{D}\, dt \equiv -\overline{\mathcal{D}}(t). \tag{1.15}$$

During a coalescence event, interfacial and kinetic energies convert back and forth while continuously being discounted by dissipation. Using Equation (1.15), we track how this energy interchange occurs during sweeping. All energies are made non-dimensional via scaling by $\sigma_{lg}R^2$, with dimensionless parameters indicated by an asterisk (*) as mentioned previously. As time progresses, the drop either jumps, at t_{jump}, or the kinetic energy transient dies out, at t_∞, where, t_∞ is defined as when oscillations in the contact line and liquid-gas interface have decayed to within 1% of some long-time average position. At long enough times, one expects the loss of interfacial energy to balance dissipation,

$$\Delta\mathcal{A}(t_\infty) = -\overline{\mathcal{D}}(t_\infty). \tag{1.16}$$

The difference between right and left hand sides of Equation (1.15) serves as an additional assessment of the simulation quality. For all cases (Table 1.3), with Equation (1.15) evaluated at t_{jump} (superhydrophobic cases) or at t_∞ (hydrophobic cases), the left- and right-hand sides of Equation (1.15) agree to 15% or better. This discrepancy may have various contributions: a) early phase error, since a small initial discrepancy in phase can lead to large discrepancies longer term for underdamped oscillators; b) neglected dissipation, since there may be effective slip near the contact line in VOF while $\beta = 0$ was assumed in Equation (1.15); and c) sharp interface location, since for the energy-dissipation balance, $\alpha = 0.5$ may not be appropriate as it is for mass conservation. Of course, a) and b) may be related since phase differences are well-known to be sensitive to damping. However, trends reported below based on the evaluation of Equation (1.15), for example in the discussion of Figures 1.8 and 1.9, are not influenced by this discrepancy. Further examination of these matters is beyond our scope.

1.7 Results and Discussion

1.7.1 Model Validation

The numerical model is verified against binary sessile drop coalescence experiments on various surfaces, with three coalescence trials performed on each substrate. A summary of the tested surfaces with their wettability metrics is found in Table 1.2, where contact angle hysteresis is defined as $\Delta\theta = \theta_a - \theta_r$. All sanded surfaces are prepared using silicon carbide sandpaper (Starcke Abrasives). For the experiments, coalescence is induced by slowly growing a drop via a 0.5 mm diameter through-hole in the surface until it touches a second pre-positioned drop (Figure 1.4). An automatic dispensing system (ramé-hart part no. 100-22) is used to control the drop growth rate at 0.2 μL/s such that the drops have a minimal approach velocity. In all experiments, the drops are of approximately equal size at the time of coalescence (diameters within 5% of each other) with D in the range of 1.5 mm to 2.0 mm ($Bo \sim 0.3$ to 0.5). Top and side view video cameras (Redlake MotionPro HS-3 and Redlake MotionXtra HG-XL, respectively) simultaneously record the coalescence dynamics at a

Table 1.2: Experimental surfaces (chemistry, roughness) and wettability by water: initial contact angle θ_0, advancing θ_a, receding θ_r, and contact angle hysteresis $\Delta\theta$.

Surface	θ_0 (°)	θ_a (°)	θ_r (°)	$\Delta\theta$ (°)
Teflon	110	120	75	45
Sanded Teflon, 320 grit	141	154	76	78
Sanded Teflon, 120 grit	151	159	102	57

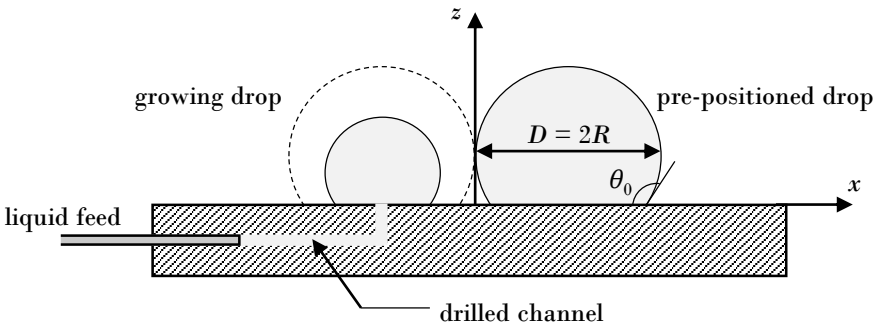

Figure 1.4: Experimental setup (side view): liquid fed drop (left) grows until it touches a pre-positioned drop (right), initiating the coalescence event.

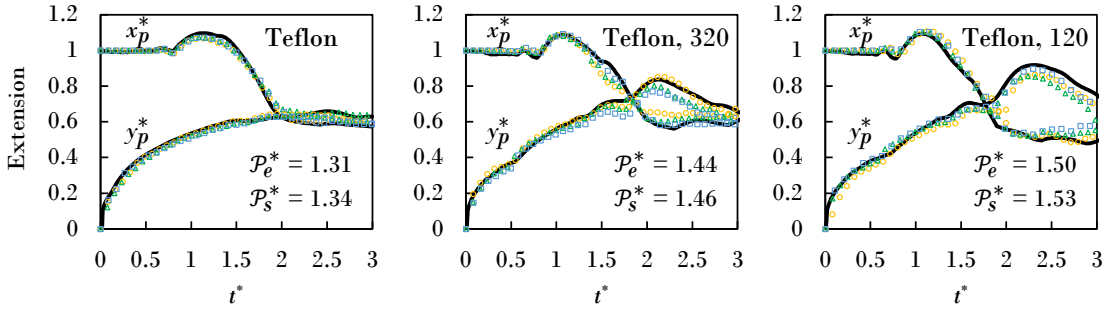

Figure 1.5: Validation: simulation (solid line) and experiment (markers) for three runs each (triangle, circle, and square markers) and three surfaces (Table 1.2). Projected swept areas, for experiment $\mathcal{P}_e^*$ and simulation $\mathcal{P}_s^*$, as listed. No fitting parameters.

frame rate of at least 3,500 frames per second. The side view gives information about the initial drop sizes and contact angles, while the top view ensures the drops are initially axisymmetric and gives the projected swept area and extensions. Comparing simulation against experiment, the time evolutions of x_p^* and y_p^* are in excellent agreement in all cases, Figure 1.5, where data is plotted against the non-dimensional time. The non-dimensional projected swept areas resulting from the coalescence dynamics are also found to be comparable in all cases, with the simulation thought to slightly exceed the experiment due to the

exact matching of the initial drop sizes. For a comparison of fluid dynamics by top view between simulation and experiment for select cases, see Video A.1 of Appendix A.2. Note that Wasserfall and collaborators[102] have independently verified the modified interFoam solver by simulating free drop oscillations at various Reynolds numbers.

1.7.2 Parametric Study

After validating the numerical model, a parametric study of the surface wettability influence on sweeping is undertaken. Table 1.3 provides the various contact angles tested over the range $90° \leq \theta_0 \leq 180°$. In all cases, except for $\theta_0 = 180°$, the contact angle hysteresis was set to $\Delta\theta = 15°$ with $\theta_a = \theta_0 + 5°$. Table 1.3 also provides the relevant dimensionless numbers associated with the dynamics of the coalescence event. For all simulations, the Reynolds number confirms laminar flow while the Ohnesorge and Capillary numbers indicate that capillary and inertia forces dominate over viscous effects. Additionally, recall that gravity is set to zero in these studies so $Bo = 0$. For each simulation in the hydrophobic regime ($90° \leq \theta_0 < 150°$), the left- and right-hand sides of Equation (1.15) agree within 15% of each other as $t \to t_\infty$. This indicates that the interfacial energy release is well-balanced by dissipation at long times when the kinetic energy approaches zero. For all superhydrophobic drop coalescence cases ($\theta_0 \geq 150°$), the liquid jumps away from the surface during the coalescence event. For these, Equation (1.15) is evaluated at the time of drop jumping (t_{jump}). The agreement between the left- and right-hand sides falls within a few percent of each other. These energy analyses provide an additional indication of the simulation fidelity.

Table 1.3: Simulation parameters: surface wettability angles θ_0, θ_a, θ_r, and $\Delta\theta$; initial diameter D; characteristic velocity u_{ch}; Reynolds Re, Ohnesorge Oh, and Capillary Ca numbers.

No.	θ_0 (°)	θ_a (°)	θ_r (°)	$\Delta\theta$ (°)	D (mm)	u_{ch} (m/s)	Re	Oh	Ca
1	90	95	80	15	1.00	0.21	205	0.004	0.003
2	101	106	91	15	0.88	0.23	203	0.004	0.003
3	113	118	103	15	0.80	0.25	203	0.004	0.004
4	123	128	113	15	0.76	0.27	203	0.004	0.004
5	131	136	121	15	0.74	0.27	203	0.004	0.004
6	141	146	131	15	0.72	0.28	201	0.004	0.004
7	150	155	140	15	0.71	0.30	214	0.004	0.004
8	160	165	150	15	0.71	0.31	223	0.004	0.004
9	170	175	160	15	0.71	0.32	224	0.004	0.004
10	180	180	180	0	1.00	0.27	272	0.004	0.004

Sweeping and extension results for both the hydrophobic and superhydrophobic regimes are plotted in Figure 1.6, along with the free drop coalescence case (white dashed lines). In the hydrophobic regime (blue shading), net swept areas $\mathcal{P}^{**}$ and $\mathcal{W}^{**}(\mathcal{W}_0/\mathcal{P}_0)$ are observed to increase with θ_0 which manifests from broader liquid extensions in the y-axis during the coalescence event. Additionally, when θ_0 increases, the drop footprints become smaller and more separated which benefits $\mathcal{W}^{**}(\mathcal{W}_0/\mathcal{P}_0)$ because the surface area between the drop footprints is always traversed by liquid. The maximum extent of liquid deformation in the x-axis is observed to be similar in all cases and results from capillary wave propagation after coalescence initiation. Furthermore, in the hydrophobic regime, $\mathcal{P}^{**}$ and $\mathcal{W}^{**}(\mathcal{W}_0/\mathcal{P}_0)$ are nearly identical indicating that a similar amount of net wetted and projected area is swept by the coalescence event.

In the superhydrophobic regime (green shading), $\mathcal{P}^{**}$ continues to increase with θ_0 while $\mathcal{W}^{**}(\mathcal{W}_0/\mathcal{P}_0)$ trends downward as $\theta_0 \rightarrow 180°$. For $\mathcal{W}^{**}(\mathcal{W}_0/\mathcal{P}_0)$, the enhanced hydrophobicity compels less liquid contact with the surface which reduces wetted contact sweeping. Additionally, as θ_0 increases, the liquid departs from the surface at earlier times which cuts short further wetted contact sweeping. Figure 1.7 illustrates the cumulative wetted and projected swept areas at various θ_0, as normalized by the initial diameter of the drops. Initial drop projections and wetted contacts are also included for reference.

To further elucidate the swept area results, the transients in interfacial, kinetic, and dissipative energies are analyzed. Figure 1.8 plots $\Delta\mathcal{A}^*$ and $\mathcal{K}^*$ versus t^*, where it is observed that the release of interfacial energy in time correlates directly with the evolution of the kinetic energy, as expected. In general, the kinetic energy transients are greater in magnitude at larger θ_0 values. Addi-

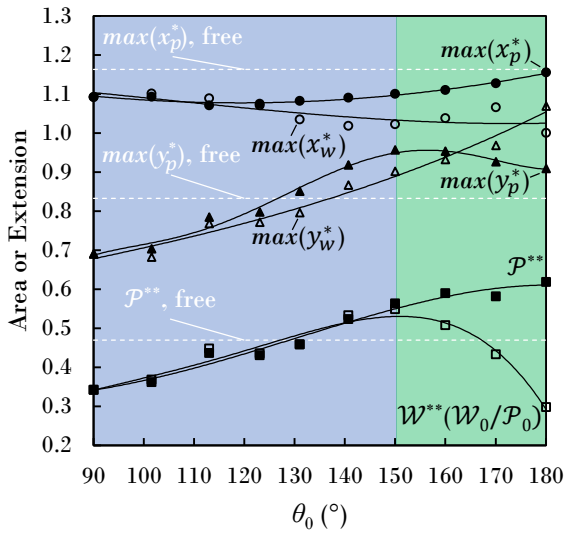

Figure 1.6: Swept areas (squares) and maximum extensions (x, circles; y, triangles), as influenced by wettability θ_0, with guide (solid fit lines). Binary free drop coalescence case (white dashed). Regimes: hydrophobic (blue) and superhydrophobic (green).

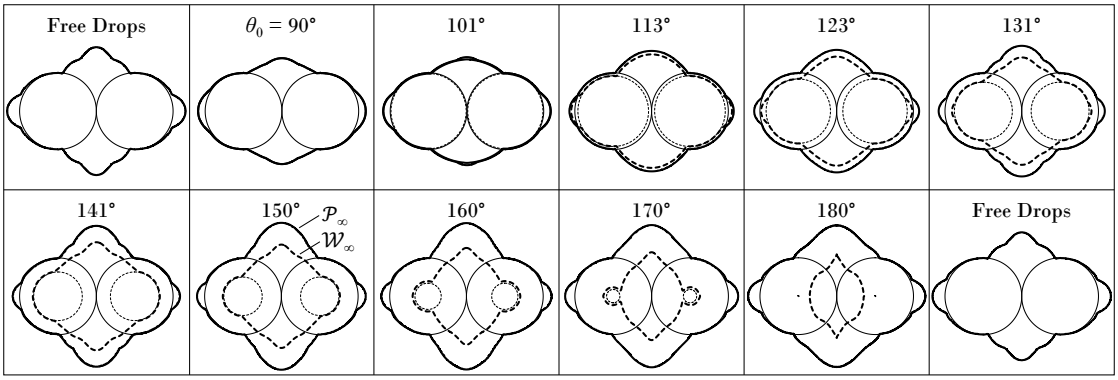

Figure 1.7: Cumulative swept areas: wetted $\mathcal{W}_\infty$ (thick dashed) and projected $\mathcal{P}_\infty$ (thick solid), with initial wetted (thin dashed) and initial projected (thin solid) areas, for reference. All areas are scaled, for comparison.

tionally, it is noted that $max(\mathcal{K}^*)$ always occurs during the initial expansion of the liquid in the y-direction, specifically after the maximum x-axis extension is reached and the capillary waves are reflected back towards the coalescence initiation point ($1.5 < t^* < 2.0$). As $max(\mathcal{K}^*)$ increases with θ_0 during this time, the liquid obtains a correspondingly larger y-component of momentum in the positive (and negative) y-axis domain, Figure 1.8. This eventually leads to greater y-axis maximum extensions during $2.0 < t^* < 2.5$ which increases the amount of area swept. In terms of energy loss during coalescence, Figure 1.9, the dimensionless bulk viscous dissipation, $\overline{\mathcal{D}}^*_\mu \equiv \int_0^t \mathcal{D}_\mu \, dt/\sigma_{lg}R^2$, is monotonically increasing in θ_0 nearly uniformly in t^* over the range while contact line dissipation, $\overline{\mathcal{D}}^*_\theta \equiv \int_0^t \mathcal{D}_\theta \, dt/\sigma_{lg}R^2$, is rather mixed. For example, at $t^* = 3$ the order of increasing $\overline{\mathcal{D}}^*_\theta$ is $\theta_0 = \{180°, 90°, 170°, 101°, 113°, 160°, 150°, 141°, 131°, 123°\}$. The maximum in $\overline{\mathcal{D}}^*_\theta$ that occurs near 123° is evidently the result of competition between lessening perimeter and increasing vigor of contact line motion owing to heightening center of mass. Decreased total dissipation, of course, allows for a larger conversion of interfacial energy to kinetic energy.

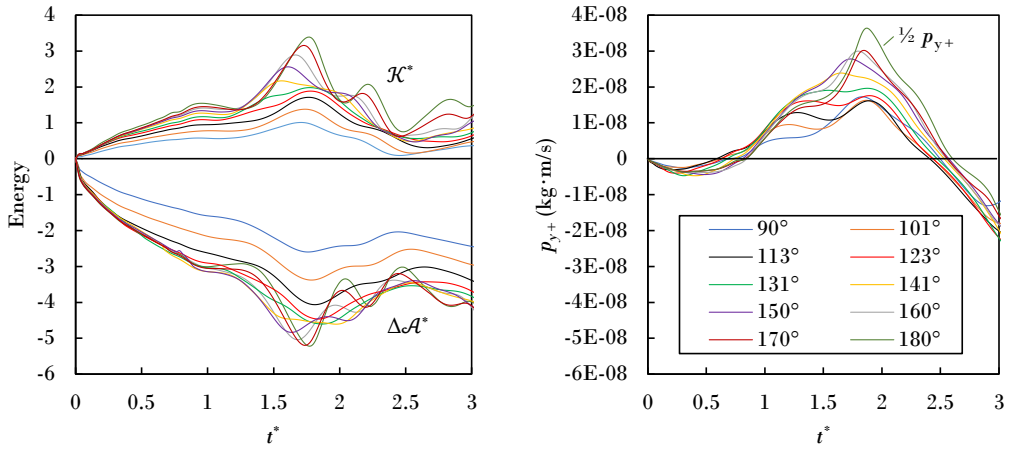

Figure 1.8: Evolution (left) of kinetic energy $\mathcal{K}^*$ and change in interfacial energy $\Delta\mathcal{A}^*$. Evolution (right) of total plane-normal momentum p_{y+} (y-component in positive y-direction).

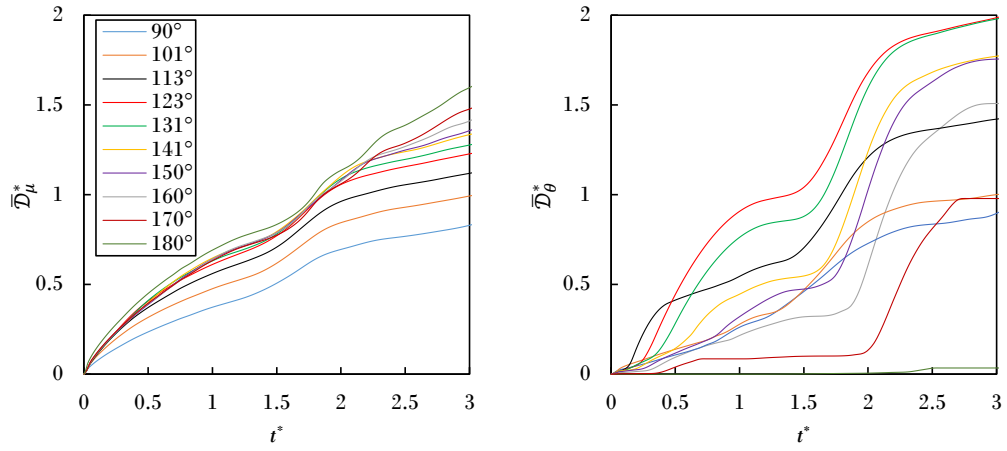

Figure 1.9: Evolution of cumulative energy losses: bulk viscous $\overline{\mathcal{D}}^*_\mu$ (left) and contact line $\overline{\mathcal{D}}^*_\theta$ (right) contributions to the overall dissipation $\overline{\mathcal{D}}^* = \overline{\mathcal{D}}^*_\mu + \overline{\mathcal{D}}^*_\theta$.

A comparison of the projected swept areas for sessile drop coalescence is also made with the free drop coalescence case, Figures 6 and 7. For the pairwise coalescence of two free drops, $\mathcal{P}^{**} = 0.44$ with $max(x_p^*) = 1.16$ and $max(y_p^*) = 0.83$. The value of $max(x_p^*)$ is slightly greater than all the sessile drop cases because the capillary wave traveling on the bottom side of the liquid is undisturbed by

a surface. This allows it to eventually reach the extreme edge of the drop which amplifies the final liquid extension. In contrast, the value of $max(y_p^*)$ is surpassed by the sessile drop case at $\theta_0 \sim 130°$. This is a result of the surface breaking the symmetry of the coalescence dynamics. As θ_0 trends towards 180°, the drops become more spherical similar to the free drop case. However, since the surface cannot be penetrated by fluid, when the liquid bridge impinges on the substrate the fluid is redirected upwards and can lead to enhanced sweeping. For $\theta_0 > 130°$, the larger values of $max(y_p^*)$ achieved versus the free drop case allow sessile drops to attain greater $\mathcal{P}^{**}$ values.

The time duration of sweeping is additionally investigated with Figure 1.10 showing $\mathcal{P}^{**}$ (left) and $\mathcal{W}^{**}(\mathcal{W}_0/\mathcal{P}_0)$ (right) versus t^* for various θ_0 values. It is observed that the evolution of $\mathcal{P}^{**}$ is nearly the same through $t^* = 1.125$ for all sessile drop coalescence cases, except $\theta_0 = 180°$ which evolves similarly to the free drop case. This time frame corresponds to early liquid bridge growth and the initial capillary wave propagation to $max(x_p^*)$. Deviations occur after this time, but in all cases more than 80% of $\mathcal{P}^{**}$ is swept by the time $max(y_p^*)$ is reached at $t^* \sim 2.5$. This indicates that a majority of the sweeping happens rapidly via the attainment of $max(x_p^*)$ and then $max(y_p^*)$ in succession during the first full oscillation of the liquid. For $\theta_0 > 130°$, the remaining area to be swept is achieved during liquid retraction immediately after $max(y_p^*)$ is attained, similar to the free drop coalescence case. Note that in the superhydrophobic regime ($\theta_0 \geq 150°$), the projected swept area can continue to evolve after the instant of drop jumping; see the dashed lines in Figure 1.10. For $\theta_0 < 130°$, $\mathcal{P}^{**}$ plateaus after $t^* \sim 2.5$ before eventually reaching its final value as the liquid settles to a rest shape. The time span before this settling is observed to increase with θ_0 due to the increased kinetic energy in the liquid. For $\mathcal{W}^{**}(\mathcal{W}_0/\mathcal{P}_0)$, analogous sweeping behavior is

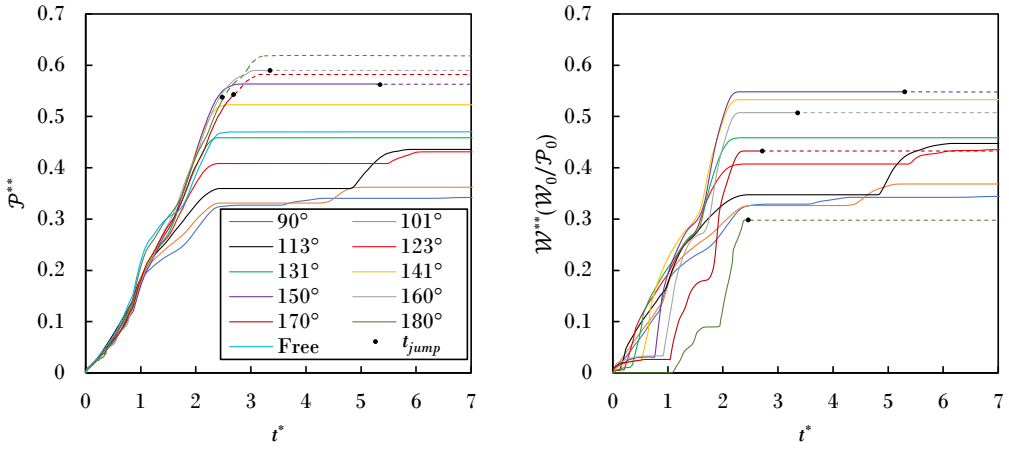

Figure 1.10: Evolution of net swept areas: projected $\mathcal{P}^{**}$ (left) and wetted $\mathcal{W}^{**}(\mathcal{W}_0/\mathcal{P}_0)$ (right). Solid circles indicate drop jumping, at which wetted trajectories terminate (extensions, dashed).

observed in time. Although the progression of $\mathcal{W}^{**}(\mathcal{W}_0/\mathcal{P}_0)$ varies with differing wettabilities early on due to the different times of liquid bridge impingement with the surface, more than $\sim$ 80% of $\mathcal{W}^{**}(\mathcal{W}_0/\mathcal{P}_0)$ is swept by $t^* \sim 2.5$ in all cases. See Appendix A.2 for select videos illustrating the sweeping behavior in time, Videos A.2 and A.3.

We end this section with a summary of the significance of these results to engineering applications. Heat transfer coefficients for dropwise condensation are an order-of-magnitude greater than those for filmwise condensation, as is well known[53]. Dropwise condensation on hydrophobic surfaces can be maintained by effective coalescence sweeping strategies. Sweeping of wetted area removes recently nucleated drops, while sweeping of projected area induces coalescence of larger-scale drops. Eventually, drops grow large enough via coalescence to be detached via gravity-driven sliding which results in additional sweeping of surface area. These mechanisms act to delay or avoid filmwise condensation.

In addition to use in dropwise condensers, hydrophobic surfaces are attrac-

tive for self-cleaning surfaces, anti-frost coatings, and water harvesters, among others. On self-cleaning surfaces, enhanced hydrophobicity may assist with the collection of contaminants and other foreign debris by increasing the amount of area swept by the liquid phase. Similarly, for anti-frost coatings, a greater extent of sweeping via increased surface hydrophobicity may improve the removal efficiency of drops before freezing can occur. For water harvesting devices, coalescence is responsible for growing drops to a critical size for departure and collection. Larger swept areas can enhance growth rates, as in dropwise condensation, and lead to more frequent drop departure and higher rates of collection.

1.8 Concluding Remarks

Sweeping by sessile drop coalescence is studied in an idealized setup. Coalescence between two identical drops, initially at rest on a flat and non-porous hydrophobic substrate, is initiated by arranging the drops to just touch. We first validate our simulations against experiment for three different material systems and then computationally study swept areas for increasing θ_0 in the hydrophobic and superhydrophobic regimes. The systems studied are characterized by initial contact angles $90^\circ \leq \theta_0 \leq 180^\circ$ and contact angle hysteresis $\Delta\theta = 15^\circ$. Our post-processing interpretation of the computations uses the hydrodynamic theory of moving contact lines.

- Simulation modeling of the experiment presents a number of challenges including rapidly moving contact lines, inertially-dominated dynamics, and possible drop jumping. Using an empirically-based model of moving

contact lines, our simulation reasonably captures the observed swept area evolutions for water on three different substrates, with no fitting parameters.

- In this work, coalescence is driven solely by excess interfacial energy as the event starts and ends at rest. Initially, interfacial energy is converted to kinetic energy and then back again while simultaneously being degraded by bulk viscous and contact line dissipation. Eventually, kinetic energy approaches zero and the interfacial energy release is expected to equal the total dissipation. We track energies and losses in time with the energy balance, Equation (1.15), ultimately evaluated at t_∞ (hydrophobic cases) or t_{jump} (superhydrophobic cases). For all simulation events reported, the left- and right-hand sides of Equation (1.15) agree to better than 15%.

- As wettability decreases (θ_0 increases), wetted area initially tracks projected area up to about $\theta_0 = 150°$, at which angle they begin to deviate. Soon after, wetted area reaches a maximum and turns over owing to a smaller wetted perimeter and possibly early termination of the evolution by drop jumping. At jumping, wetted perimeter vanishes by shrinking to a point. Interestingly, the onset of jumping happens to coincide with the commonly accepted start of the superhydrophobic regime, $\theta_0 = 150°$. Our observation of coalescence-induced drop jumping in the superhydrophobic regime is consistent with other studies[95,101].

- Viscosity is the only form of dissipation operative in free drop coalescence while sessile drop coalescence additionally has contact friction. Contact

line dissipation can contribute more than half the total dissipation, according to our simulations, depending on wettability. It is perhaps surprising then that, by $\theta_0 = 130°$, the sessile drop $\mathcal{P}^{**}$ can exceed the free drop $\mathcal{P}^{**}$ and by $\theta_0 = 180°$, the sessile $\mathcal{P}^{**}$ exceeds the free $\mathcal{P}^{**}$ by more than 30%. One concludes that the increasing energy loss by contact line dissipation is outweighed by enhanced dynamical vigor owing to the higher center of mass (COM) that correlates with increasing θ_0, or decreasing wettability.

- The COM motion with and without substrate relates to jumping. For the free drop coalescence event, there is no net force in any direction exerted on the system. This implies, by Newton's law, that the system COM remains stationary throughout the event. With the introduction of the substrate, a vertical velocity component of the system COM motion becomes possible. That is, the liquid contact with the substrate introduces i) a pressure that acts vertically and ii) a contact line force around the perimeter due to surface tension, having a vertical component. As a consequence, the system COM can move upward even while its xy-projection remains stationary by no net horizontal force. In summary, jumping cannot occur obliquely and, to occur, must overcome the surface tension adhesion contribution at the contact line. This is increasingly likely to happen as wettability decreases (θ_0 increases), consistent with our predictions.

In closing, it is important to note that coalescence infrequently takes place between two identical sessile drops in practical applications. As such, future studies that investigate the effects of drop size and/or contact angle mismatch on sweeping would be of value. Additionally, the sweeping behavior of three or more drops with or without chain-reaction coalescence remains unexplored.

Open questions persist as to how the number of drops and their positioning affect coalescence sweeping. Finally, a parametric study of contact angle hysteresis $\Delta\theta$ would be of benefit to parse whether θ_0 or $\Delta\theta$ is the dominant parameter in determining the extent of coalescence-induced sweeping.

CHAPTER 2

SWEEPING BY SESSILE DROP COALESCENCE. PART 2: EFFECT OF CONTACT ANGLE HYSTERESIS

2.1 Abstract

The phenomenon of sweeping by sessile drop coalescence evolves complex wetted and projected area patterns on the support surface. Part 1 (Ludwicki & Steen, *Eur. Phys. J. Special Topics*, 2020, accepted) investigates how the wettability of the surface influences these swept area patterns by modifying the initial contact angle of the coalescing drops (θ_0) on various hydrophobic supports. It is found that the magnitude of θ_0 dictates the extent of coalescence sweeping, along with other liquid behaviors like out-of-plane drop jumping. Here, in Part 2, it is studied how a second wettability parameter, contact angle hysteresis ($\Delta\theta$), influences coalescence sweeping by employing numerical simulations. Contact angle hysteresis is incorporated into a volume of fluid method via the Kistler dynamic contact angle model. Depending on the combination of θ_0 and $\Delta\theta$ employed, sweeping is classified as either bulk dynamics-dominated or final rest state-dominated. With these classifications defined, swept areas are analyzed and interpreted for $\theta_0 > 90°$ over a range of $\Delta\theta$ values. Contact angle hysteresis is found to add an interesting complexity to the coalescence behavior, with various trends in the wetted and projected swept areas discussed. Ultimately, for $\Delta\theta$ versus θ_0, a line of demarcation distinguishes between the two sweeping regimes, and also for drop jumping behavior. This characterization of the surface wettability effect on sweeping by sessile drop coalescence has important implications pertaining to solid support design for a number of different

drop-based applications.

2.2 Introduction

During sessile drop coalescence, the merging process results in the solid support being swept by the liquid phase. Coalescence sweeping manifests as both wetted and projected areas, culminating in complicated patterns as the fluid dynamics progress the combining drops to a final rest state (Figure 2.1). For non-wetting and hydrophobic surfaces, where the initial contact angle $\theta_0 > 90°$, cumulative projected $\mathcal{P}_\infty$ and cumulative wetted $\mathcal{W}_\infty$ swept areas typically differ because the body of the liquid overhangs the wetted footprint during the coalescence event. Extent of sweeping depends on surface wettability, as determined by the solid-liquid-gas system, and is important to device performance in areas ranging from self-cleaning surfaces[63] to water harvesters[131] to dropwise condensers[66] which typically employ hydrophobic supports. Chapter 1 showed that the initial contact angle of the coalescing drops in the hydrophobic regime has a significant effect on sweeping due to differences in interfacial energy release and dissipation which, ultimately, affect kinetic energy availability for motions. However, the influence of contact angle hysteresis ($\Delta\theta$) on coalescence sweeping has yet to be investigated, as far as the author is aware.

Classically, contact angle hysteresis is defined as the difference in dynamic advancing and receding contact angles, $\Delta\theta \equiv \theta_a - \theta_r$, and specifies the stick-slip behavior of the three-phase contact line. In other research areas, for example studies of drop impact on a solid surface, increased $\Delta\theta$ has been shown to dampen fluid dynamics via early pinning of the liquid and increased dissi-

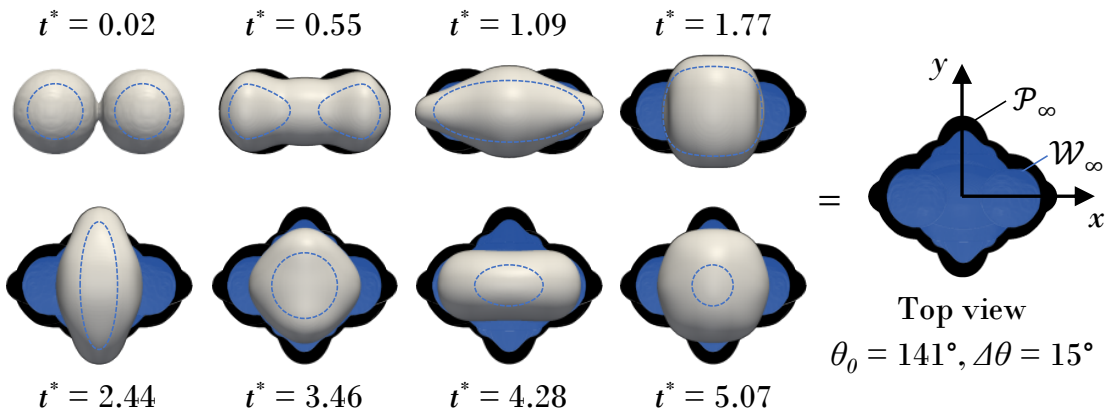

Figure 2.1: Evolution of wetted (blue) and projected (black) swept areas during binary sessile drop coalescence, resulting in wetted $\mathcal{W}_\infty$ and projected $\mathcal{P}_\infty$ cumulative swept areas (right). Wetted footprints are indicated by the dashed blue lines overlaying the bulk dynamics.

pation[132,133]. For drop vibration on a support, pinned versus partially mobile contact lines yield differing drop dynamics and oscillation frequencies[134–138]. Moreover, sliding drops adopt distinct topologies while in motion depending on the combination of θ_0 and $\Delta\theta$ employed[139–141]. As such, it is expected that varying $\Delta\theta$ will play a large role in influencing the dynamics of drop merging and, ultimately, coalescence sweeping and possible drop jumping.

Over the past two decades, sessile drop coalescence has been widely studied. Research topics range from growth of the meniscus bridge[69–75] to bulk shape evolution[22,60,76–81,110–112] to post-coalescence contact line relaxation[21,82–85]. Recently, coalescence induced out-of-plane drop jumping has received a majority of the focus through analytical, numerical, and experimental studies[28,29,49,86–109,142–146]. In regards to hysteresis effects on coalescence, the author is aware of a lone study from 2011 by Nilsson and Rothstein[61]. This paper experimentally investigates the influence of $\Delta\theta$ on binary sessile drop coalescence over

a range of impact velocities and impact angles. Three surfaces were employed for experiments; each had an advancing contact angle of $\theta_a = 150°$, while the receding contact angle θ_r was varied to satisfy $\Delta\theta = 3°$, 15°, or 30°. Increased $\Delta\theta$ was found to reduce deformations in the bulk fluid during the coalescence process. Also, depending on impact velocity and impact angle, coalescence behavior could be classified as oscillation dominated, rotation dominated, or mixed dynamics. It is noted that this paper did not mention or quantify swept areas and, in general, there is a lack of literature reported studies on the coalescence sweeping phenomenon. This work seeks to inform knowledge in this area.

In this paper, numerical simulations are performed to investigate the swept areas resulting from the coalescence of two identical sessile drops with no approach velocity. After introducing the numerical method and dynamic contact angle model, the influence of surface wettability on sweeping is explored by changing the contact angle hysteresis of the coalescing drops in the hydrophobic ($90° \leq \theta_0 < 150°$) and superhydrophobic ($\theta_0 \geq 150°$) regimes. Swept areas are quantified with trends discussed, and two sweeping regimes are distinguished that depend on the combination of $\Delta\theta$ and θ_0 employed. For $\Delta\theta$ versus θ_0, the simulations provide a boundary for the sweeping regimes, in addition to the jumping and non-jumping regimes. As far as the author is aware, this study is a first to parametrically study the influence of $\Delta\theta$ on sessile drop coalescence over a range of θ_0 values (equivalently, θ_a values) and to address its role in determining the extent of area swept. Additionally, this work investigates heretofore unstudied large hysteresis values during coalescence, up to $\Delta\theta = 90°$.

2.3 Numerical Method

The computational volume of fluid (VOF) method is more fully described in the accompanying work, Chapter 1, however a brief overview is provided here for completeness. OpenFOAM computational fluid dynamics software[121] is employed to simulate the pairwise coalescence of identical sessile drops. The interFoam VOF solver, applicable to incompressible, laminar, and two-phase fluid flow, is utilized. The solver is modified from its original state to remove artificial anti-diffusive surface fluxes; this has been previously shown to improve transient behaviors in capillary-dominated flows[54,102]. Material advection, momentum, and continuity equations are solved subject to the Kistler dynamic contact angle model[119]. The Kistler model has no fit parameters, requiring only a physically realistic choice of the dynamic contact angles θ_a and θ_r. Note that θ_0 does not appear explicitly in Kistler's formulation, although it is bound by $\theta_r < \theta_0 < \theta_a$.

Binary sessile drop coalescence is simulated via a 1.4 mm x 1.3 mm x 1.3 mm computational domain comprised of cubic cells with edge length $\epsilon = 10\,\mu$m (Figure 2.2). At the no-penetration solid contact boundary, the Kistler dynamic contact angle model is imposed with user-specified values of θ_a and θ_r. The open-flow boundaries are initialized as fixed pressure and zero velocity gradi-

Table 2.1: Fluid properties of water, subscript l, and air, subscript g, used in the simulations: density (ρ), viscosity (μ), and surface tension (σ).

ρ_l (kg/m^3)	ρ_g (kg/m^3)	μ_l (mPa$\cdot$s)	μ_g (mPa$\cdot$s)	σ_{lg} (J/m^2)
998.0	1.204	0.998	0.0181	0.072

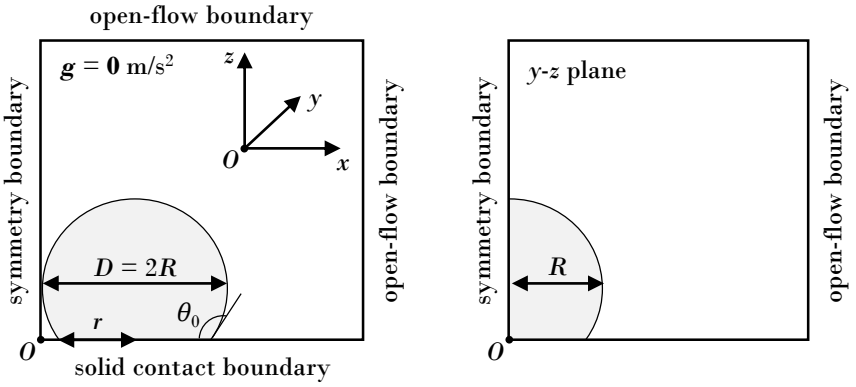

Figure 2.2: 3D computational domain with boundaries (solid contact, open-flow, or symmetry) as indicated.

ent. Fluid properties are for a water-air system at room temperature, see Table 2.1. Model validation versus experiment is also provided in the accompanying work, Chapter 1, along with a description of the numerical solving technique employed in OpenFOAM. As a further confirmation of OpenFOAM performance, Figure B.1 of Appendix B shows that trajectories in the fluid dynamics collapse when a set of non-dimensional numbers, which coalescence motions depend parametrically on, are held constant.

2.4 Sweeping Metrics and Energy Accounting

A cumulative projected swept area $\mathcal{P}_\infty$ is outlined as drops coalesce and progress to a rest state, Figure 2.1. The amount of net projected swept area, as normalized by the initial projected area $\mathcal{P}_0 = 2\pi R^2$, is

$$\mathcal{P}^{**} = \frac{\mathcal{P}_\infty - \mathcal{P}_0}{\mathcal{P}_0} \tag{2.1}$$

where, for two identical coalescing drops, R is the initial radii of the drops. Similarly, a cumulative wetted swept area $\mathcal{W}_\infty$ is traced in time, Figure 2.1.

The amount of net wetted swept area, as normalized by the initial wetted area $\mathcal{W}_0 = 2\pi r^2$, is

$$\mathcal{W}^{**} = \frac{\mathcal{W}_\infty - \mathcal{W}_0}{\mathcal{W}_0} \tag{2.2}$$

with $r = R\sin\theta_0$ the base wetted radius of a drop. To enable direct comparison with $\mathcal{P}^{**}$, the regularized form of the net wetted swept area, $\mathcal{W}^{**}(\mathcal{W}_0/\mathcal{P}_0)$, is utilized going forward. Maximum extensions in the x-and y-axes for the cumulative swept areas are also used as a metric to inform sweeping, Figure 2.3. As discussed later, maximum projected extensions are normalized by $2R$ while wetted extensions are normalized by $r + R$. Henceforth, all non-dimensional parameters are indicated by an asterisk superscript (*).

To elucidate coalescence sweeping behavior, energy transients are analyzed in the computational domain. For a coalescence event, reversible energy changes in interfacial and kinetic energy must balance dissipation in time. Interfacial energy ($\mathcal{A}$) is defined as the sum of the solid-liquid (sl), liquid-gas (lg), and solid-gas (sg) interfacial areas, A, weighted by their respective surface energies,

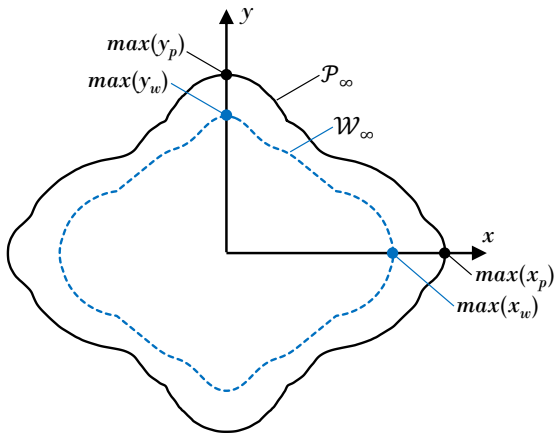

Figure 2.3: Definition sketch: maximum x- and y-axis extensions of the wetted (subscript w) and projected (subscript p) cumulative swept areas.

σ, yielding

$$\mathcal{A}(t) = A_{sl}(t)\sigma_{sl} + A_{lg}(t)\sigma_{lg} + A_{sg}(t)\sigma_{sg}. \tag{2.3}$$

Kinetic energy ($\mathcal{K}$), defined in the standard way, is evaluated over the combined volume of the liquid and gas phases (V) as

$$\mathcal{K}(t) = \int_V \frac{1}{2}\rho(t)\left(\boldsymbol{u}(t)\cdot\boldsymbol{u}(t)\right)dV \tag{2.4}$$

where $\boldsymbol{u} = (u_x, u_y, u_z)$ is the velocity vector and dV is the volume of a mesh element. Finally, dissipation ($\overline{\mathcal{D}}$) has contributions from contact line motion and bulk viscosity,

$$\overline{\mathcal{D}}(t) = \int_0^t \left(\mathcal{D}_\theta(t) + \mathcal{D}_\mu(t)\right)dt, \tag{2.5}$$

where $\mathcal{D}_\theta = \int_\gamma \sigma_{lg}(\cos\theta_e - \cos\theta)U_{CL}\,d\gamma$ is the contact line dissipation rate and $\mathcal{D}_\mu = \int_V \mu\,\Phi\,dV$ is the viscous dissipation rate[130]. Here, γ is contact line arc length, θ_e is equilibrium contact angle from the Young-Dupré equation, θ is dynamic contact angle, U_{CL} is contact line velocity, and Φ is the viscous dissipation function. For a coalescence event starting at rest, the energy balance is

$$\Delta\mathcal{A}(t) + \mathcal{K}(t) + \overline{\mathcal{D}}(t) = 0 \tag{2.6}$$

with notation $\Delta\mathcal{A}(t) \equiv \mathcal{A}(t) - \mathcal{A}(t=0)$. In the Results and Discussion section, time t is scaled by the inertial-capillary timescale $\tau = (\rho_l R^3/\sigma_{lg})^{1/2}$.

2.5 Results and Discussion

2.5.1 Parametric Study

For the parametric study of $\Delta\theta$ influence on coalescence sweeping, Table 2.2 summarizes the surface wettability conditions employed in the simulations. Ini-

Table 2.2: Simulation parameters: surface wettability θ_0 and $\Delta\theta$; initial drop diameter D. Advancing and receding contact angles are, respectively, $\theta_a = \theta_0 + 5°$ and $\theta_r = \theta_a - \Delta\theta$.

θ_0 (°)	$\Delta\theta_1$ (°)	$\Delta\theta_2$ (°)	$\Delta\theta_3$ (°)	$\Delta\theta_4$ (°)	D (mm)
113	15	30	45	90	0.80
123	15	30	45	90	0.76
131	15	30	45	90	0.74
141	15	30	45	90	0.72
150	15*	30	45	90	0.71
160	15*	30	45	90	0.71
170	15*	30*	45	90	0.71

tial contact angles range from $\theta_0 = 110°$ to 170°, while contact angle hysteresis is set to $\Delta\theta = 15°$, 30°, 45°, or 90°. In all cases, $\theta_a = \theta_0 + 5°$ and $\theta_r = \theta_a - \Delta\theta$. In total, 28 simulations were run. Dimensionless groups Ohnesorge ($Oh \ll 1$) and Capillary ($Ca \ll 1$) indicate liquid inertia and surface tension are dominant over viscous effects, as typical for water drop coalescence at this scale. Additionally, Reynolds number ($Re < 300$) confirms laminar flow in all simulations. Lastly, with gravitational effects neglected, Figure 2.2, Bond number (Bo) is zero. Coalescence induced drop jumping is noted to occur for i) $\theta_0 \geq 150°$ & $\Delta\theta = 15°$ and ii) $\theta_0 = 170°$ & $\Delta\theta = 30°$, corresponding here to four instances (* in Table 2.2).

2.5.2 Modes of Sweeping

Two modes of coalescence sweeping are distinguished based on the extension results obtained at different combinations of θ_0 and $\Delta\theta$. For cases where the

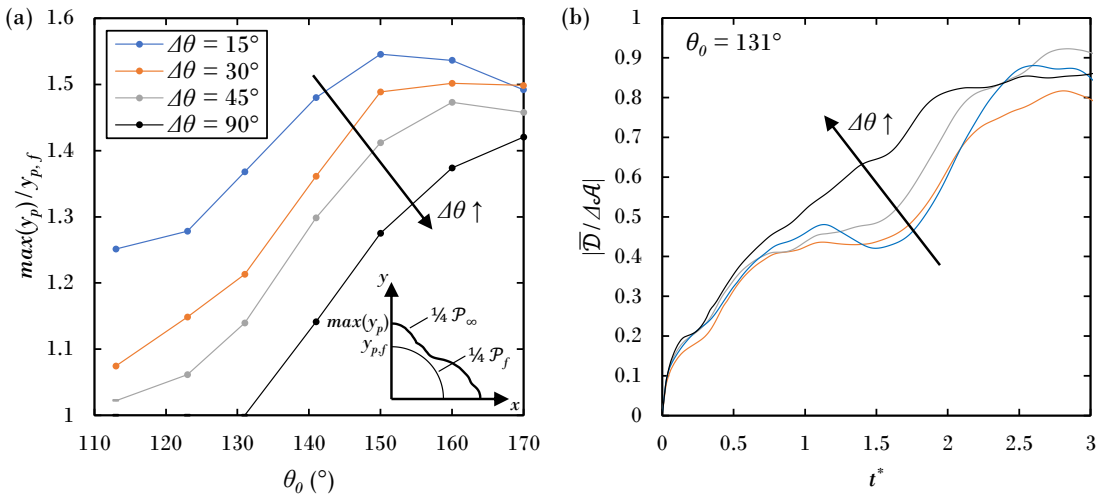

Figure 2.4: (a) Ratio of extensions, $max(y_p)/y_{p,f}$, for various θ_0 and $\Delta\theta$. Bulk dynamics-dominated sweeping = • symbol, final rest state-dominated sweeping = – symbol. (b) Dissipation fraction of the total interfacial energy release, $|\overline{\mathcal{D}}/\Delta\mathcal{A}|$, in time for $\theta_0 = 131°$.

maximum projected y-axis extension is approximately equal to the projected y-axis extension at final equilibrium, $max(y_p) \approx y_{p,f}$, sweeping is defined as 'final rest state'-dominated. For analysis related to this work, $max(y_p) \approx y_{p,f}$ if the values are within 2.5% of each other. In cases where $max(y_p) > y_{p,f}$, for example Figure 2.4a inset, the sweeping is considered 'bulk dynamics'-dominated. Figure 2.4a plots the ratio $max(y_p)/y_{p,f}$ versus θ_0 for $\Delta\theta = 15°, 30°, 45°$, and $90°$. As $\Delta\theta$ increases, $max(y_p)/y_{p,f}$ decreases indicating that higher contact angle hysteresis dampens the bulk fluid dynamics. Assessing dissipation percentage of the total interfacial energy release, it is found that dissipation increases with $\Delta\theta$ during $1.5 < t^* < 2.0$. This time frame, which corresponds to initial liquid expansion in the y-direction, immediately precedes the attainment of the maximum y-axis extensions[54]. Hence, with kinetic energy availability reduced due to increased dissipation during $1.5 < t^* < 2.0$, maximum y-axis extensions become muted and $max(y_p)/y_{p,f}$ decreases. An exemplary case of dissipation fraction of the to-

tal interfacial energy release is provided in Figure 2.4b for $\theta_0 = 131°$ at various $\Delta\theta$ values. Later, Section 2.5.5, a phase diagram is drawn to indicate the manifestation of the two sweeping regimes for $\Delta\theta$ vs. θ_0.

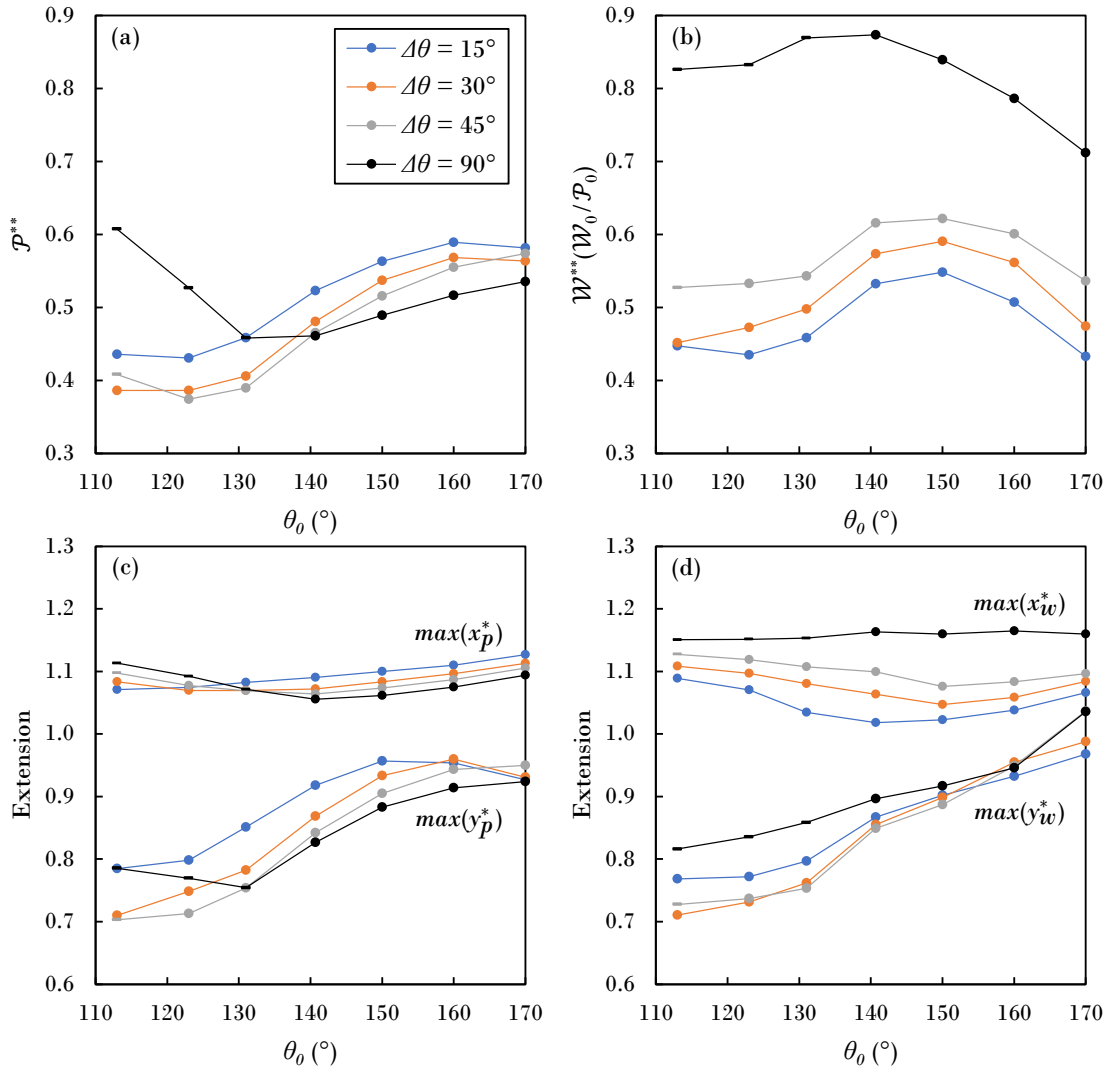

Figure 2.5: Effect of surface wettability, θ_0 & $\Delta\theta$, on swept areas and extensions: (a) net projected swept area $\mathcal{P}^{**}$, (b) regularized net wetted swept area $\mathcal{W}^{**}(\mathcal{W}_0/\mathcal{P}_0)$, (c) maximum projected extensions, and (d) maximum wetted extensions.

2.5.3 Swept Areas and Extensions

Sweeping and extension data for the sessile drop coalescence simulations are shown in Figure 2.5, while Figure 2.6 gives pictorial representations of the cumulative swept areas. Differences in projected swept areas manifest primarily from maximum extensions in the y-axis, as it is observed that i) $\mathcal{P}^{**} \propto max(y_p^*)$ and ii) $max(x_p^*) \approx$ constant. For bulk dynamics-dominated sweeping ($\bullet$ symbols in Figures 2.4, 2.5, 2.7, & 2.8), the net projected swept area $\mathcal{P}^{**}$ decreases as contact angle hysteresis $\Delta\theta$ increases owing, as previously mentioned, to increasing dissipation which reduces kinetic energy availability for the y-axis extensions that ultimately dictate sweeping. Conversely, for final rest state-dominated sweeping ($-$ symbols in Figures 2.4, 2.5, 2.7, & 2.8), $\mathcal{P}^{**}$ increases with $\Delta\theta$. In these cases, the liquid settles to a final conformation that sets the maximum y-axis extension. At fixed θ_0, higher $\Delta\theta$ values correspond to smaller receding contact angles θ_r (Table 2.2). Ultimately, for lower θ_r, the combining drops settle to a smaller final contact angle θ_f that has a correspondingly larger final projected diameter which acts to increase $\mathcal{P}^{**}$. In many cases, for final rest state-dominated sweeping, $\theta_f \leq \sim 90°$.

For net wetted swept areas, $\mathcal{W}^{**}(\mathcal{W}_0/\mathcal{P}_0)$ is always observed to increase with $\Delta\theta$ at fixed θ_0. At some level, this may be counterintuitive because increased $\Delta\theta$ is associated with a less mobile contact line. However, as discussed in the paragraph above, the merged liquid drops settle to larger rest footprint areas as a result of the lower θ_r value at increased $\Delta\theta$. This leads to additional wetted sweeping given the initial spacing that is present between the wetted footprints of the coalescing drops on hydrophobic supports, cf. Figure 2.6. As $\Delta\theta$ increases, note how the wetted swept area patterns become more rounded, in addition

to the broadening of the swept area near $max(x_w^*)$. Ultimately, $\mathcal{W}^{**}(\mathcal{W}_0/\mathcal{P}_0)$ is dominated more by final equilibrium than maximum extensions.

2.5.4 Wetted versus Projected Sweeping

As must be true, cumulative wetted sweeping is less than or equals cumulative projected sweeping ($\mathcal{W}_\infty \leq \mathcal{P}_\infty$) in all cases, with Figure 2.7a plotting $\mathcal{W}_\infty/\mathcal{P}_\infty$. Note that $\mathcal{W}_\infty$ approaches the value of $\mathcal{P}_\infty$ as θ_0 decreases and $\Delta\theta$ increases, when dynamical behavior has a reduced effect on cumulative sweeping and the final rest configuration has increased influence. Interestingly, in the bulk dynamics-dominated sweeping regime, $\mathcal{W}_\infty/\mathcal{P}_\infty$ trends linearly with θ_0 for $\Delta\theta = 15°$, $30°$, $45°$, and $90°$ with the slopes approximately identical. The linearity is surprising because of the complex (i.e. non-linear) effect θ_0 has on the evolution of various energies which ultimately dictate sweeping[54]. As an alternative means to compare wetted and projected sweeping, the ratio of net swept areas $(\mathcal{W}_\infty - \mathcal{W}_0)/(\mathcal{P}_\infty - \mathcal{P}_0)$ is plotted in Figure 2.7b. At any appreciable contact angle hysteresis ($\Delta\theta \geq 15°$), net wetted sweeping exceeds net projected sweeping except in a few select cases. For these, which correspond to $(\mathcal{W}_\infty - \mathcal{W}_0)/(\mathcal{P}_\infty - \mathcal{P}_0) < 1$, non-wetting behavior is compelled by $\theta_0 \geq 150°$ and a relatively low $\Delta\theta$. In addition, drop jumping sometimes occurs which terminates wetted sweeping while the projected swept area can still evolve. It is also observed that $(\mathcal{W}_\infty - \mathcal{W}_0)/(\mathcal{P}_\infty - \mathcal{P}_0)$ increases at larger $\Delta\theta$ values, with $(\mathcal{W}_\infty - \mathcal{W}_0)$ nearly exceeding $(\mathcal{P}_\infty - \mathcal{P}_0)$ by a factor of two at $\Delta\theta = 90°$ for $\theta_0 = 131° \,\&\, 141°$. For hydrophobic surfaces at higher hysteresis values, it is possible for $\mathcal{W}_\infty \approx \mathcal{P}_\infty$ while $\mathcal{W}_0 < \mathcal{P}_0$ leading to net wetted sweeping dominating net projected sweeping, cf. Figure 2.6.

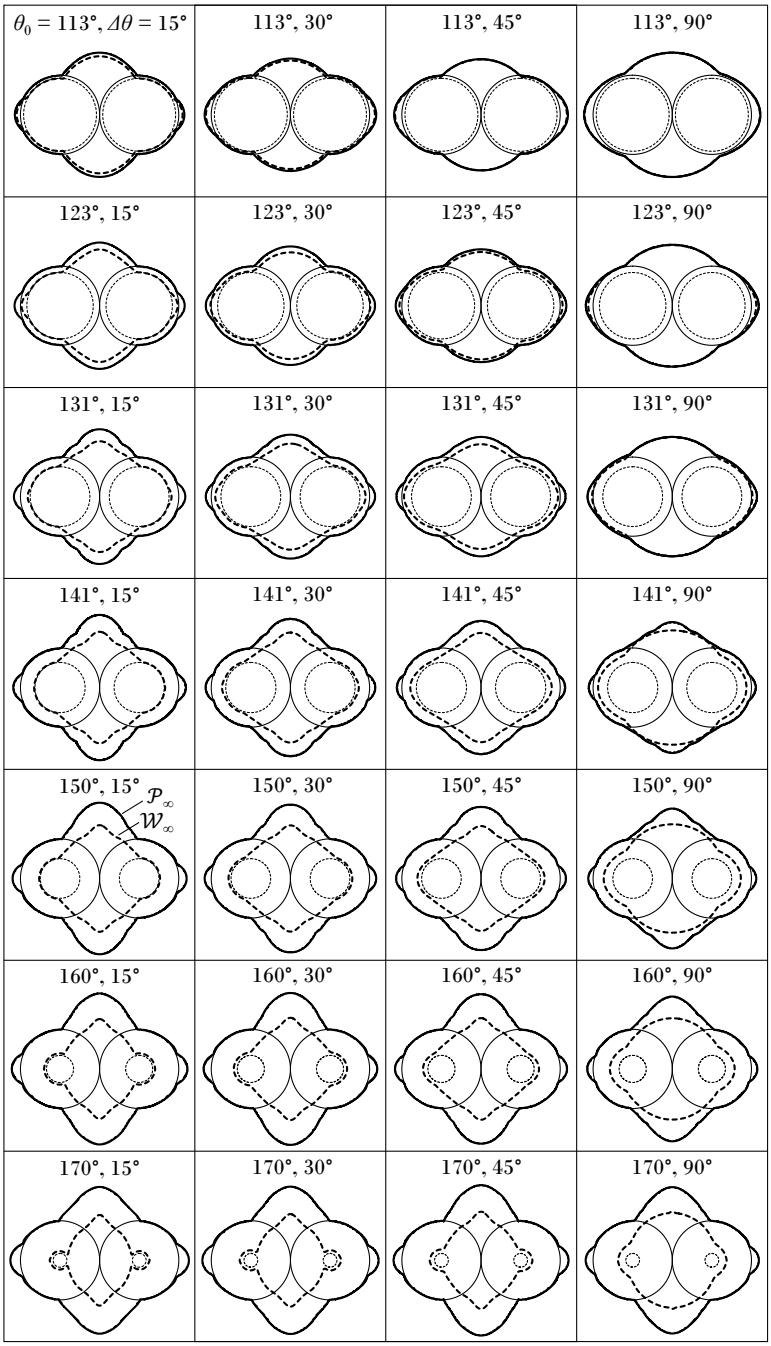

Figure 2.6: Cumulative swept areas for (θ_0, $\Delta\theta$): wetted $\mathcal{W}_\infty$ (thick dashed) and projected $\mathcal{P}_\infty$ (thick solid), with initial wetted (thin dashed) and initial projected (thin solid) areas, for reference. All areas are scaled, for comparison.

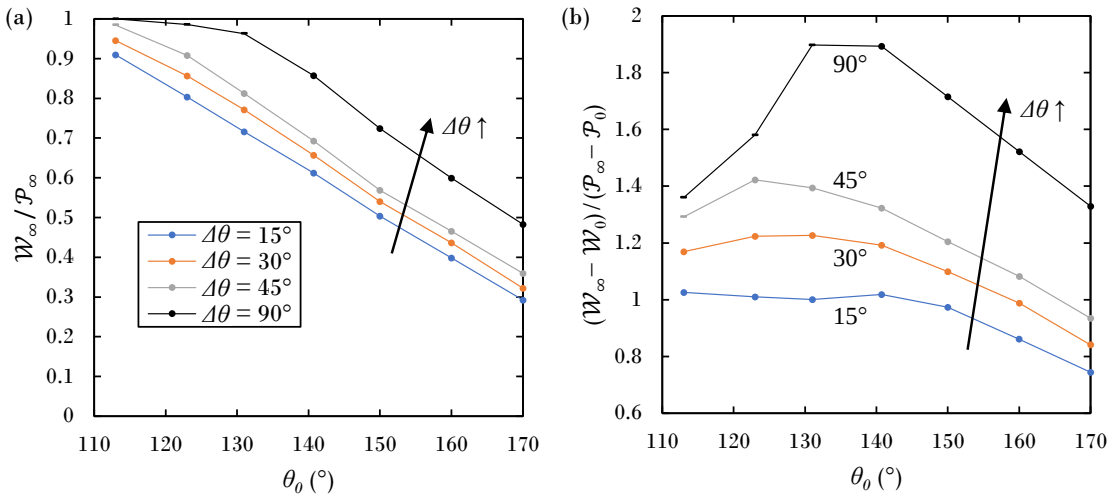

Figure 2.7: Ratio of wetted and projected areas: (a) cumulative $\mathcal{W}_\infty/\mathcal{P}_\infty$ and (b) net $(\mathcal{W}_\infty - \mathcal{W}_0)/(\mathcal{P}_\infty - \mathcal{P}_0)$.

2.5.5 Jumping and Non-Jumping Regimes

This computational study also allows the creation of a phase diagram for jumping versus non-jumping regimes when considering $\Delta\theta$ vs. θ_0 (Figure 2.8). Similar plots have been drawn for Oh vs. θ_0 at different density ratios (fixed viscosity ratio)[95] and drop size ratio vs. radius of the large drop at fixed wettability[101]. However, the author is not aware of a similar diagram for $\Delta\theta$ vs. θ_0 which is likely to be of utility to other researchers. Coalescence induced out-of-plane drop jumping is typically reported on superhydrophobic surfaces ($\theta_0 \geq 150°$) with ultra-low contact angle hysteresis ($\Delta\theta < 5°$)[87,90,93,96,100]. Simulations here predict jumping can also occur in cases where the hysteresis is relatively high, such as $\theta_0 = 170°$ and $\Delta\theta = 30°$, in addition to all superhydrophobic cases with $\Delta\theta = 15°$. The typical cutoff for jumping behavior, $\theta_0 = 150°$, as reported elsewhere[95], is also captured by the simulations. A rough boundary can additionally be drawn between the two sweeping regimes when considering $\Delta\theta$ vs. θ_0,

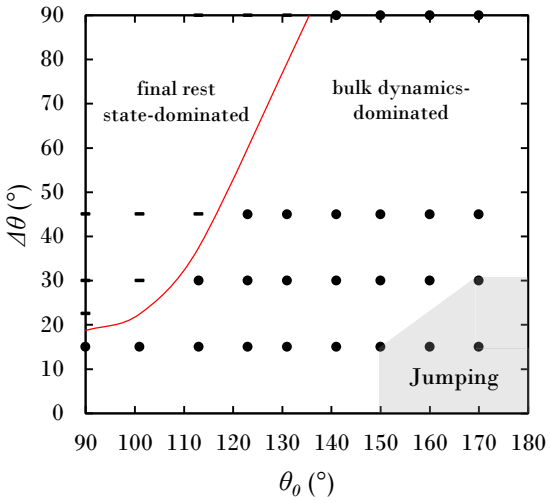

Figure 2.8: Regime boundaries: i) modes of coalescence sweeping, as separated by the red line. ii) jumping versus non-jumping coalescence, as separated by the shaded (gray) and non-shaded regions.

see Figure 2.8. Supplemental simulations were performed for $\theta_0 = 90°$ and 101° to fully fill out this line in the hydrophobic regime, as indicated, with $\theta_a = \theta_0 + 5°$ similar to the prior studies.

2.6 Concluding Remarks

Contact angle hysteresis $\Delta\theta$ is found to add another layer of complexity to sweeping behavior during sessile drop coalescence. In the previous study of binary sessile drop coalescence on hydrophobic supports with fixed $\Delta\theta = 15°$ [54], only bulk dynamics-dominated sweeping was observed. However, here, a final rest state-dominated sweeping mode was also identified for surfaces with high enough $\Delta\theta$. That is, the manifestation of different sweeping modes during coalescence depends on surface wettability via θ_0 and $\Delta\theta$. Largely, swept areas in the hydrophobic regime are dominated by bulk dynamics during the coales-

cence event, however exceptions do exist as identified here. From the results, a rough phase diagram was drawn that indicates the boundary between sweeping modes for $\Delta\theta$ versus θ_0. Additionally, a similar line of demarcation was generated for the jumping and non-jumping coalescence regimes with higher $\Delta\theta$ found to restrict jumping on superhydrophobic surfaces. The following trends in the swept areas were also noted:

- Depending on the mode of sweeping, net projected swept areas $\mathcal{P}^{**}$ trend either with (final rest state-dominated) or against (bulk dynamics-dominated) increasing contact angle hysteresis $\Delta\theta$. Conversely, in all cases, net wetted swept areas $\mathcal{W}^{**}$ increase with higher $\Delta\theta$ despite the reduced mobility of the three-phase contact line.

- For any appreciable amount of contact angle hysteresis, $\Delta\theta \geq 15°$, net wetted sweeping ($\mathcal{W}_\infty - \mathcal{W}_0$) exceeds net projected sweeping ($\mathcal{P}_\infty - \mathcal{P}_0$) except in select superhydrophobic cases where $\theta_0 \geq 150°$ and $\Delta\theta$ is relatively low.

- By plotting the ratio of cumulative wetted to cumulative projected swept areas, $\mathcal{W}_\infty/\mathcal{P}_\infty$, it is shown that $\mathcal{W}_\infty$ approaches $\mathcal{P}_\infty$ at reduced θ_0 and increased $\Delta\theta$.

In terms of which wettability parameter dictates sweeping behaviors, $\Delta\theta$ or θ_0, it is dependent on the swept area being considered, $\mathcal{P}_\infty$ or $\mathcal{W}_\infty$, and where $(\Delta\theta, \theta_0)$ falls in the wettability phase space. In some cases, a 10° step in θ_0 minimally changes $\mathcal{P}_\infty$ and $\mathcal{W}_\infty$ while a comparable step in $\Delta\theta$ has a more profound effect. In other cases, the opposite can be true. Moreover, $\mathcal{P}_\infty$ and $\mathcal{W}_\infty$ do not always respond similarly to changes in the wettability parameters. Clearly, depending on $(\Delta\theta, \theta_0)$, there is a complexity to the evolutions of interfacial, dissipative,

and kinetic energies which ultimately determine the coalescence dynamics for sweeping.

For future work, further assessing the validity of sessile drop coalescence simulations with high $\Delta\theta$ and low θ_r is of interest. In experiments, combining liquid drops can settle to a non-spherical cap rest shape, for example an ellipsoid, when hysteresis is large and/or initial contact angle is low[21,22]. It is necessary to understand how such behaviors affect cumulative sweeping, and if they can be accurately captured by simulation. Also, a more rigorous criteria for predicting coalescence induced drop jumping is of interest. Perhaps there exists an escape velocity, analogous to a rocket moving out of a gravity well, where upward liquid momentum overcomes substrate adhesion during the coalescence process. It is predicted that this escape velocity would be dependent on the wettability of the surface employed.

CHAPTER 3

SWITCHABLE WETTABILITY FOR CONDENSATION HEAT TRANSFER

(this Chapter is published in *ACS Appl. Mater. Interfaces*[31])

3.1 Abstract

Condensation proceeds as dropwise or filmwise depending on the wettability of the condensing surface. These two modes of condensation have disparate heat transfer coefficients, with dropwise often exceeding filmwise. This work reports a surface with switchable superhydrophilic to hydrophobic wetting behavior that can exhibit both modes of condensation. Relative to the highly-wetting state which yields filmwise condensation, the non-wetting state exhibits dropwise condensation and twice the heat transfer coefficient. Relevance to thermal management is additionally discussed.

3.2 Introduction

Vapor condensation to liquid is a phase change heat transfer process common to a number of applications such as power generation[147], water desalination[148], and refrigeration[149]. The phase change is driven by a temperature difference between the vapor and condensing surface, often referred to as the degree of subcooling[53]. Depending on the chemistry and physical texturing of the condensing surface, which specify its wettability, the mode of condensation evolves as either discrete drops or a continuous film[32]. It is well established

that dropwise condensation can enhance the condensation heat transfer coefficient by up to an order-of-magnitude compared with the filmwise mode[150,151]. Since condensation typically occurs on surfaces with constant or unchanging wettability, only a single mode of condensation is possible at a particular subcooling which locks in one heat transfer coefficient[152]. In this work, we report a surface with temperature-responsive wettability that can achieve both filmwise and dropwise condensation over a range of common heat fluxes. Correspondingly, switching to the dropwise mode realizes a factor of two improvement in condensation heat transfer coefficient.

Switchable condensation heat transfer performance is relevant to thermal management applications. For example, in spacecraft two-phase flow thermal control systems (e.g. heat pipes, loop heat pipes, and mechanically-pumped loops), the radiator/condenser section is sized for the maximum heat load in the warmest anticipated environment[153]. As a result, when these two-phase systems are operated at reduced heat loads and/or in colder environments, the radiator/condenser is oversized for the reduced heat rejection needs[154,155]. Consequently, unless the condenser has variable heat transfer capabilities, it transfers more thermal energy than desired during lower heat load demands. Variable heat transfer capabilities would reduce energy waste and, in extreme cases, prevent drastic temperature changes in the working fluid that may in-

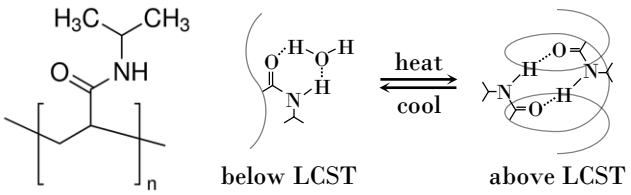

Figure 3.1: Structural formula of PNIPAAm and its reversible conformation changes below and above the LCST.

hibit the heat transfer device from functioning properly. NASA has highlighted the importance of such devices in its Technology Roadmaps[156], indicating that variable heat transfer capabilities would be candidate technologies for enabling human exploration missions beyond low-Earth orbit, say, to asteroids or the Mars system.

A variety of switchable wettability surfaces have been reported over the years, with actuation stimuli including light[157], strain[158], electrical potential[159], and pH[160]. This work utilizes a surface coated with the temperature-responsive material poly(N-isopropylacrylamide), or PNIPAAm for short, Figure 3.1. PNIPAAm exhibits a reversible and abrupt conformation change at a lower critical solution temperature (LCST) of approximately 32°C in water[161–163]. Below the LCST, the polymer adapts an extended state and exposes its polar −C=O and −N−H groups. These polar groups are of high surface energy and render the polymer hydrophilic[164]. Conversely, above the LCST, the polymer chain collapses due to intramolecular hydrogen bonding between the −C=O and −N−H groups. This renders the polymer hydrophobic as the exposed methyl-terminated backbone is of low surface energy[165]. When deposited on a smooth or non-textured surface, PNIPAAm exhibits water static contact angles of $\theta_{static} \approx 60°$ below and $\approx 90°$ above the LCST[166]. To amplify the effects of the PNIPAAm surface chemistry and thereby produce a wider shift in the wetting contact angles, researchers have deposited PNIPAAm onto micro- and/or nano-textured surfaces to achieve superhydrophilic to superhydrophobic transitions[164,166]. Historically, PNIPAAm has been discussed in many contexts[167] ranging from drug delivery[168] to chemical separations[169] to biofilm release[170]. However, we are unaware of previous PNIPAAm application to areas in heat transfer such as condensation.

3.3 Surface Fabrication

In pursuing switchable filmwise-dropwise condensation, a PNIPAAm-grafted surface with superhydrophilic to hydrophobic wetting transitions was developed. This was achieved by grafting PNIPAAm onto a nanostructured copper oxide surface. The nanostructures are grown on solid copper according to the wet chemical oxidation technique of Nam and Ju, Type I[171]. During oxidation, a thin (100s of nm) copper (I) oxide layer first grows that is then covered with a dense array of needle-like copper (II) oxide nanostructures[172]. To prepare the nanostructures for polymerization, a monolayer of the polymerization initiator (3-trimethoxysilyl)propyl 2-bromo-2-methylpropionate (Gelest Inc.) is first deposited onto the surface via vapor phase silanization. The −Cu−O−Si− bonds formed via the silanization process are known to be of high stability under a variety of adverse conditions, including boiling water[173]. PNIPAAm is then grafted from the initiator layer via an atom transfer radical polymerization (ATRP) employing the activators regenerated electron transfer (ARGET) mechanism[174]. For this ARGET-ATRP reaction, ascorbic acid is used as the reducing

Table 3.1: Chemical composition of the polymerization solution used to synthesize the surface-grafted PNIPAAm brushes via ARGET-ATRP. The reaction was performed at room temperature.

Chemical Component	Amount
N-isopropylacrylamide	0.8 M
Copper (II) bromide	0.5 mM
N,N,N′,N″,N″-pentamethyldiethylenetriamine	3.3 mM
Ascorbic acid	7.0 mM
Water/methanol	1:1 v/v

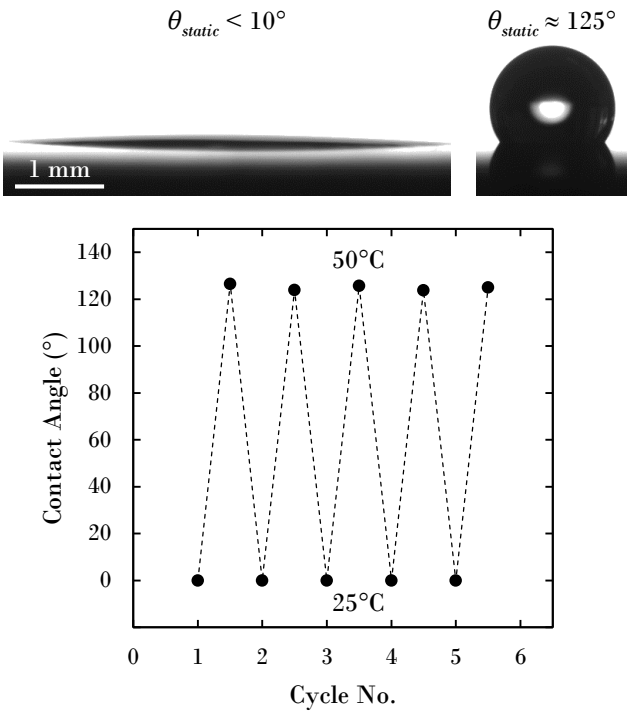

Figure 3.2: Switchable wettability: (top left) pure spreading, below the LCST. (top right) hydrophobicity, above the LCST. (bottom) reversibility of the water contact angle below, 25°C, and above, 50°C, the LCST.

agent[175]. After a 60 minute polymerization time using the conditions listed in Table 3.1, the surface exhibits switchable superhydrophilic (below LCST) to hydrophobic (above LCST) wetting behavior with respective static contact angles of $\theta_{static} < 10°$ and $\theta_{static} \approx 125°$ (Figure 3.2). Above the LCST, the dynamic contact angles are advancing $\theta_a = 130°$ and receding $\theta_r = 20°$. Dynamic contact angles are not reported below the LCST given the superwetting nature of the surface. Finally, based on previous studies with a similar polymerization scheme[175], the PNIPAAm brush thickness is estimated to be $O(100\text{ nm})$.

3.4 Condensation Experiment

To quantify the condensation heat transfer performance on the temperature-responsive surface, oxygen-free copper tubes (C122 type, 99.9% purity) were nanostructured and then grafted with PNIPAAm according to the previous paragraph. Tubing was of outer diameter D_o = 6.35 mm, inner diameter D_i = 3.86 mm, and length $L \approx$ 13.5 cm with the functionalization performed on the outer tube surface. Round tubing was chosen as it is a common geometry employed in heat exchangers, while copper is compatible with water-steam systems. Ultimately, the sample tube was plumbed into a fluid loop housed inside a custom condensation chamber at the NASA Goddard Space Flight Center, a chamber typically used for simulating deep-space conditions. By flowing a coolant through the fluid loop via a recirculating chiller, condensation of vapor on the outer tube surface could be achieved, Figure 3.3. Prior to steam introduction, the chamber was evacuated via a vacuum pump to a pressure $P < 0.1$ Pa as the presence of non-condensable gases masks true operating behavior. Indeed, Ma et al.[176] have shown that condensation heat transfer performance can be significantly degraded at non-condensable gas concentrations as low as 0.5%. Also, by evacuating non-condensable gases, we achieve experimental conditions consistent with other studies thereby allowing a fair comparison of condensation heat transfer data.

During condensation, measurement of the cooling fluid temperature at the inlet and outlet of the test section (T_{in} & T_{out}, respectively), vapor saturation temperature T_s, and cooling fluid volumetric flow rate $\dot{Q}$ allows calculation of the overall heat transfer coefficient $\bar{U}$. Note that $\bar{U}$ is measured from saturated vapor to cooling fluid and is deduced by setting two forms of the heat transfer

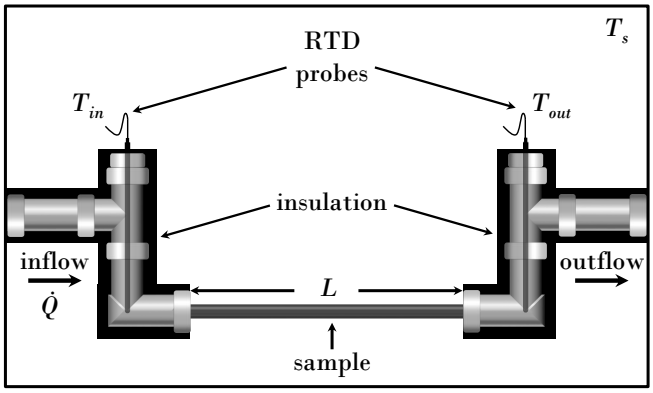

Figure 3.3: Condensation chamber schematic: flow loop with sample section housed inside a vacuum enclosure. Resistance temperature detector (RTD) probes (Class 1/10DIN, Omega Engineering Inc.) measure T_{in} and T_{out}, an integrated flow meter (104-8, McMillan Co.) measures $\dot{Q}$, and a chamber pressure sensor (UNIK 5000, Druck Ltd.) measures the vapor saturation pressure which is then converted to T_s using a best-fit polynomial to experimental data[1]. Electrical outputs from the measurement devices are sent to a digital multimeter operated at 6½-digit resolution (PXIe-4081, National Instruments Co.) for data acquisition.

rate equal to each other,

$$\rho_l \dot{Q} C_p (T_{out} - T_{in}) = \bar{U} A_o \, \Delta T_{LMTD}, \tag{3.1}$$

where ρ_l is the cooling fluid density, C_p is the cooling fluid specific heat capacity, $A_o \equiv \pi D_o L$ is the sample tube outer surface area, and ΔT_{LMTD} is the log mean temperature difference defined as

$$\Delta T_{LMTD} = \frac{(T_s - T_{in}) - (T_s - T_{out})}{\ln\left(\frac{T_s - T_{in}}{T_s - T_{out}}\right)}. \tag{3.2}$$

Rearrangement of Equation (3.1) then gives

$$\bar{U} = \frac{\rho_l \dot{Q} C_p}{A_o} \ln\left(\frac{T_s - T_{in}}{T_s - T_{out}}\right), \tag{3.3}$$

which allows $\bar{U}$ to be specified solely from known parameters and experimental measurements. The condensation heat transfer coefficient h, taken from satu-

rated vapor to tube outer surface, is then determined via $\bar{U}$ by eliminating thermal contributions from copper (I) oxide conduction, copper tube conduction, and cooling fluid convective heat transfer. Due to the thinness of the copper (I) oxide layer and its relatively high thermal conductivity[177], the corresponding temperature drop is low and can be neglected yielding

$$h = \left(\frac{1}{\bar{U}} - \frac{A_o}{A_i h_i} - \frac{A_o \ln (A_o/A_i)}{2\pi L k} \right)^{-1} \tag{3.4}$$

where $A_i \equiv \pi D_i L$ is the sample tube internal surface area, k is the thermal conductivity of copper, and h_i is the convective heat transfer coefficient of the cooling fluid. Here, h_i is estimated using the Gnielinski correlation which is valid for turbulent pipe flow[178]. Note that thermal resistances from the copper (II) oxide nanostructures and attached polymer are not included since drops are known to form in a partially wetting morphology on such features[40].

In this work, condensation heat fluxes are considered low ($q'' < 100$ kW/m^2) and correspond to small outlet to inlet temperature differences $\Delta T \equiv T_{out} - T_{in}$. For a working fluid of distilled water with $\dot{Q} \approx 3.5$ L/min (Reynolds number $Re > 15{,}000$), $\Delta T < 1$°C in all reported experiments. As such, high-accuracy measurement devices and a precision data acquisition system were needed to minimize uncertainty in the heat transfer calculations (Figure 3.3). Uncertainty associated with T_{in}, T_{out}, and T_s is $\delta T < \pm 0.05$°C, while for $\dot{Q}$ it is $\delta \dot{Q} < \pm 0.05$ L/min. See Appendix C.1 - C.4 for further details on the experimental apparatus and its operation, along with additional information related to the uncertainty analysis.

3.5 Results and Discussion

For condensation below the LCST, filmwise condensation ($\bar{U}_{filmwise} = 6.6 \pm 0.8$ kW/m^2 K) was observed and is attributed to the superhydrophilicity of PNIPAAm in its extended conformation (Figure 3.4, left). Conversely, condensation above the LCST evolved to a flooded form of dropwise condensation ($\bar{U}_{flooded} = 10.9 \pm 1.1$ kW/m^2 K) characterized by highly pinned drops with irregular shapes (Figure 3.4, right). These types of drops arise due to the selective nucleation of liquid within the nanostructures due to a lower energy barrier versus nucleation on the nanostructure tips[179]. Condensate initially fills the array of nanostructures and eventually bursts outward[180] to create low contact angle drops with high hysteresis on the hydrophobic surface conformation.

Figure 3.5 plots the condensation heat transfer coefficient versus heat flux, above ($h_{flooded} \approx 40$ kW/m^2 K) and below ($h_{filmwise} \approx 10$ to 20 kW/m^2 K) the LCST. The horizontal and vertical bars in this figure indicate uncertainty in the heat transfer data. The uncertainty analysis employed uses the standard method of the International Bureau of Weights and Measures, accounting for both Type A and Type B uncertainties and their propagation[181]. For h, uncertainty bars above the LCST are larger than below the LCST as dictated by the increased

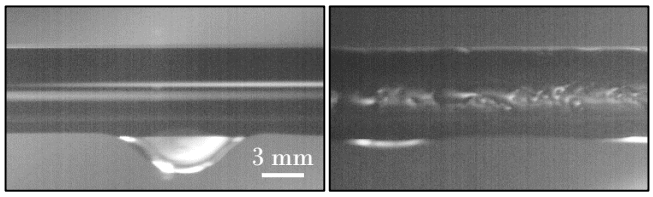

Figure 3.4: Switchable condensation: (left) filmwise condensation, below the LCST. (right) flooded dropwise condensation, above the LCST. Same scale bar as at left.

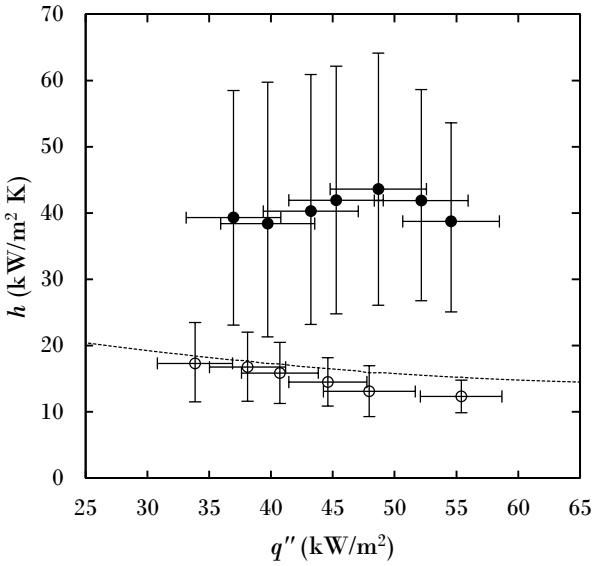

Figure 3.5: Switchable condensation: h versus q'' for temperatures above (• symbol) and below (◦ symbol) the LCST. The dashed line is the Nusselt model for filmwise condensation on a horizontally-oriented tube.

magnitude of $\bar{U}$ and its larger uncertainty. It is observed that the flooded dropwise condensation above the LCST gives an approximately two- to three-times improvement in the condensation heat transfer coefficient at a given heat flux versus filmwise condensation below the LCST. This is because a continuous liquid film has higher thermal resistance than a population of discrete drops. The results for flooded dropwise condensation are in excellent agreement with those reported by Miljkovic et al. ($h_{flooded} = 44 \pm 6$ kW/m^2 K) using a similar experimental system[6]. Additionally, the filmwise condensation data is in agreement with the experimentally verified heat transfer model developed by Nusselt for a horizontal tube[182], Figure 3.5.

Further enhancements in the dropwise condensation heat transfer coefficient and, hence, the effectiveness of switching may be feasible by rational design of the switchable wettability surface. Dropwise condensation with highly-mobile

drops can show an increase in the heat transfer coefficient ($h_{dropwise}$ = 75 ± 15 kW/m^2 K[183]) via the rapid refreshment of the condensing surface for renucleation by way of fast drop shedding. Similarly, jumping-drop condensation on superhydrophobic surfaces increases the heat transfer coefficient ($h_{jumping}$ = 92 ± 12 kW/m^2 K[6]) by maintaining a population of small drops ($D \approx 15$ µm) that have high heat fluxes due to a reduced condensate conduction resistance[34]. The hydrophobic surface conformation would have to be engineered to sustain these forms of dropwise condensation rather than the flooded mode. Then, switching between filmwise and the more efficient dropwise modes would allow for variation by a factor of five- to ten-times of the condensation heat transfer coefficient.

3.6 Conclusions

In summary, a nanostructured copper oxide surface grafted with PNIPAAm was developed that exhibits switchable superhydrophilic to hydrophobic behavior depending on the surface temperature. This temperature-responsive wettability allowed steam condensation to manifest as either filmwise or flooded dropwise at identical heat fluxes, leading to differing heat transfer performance with $h_{flooded} \approx 2h_{filmwise}$. Our work contrasts to prior studies in that, historically, condensation has been performed on surfaces with unchanging wettability which fixes the heat transfer coefficient. Switchable wettability surfaces hold promise as a means to manipulate heat transfer during flow condensation in spacecraft two-phase flow thermal control systems, and may be of benefit to energy conservation in other thermal management systems. The future utilization of surfaces with temperature-responsive wettability may require

tailoring the LCST to the application, with preliminary studies in this direction already performed by others[184]. Temperature-responsive surfaces can be considered a form of passive control; for active control, one could employ a surface with, say, an electrical potential-responsive wettability (Appendix C.5). Switchable wettability surfaces could additionally be extended to boiling and evaporation applications where efficiencies also depend on surface wettability[185].

Author Contributions: JML conceived the initial idea of the research, while FLR and PHS guided the work. JML designed and fabricated the surfaces. JML and FLR built the experimental apparatus. JML carried out the experiments and analyzed the data. JML, FLR, and PHS wrote the paper.

JML = Jonathan M. Ludwicki, FLR = Franklin L. Robinson, PHS = Paul H. Steen

CHAPTER 4

HOW SURFACE WETTABILITY AFFECTS FUNDAMENTAL DROP PROCESSES DURING DROPWISE CONDENSATION

4.1 Abstract

In guiding the development of condensers that exhibit highly-efficient dropwise condensation, it is necessary to understand how the surface design influences fundamental drop processes that ultimately dictate the heat transfer performance. To this end, an analytical study of the effect of surface wettability on drop nucleation, growth, and departure processes is performed for steam dropwise condensation. The surfaces are assumed to have uniform wettability, that is a non-variable static contact angle (θ_0) and contact angle hysteresis ($\Delta\theta$). Favorable drop behaviors are predicted on lowly-hysteretic hydrophobic surfaces ($\theta_0 \rightarrow 90^\circ$ & $\Delta\theta \rightarrow 0^\circ$), contrary to recent efforts in the literature (e.g., see review articles by Ahlers et al.[186] and El Fil et al.[187]) which have sought superhydrophobic surfaces with low adhesion ($\theta_0 \geq 150^\circ$ & $\Delta\theta \rightarrow 0^\circ$) for potential condensation heat transfer improvements. For hydrophobic surfaces with low hysteresis, we perform analytical modeling to predict condensation heat transfer behavior. A 40% improvement in heat transfer coefficient is found versus typical dropwise condensation performance in the literature. Finally, candidate surfaces are identified for experimental validation of the predicted heat transfer behavior.

4.2 Introduction

Since its discovery in 1930[32], dropwise condensation has received significant research attention due to its superior heat transfer performance compared with filmwise condensation. In a recent review article, Cho et al.[53] compiled heat transfer curves from condensation studies performed over the last 90 years. The results indicate that dropwise condensation can, in some situations, enhance the heat transfer coefficient by an order-of-magnitude compared with the filmwise mode. However, despite numerous recent efforts to engineer highly-efficient dropwise condensation surfaces that further increase this advantage, there have been only modest gains in the condensation heat transfer performance[6,188–192]. These shortcomings have often manifested from a poor understanding of how the surface design influences wetting, and thus fundamental drop processes that ultimately govern the heat transfer coefficient during dropwise condensation (i.e. nucleation, growth, and departure). Many researchers continue to pursue superhydrophobic surfaces with low adhesion ($\theta_0 \geq 150°$ & $\Delta\theta \rightarrow 0°$) for enhancing condensation heat transfer[193–209]. However, analytical modeling presented in this Chapter suggests slightly non-wettable surfaces ($\theta_0 \rightarrow 90°$) with low hysteresis ($\Delta\theta \rightarrow 0°$) may provide more favorable drop behaviors for achieving dropwise condensation heat transfer improvements. This is supported by the recent trend of experimentalists investigating condensation on lubricant-infused surfaces (LIS) where high drop mobility is attainable on substrates with $\theta_0 \ll 150°$[172,210–215].

During dropwise condensation, a population of drops continuously evolves on a condensing surface via nucleation, growth, and departure processes[50]. The number and size of drops on the surface dictates the heat transfer per-

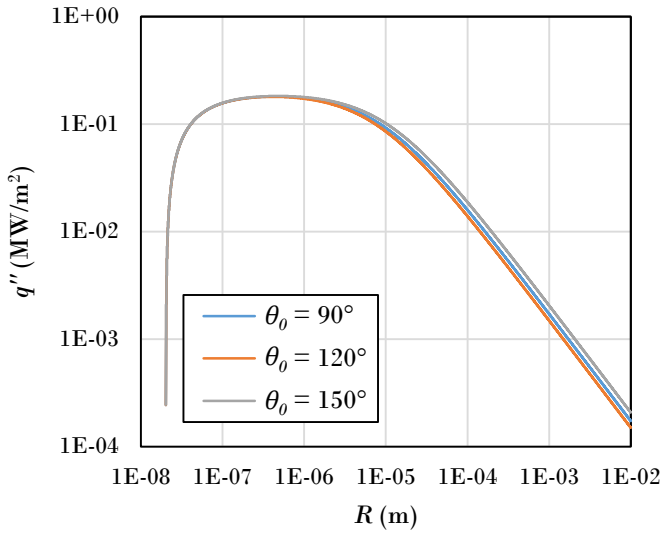

Figure 4.1: Single drop heat flux (q'') versus drop radius (R) for various static contact angles at $\Delta T = 1°C$, $\delta = 1\ \mu$m, $k_{coat} = 0.2$ W/m·K, $k_l = 0.68$ W/m·K, $h_{\dot{m}} = 15.7$ MW/m^2·K, and $r_{min} = 20$ nm.

formance since each drop acts as thermal resistance to heat transfer[216]. In 2011, Kim and Kim[34] developed the first single-drop heat transfer model for non-wettable surfaces (that is, when the condensate has a static contact angle $\theta_0 > 90°$). This model accounts for resistances due to liquid-vapor interfacial mass transfer, drop curvature, conduction through the drop, and conduction through a dropwise condensation promoter layer

$$q_d = \frac{\Delta T \pi R^2 (1 - \frac{r_{min}}{R})}{\frac{\delta}{k_{coat} \sin^2 \theta_0} + \frac{R\theta_0}{4k_l \sin \theta_0} + \frac{1}{2h_{\dot{m}}(1 - \cos \theta_0)}} \tag{4.1}$$

where ΔT is the degree of surface subcooling, R is the drop radius, r_{min} is the drop nucleation radius, δ is the promoter coating thickness, k_{coat} is the promoter coating thermal conductivity, k_l is the condensate thermal conductivity, and $h_{\dot{m}}$ is interfacial mass transfer coefficient. Figure 4.1 shows that small drops are predicted to have the highest heat fluxes (q''), which has also been confirmed by experiment[42,52]. Thus, to maximize the heat transfer coefficient, it is necessary

to have a sizable population of small drops on the condensing surface at any one time. This can be accomplished by frequent drop departure via sliding that clears (or sweeps) the condenser surface for nucleation[45]. In designing such a surface, it is required to have (i) fast drop nucleation, (ii) fast drop growth to the departure size, and (iii) small drop departure sizes. The present work analyzes gravity-driven dropwise condensation of steam on surfaces with uniform wettability (that is, surfaces with non-variable static contact angle and contact angle hysteresis) to determine how such behaviors can be realized. Then, an analytical heat transfer model is employed to predict possible enhancements in heat transfer performance via optimal surface design.

4.3 Drop Nucleation, Growth, and Departure

During dropwise condensation, drops nucleate exclusively at the condenser surface because heterogeneous nucleation has a significantly reduced energy barrier versus homogeneous nucleation. Via classical nucleation theory, the heterogeneous nucleation rate is derived as[217]

$$J = \nu_l \left(\frac{2\sigma_{lv} f(\theta_0)^3 N_A}{\pi M_w}\right)^{1/2} \left(\frac{P_v}{R_m T_v}\right)^{5/3} \left(\frac{N_A}{M_w}\right)^{2/3} \left(\frac{1-\cos\theta_0}{2}\right) \exp\left(\frac{-16\pi(\frac{\sigma_{lv} f(\theta_0)}{R_m T_v})^3 \nu_l^2 N_A}{3M_w[\ln(\frac{P_v}{P_{sat}(T_v)})]^2}\right) \quad (4.2)$$

where σ_{lv} is the liquid-vapor surface tension, $f(\theta_0) = \frac{1}{4}(2 - 3\cos\theta_0 + \cos^3\theta_0)$ is a shape factor, N_A is the Avogadro number, M_w is molecular weight, P_v is vapor pressure, T_v is vapor temperature, R_m is the mass-specific ideal gas constant, ν_l is liquid specific volume, and P_{sat} is saturated vapor pressure. Figure 4.2 plots the nucleation rate versus static contact angle for steam condensation at various surface temperatures. As static contact angle decreases, the nucleation

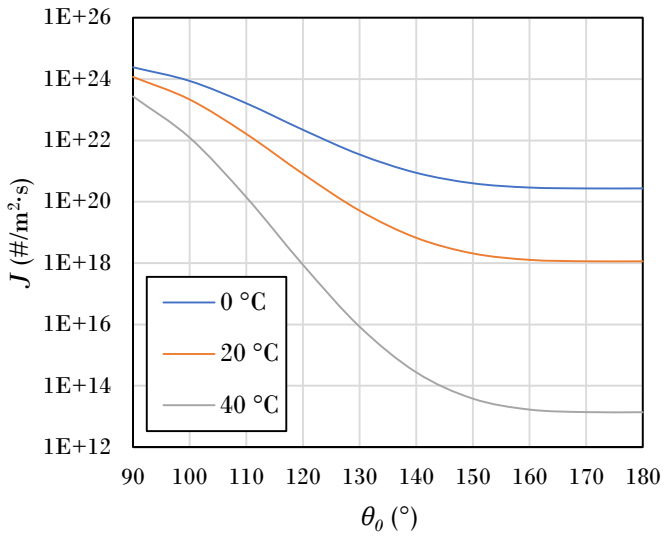

Figure 4.2: Drop nucleation rate (J) versus static contact angle (θ_0) for steam condensation (pressure = 1 bar) at various surface temperatures (0 °C, 20 °C, and 40 °C).

rate increases. This is because the critical nucleation radius is identical for all static contact angles at a particular subcooling, meaning smaller static contact angles have a reduced energy barrier since they have a smaller critical nucleation volume. It is also noted that the nucleation rate increases at decreased surface temperatures since the critical nucleation radius decreases with increased subcooling. Thus, at a given subcooling, fast drop nucleation during dropwise condensation is favored by reducing the static contact angle towards 90°.

Next, the growth rate of drops due to condensation is analyzed. Since the heat transfer rate through a drop equals the rate of enthalpy change for newly condensing vapor, Equation (4.1) can be set equal to $\dot{m}_l h_{fg}$ where $\dot{m}_l = \frac{dm_l}{dt}$ is the condensate mass flow rate and h_{fg} is latent heat of vaporization. Since $m_l = \rho_l V_l$, where ρ_l is the condensate density and $V_l = \frac{1}{3}\pi R^3(2 + \cos\theta_0)(1 - \cos\theta_0)^2$ is the condensate volume,

$$q_d = \pi R^2 \rho_l h_{fg} (2 + \cos\theta_0)(1 - \cos\theta_0)^2 \frac{dR}{dt} \tag{4.3}$$

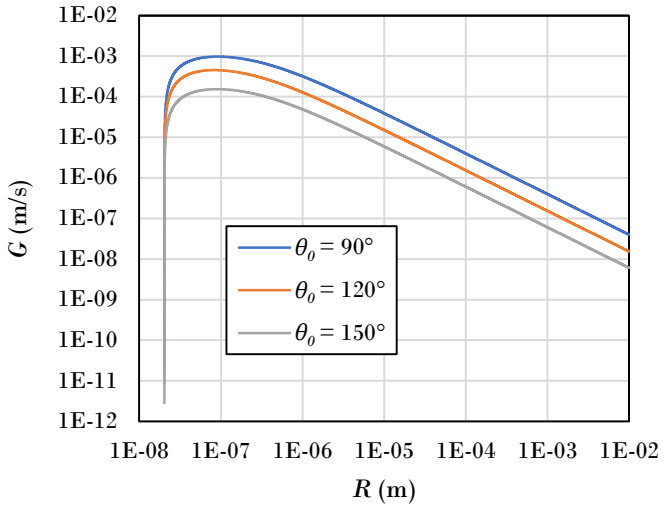

Figure 4.3: Single drop growth rate (G) versus drop radius (R) for various static contact angles at $\Delta T = 1°C$, $\delta = 20$ nm, $k_{coat} = 0.2$ W/m·K, $k_l = 0.68$ W/m·K, $\rho_l = 959$ kg/m^3, $h_{\dot{m}} = 15.7$ MW/m^2·K, $r_{min} = 20$ nm, and $h_{fg} = 2.26$ MJ/kg.

where $\frac{dR}{dt} \equiv G$ the drop growth rate. Solving for G yields

$$G = \frac{A_1 \left(1 - \frac{r_{min}}{R}\right)}{A_2 R + A_3} \tag{4.4}$$

with parameters A_1, A_2, and A_3 defined as

$$A_1 = \frac{\Delta T}{\rho_l \, h_{fg}}, \tag{4.5}$$

$$A_2 = \frac{\theta_0 \left(2 + \cos\theta_0\right) \left(1 - \cos\theta_0\right)^2}{4 \, k_l \, \sin\theta_0}, \tag{4.6}$$

$$A_3 = \frac{\left(2 + \cos\theta_0\right) \left(1 - \cos\theta_0\right)}{2 \, h_{\dot{m}}} + \frac{\delta \left(2 + \cos\theta_0\right) \left(1 - \cos\theta_0\right)^2}{k_{coat} \, \sin^2\theta_0}. \tag{4.7}$$

Figure 4.3 plots growth rate versus drop radius for steam condensation at various static contact angles. Drop growth rates decrease with both increased static contact angle and radius because drops of larger volume have higher resistance to heat transfer. Thus, at a given subcooling, fast drop growth via condensation is favored by reducing the static contact angle towards 90°.

Finally, the departure size of drops due to gravity is analyzed. A force balance at the drop contact line between surface tension and gravity is performed as $F_\sigma = F_g$ where

$$F_\sigma = 2\,\sigma_{lv}\,R\,\sin\theta_0\,(\cos\theta_r\,-\,\cos\theta_a) \tag{4.8}$$

and

$$F_g = \frac{\pi}{3}\,R^3\,(2\,+\,\cos\theta_0)\,(1\,-\,\cos\theta_0)^2\,\rho_l\,g\,\cos\Theta \tag{4.9}$$

with θ_r the receding contact angle, θ_a the advancing contact angle, and Θ the surface inclination from a vertical reference. Here, the surface is assumed to be vertically oriented so $\cos\Theta = 1$. The drop departure size $\hat{r}$ is then

$$\hat{r} = \left(\frac{6\,\sigma_{lv}\,\sin\theta_0\,(\cos\theta_r\,-\cos\theta_a)}{\pi\,\rho_l\,g\,(2\,+\,\cos\theta_0)\,(1\,-\,\cos\theta_0)^2}\right)^{1/2}. \tag{4.10}$$

Figure 4.4 plots water drop departure size versus contact angle hysteresis for various static contact angles. Here, it is assumed that $\theta_0 = \frac{1}{2}(\theta_a + \theta_r)$. As contact angle hysteresis decreases, the drop departure size also decreases due to reduced contact line pinning. Also, for the same contact angle hysteresis, higher

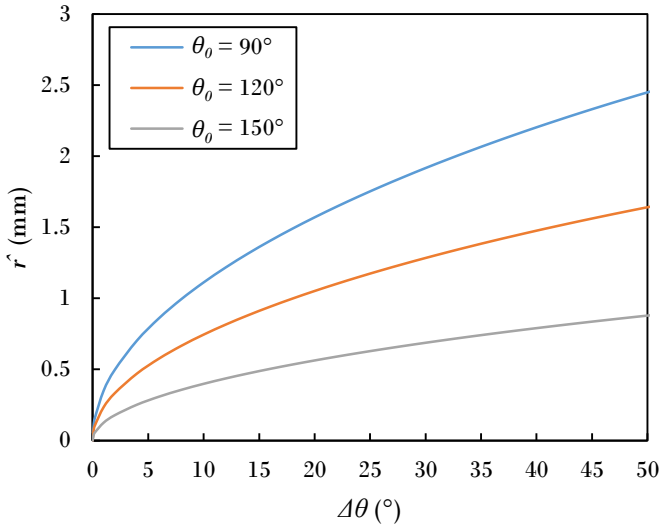

Figure 4.4: Drop departure size ($\hat{r}$) versus contact angle hysteresis ($\Delta\theta$) for various static contact angles with $\rho_l = 998$ kg/m^3, $g = 9.81$ m/s^2, and $\sigma_{lv} = 0.072$ J/m^2.

static contact angles reduce the drop departure size because the footprint of the drop contact with the surface is smaller. However, the departure size begins to converge independent of static contact angle as the hysteresis approaches zero. Thus, small drop departure sizes are favored by low-hysteresis surfaces. In summary, reducing the static contact angle towards 90°promotes fast nucleation and drop growth while reducing the contact angle hysteresis towards 0°allows for smaller drop departure sizes.

4.4 Dropwise Condensation Heat Transfer Modeling

The prior analysis suggests that favorable heat transfer performance can be achieved on a hydrophobic surface with low-hysteresis where the static contact angle trends towards 90° and the contact angle hysteresis trends towards 0°. Before testing such a surface experimentally, it is worth estimating if any improvement in heat transfer can be expected over legacy data. Mathematical prediction of the heat transfer coefficient during dropwise condensation can be accomplished by combining the single-drop heat transfer model with the drop size distribution

$$q'' = \int_{r_{min}}^{r_e} q_d \, n \, dr + \int_{r_e}^{\hat{r}} q_d \, N \, dr \tag{4.11}$$

where n is the drop size distribution for small drops that grow primarily by condensation, N is drop size distribution for large drops that grow primarily by coalescence, and r_e is the transition radius from condensation-dominated growth to coalescence-dominated growth. The drop size distribution for small drops is derived via a population balance as[27]

$$n = \frac{1}{3\,\pi\, r_e^3\, \hat{r}} \left(\frac{r_e}{\hat{r}}\right)^{-2/3} \frac{R\,(r_e - r_{min})}{R - r_{min}} \, \frac{A_2 R + A_3}{A_2 r_e + A_3} \, \exp(B_1 + B_2) \tag{4.12}$$

with

$$B_1 = \frac{A_2}{\tau A_1}\left(\frac{r_e^2 - R^2}{2} + r_{min}(r_e - R) - r_{min}^2 \ln\left(\frac{R - r_{min}}{r_e - r_{min}}\right)\right), \tag{4.13}$$

$$B_2 = \frac{A_3}{\tau A_1}\left(r_e - R - r_{min} \ln\left(\frac{R - r_{min}}{r_e - r_{min}}\right)\right), \tag{4.14}$$

$$\tau = \frac{3r_e^2 (A_2 r_e + A_3)^2}{A_1(11A_2 r_e^2 - 14A_2 r_e r_{min} + 8A_3 r_e - 11A_3 r_{min})}. \tag{4.15}$$

The drop size distribution for large drops has been established empirically by Rose and Glicksman[41]

$$N = \frac{1}{3\pi R^2 \hat{r}}\left(\frac{R}{\hat{r}}\right)^{-2/3}. \tag{4.16}$$

Table 4.1: Parameter values used to analytically model the steam dropwise condensation heat transfer behavior of Miljkovic et al. (2013). The rightmost column justifies the choice of each parameter value.

Parameter	Value	Justification
$h_{\dot{m}}$	15.7 MW/m^2·K	Experimental value for steam condensing at 1 atm.
θ_0	115°	Typical static contact angle for fluorosilanes; fits the hysteresis range.
δ	10 nm	Monolayer thickness reported in Miljkovic et al. (2013).
k_{coat}	0.1 W/m·K	Estimated based on similar fluorocarbon chains, e.g. polytetrafluoroethylene.
$\hat{r}$	1.7 mm	Estimated based on a force balance at the contact line using the reported θ_a and θ_r.
r_e	0.3 μm	Fit parameter; reasonable based on the condensation literature.

To verify the model, dropwise condensation heat transfer data for steam from Miljkovic et al.[6] is employed. The paper reports θ_a = 123°, θ_r = 81°, and $\delta \approx 10$ nm for (trichloro(1H,1H,2H,2H-perfluorooctyl)-silane deposited on a copper surface. Values of various model parameters with justification of their choice are reported in Table 4.1. All values related to condensate thermophysical properties are taken at the average temperature between the surface and condensing steam. Figure 4.5 shows an excellent match to the data when $r_e = 0.3\,\mu$m (red line). Based on the literature[218], this transition radius is highly reasonable. Next, the model was adapted to an idealized surface design by changing static contact angle to θ_0 = 90° and drop departure radius to $\hat{r}$ = 0.1 mm (based on contact angle hysteresis = 0.1°). Figure 4.5 predicts a 40% enhancement in heat transfer (green line) over the best legacy data, which motivates such a surface design as a route towards attaining highly-efficient dropwise condensation heat transfer.

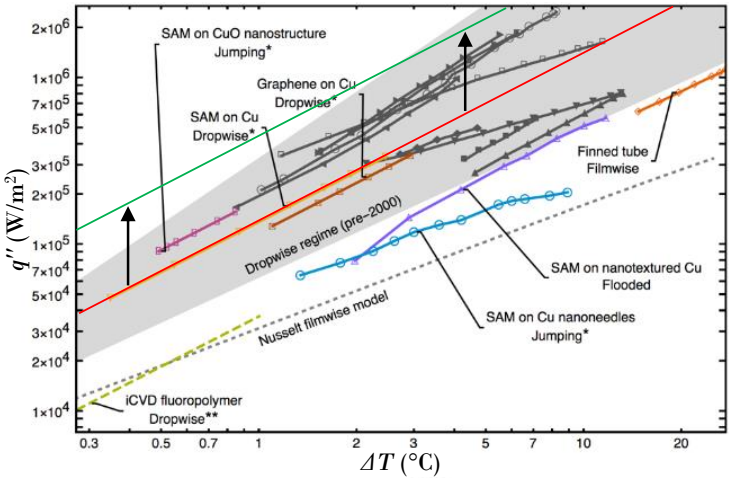

Figure 4.5: Analytical dropwise condensation heat transfer modeling results. Red solid line: model behavior versus experimental data reported in the literature. Green solid line: predicted enhancements in condensation heat transfer with θ_0 = 90° and $\Delta\theta$ = 0.1°. Figure adapted from Cho et al. (2016).

4.5 Conclusions and Future Work

Favorable surface wettability behavior for enhancing dropwise condensation heat transfer was motivated via theoretical analysis by studying the effect of static contact angle and contact angle hysteresis on drop nucleation, growth, and departure. It was shown that a lowly hysteretic hydrophobic surface could provide the fast drop nucleation, fast drop growth, and reduced drop departure sizes which are desired for maximizing the heat transfer coefficient. Further, possible heat transfer enhancements were modeled for such surfaces with a 40% advantage predicted over the best reports in the literature. Future work proposes to test such hydrophobic surfaces with low hysteresis, with several candidates identified:

- Trimethylsilyl-terminated linear poly(dimethylsiloxane) with reported θ_a = 105.6° and θ_r = 104.8°[219]

- Dichlorodimethylsilane with reported θ_a = 103.8° and θ_r = 102.7°[220]

- Lubricant-infused surfaces (LIS) where $(\theta_a - \theta_r) < 1°$[221]

Finally, it is also proposed to investigate promising robust materials for attaining sustained dropwise condensation that avoids degradation and flooding over long-time usage. Such materials include rare-earth oxides[222] and graphene[223]. The validation of these chemistries would benefit the areas of power generation, thermal management, and water desalination where filmwise condensation if often employed.

CHAPTER 5

CATASTROPHE THEORY MODEL OF THE TRANSITION FROM DROPWISE TO FILMWISE CONDENSATION

5.1 Abstract

The condensation heat transfer curve shows the relationship between heat flux and surface subcooling when saturated vapor is condensed onto a cooled substrate. As surface subcooling increases, a critical heat flux is eventually reached and the mode of condensation transitions from dropwise to filmwise. Experimental results show this transition can either be smooth or abrupt; however, to date, it remains unclear how different parameters (e.g. thermophysical properties of the solid-liquid-vapor system, magnitude of gravity, velocity of saturated vapor over the cooled substrate, etc.) influence which type of transition mechanism is observed. It has been previously hypothesized that insights can be deduced via catastrophe theory, where the transition between dropwise and filmwise condensation is regarded as a cusp-type catastrophe. However, an appropriate model has yet to be developed and confirmed against experimental data. In this paper, a cusp-type potential function is derived for the condensation process via classical nucleation theory. The potential function is then used to obtain the equilibrium curve and bifurcation set. Finally, model-predicted condensation heat transfer curves are compared to experimental data from the literature with reasonable qualitative agreement achieved. Future work should address the validity of the derived potential function by quantiative comparison to experiment.

5.2 Introduction

During dropwise condensation, drops continuously nucleate, grow, and coalesce on a cooled surface. To maintain dropwise condensation behavior, drop departure from the condensing surface is promoted by various means including gravity[190] or surface energy gradients[45], among others[6,46]. If drop departure does not occur at a sufficient rate, a transition to filmwise condensation is observed which is often undesirable because the overall heat transfer coefficient can be reduced by an order of magnitude[150]. The condensation heat transfer curve, Figure 5.1, captures the transition from dropwise to filmwise condensation by quantifying the heat flux versus surface subcooling relationship. The sharp decrease in heat flux with surface subcooling in Region C is indicative of the transition to the filmwise mode from the dropwise regime. Stylianou and Rose[224] have proposed two possible mechanisms for the transition to the filmwise mode, a coalescence-limited transition and a nucleation site saturation transition, along with transition criteria for each mechanism.

Hysteresis and catastrophe phenomenon can appear during the transition from dropwise to filmwise condensation, with Figure 5.1 showing the obvious existence of multi-fold solutions. Experimental results indicate that two types of transitions are possible[152]: smooth transitions and jump transitions, see Figure 5.2. At present, there remains the significant task of identifying how different system parameters influence which type of transition is observed, smooth or abrupt. Ma et al.[225,226] have proposed to elucidate this by means of the catastrophe theory, with transitions between condensation modes regarded as a cusp-type catastrophe. However, an appropriate model (including control paramters) has yet to be identified and confirmed against experiment. The cur-

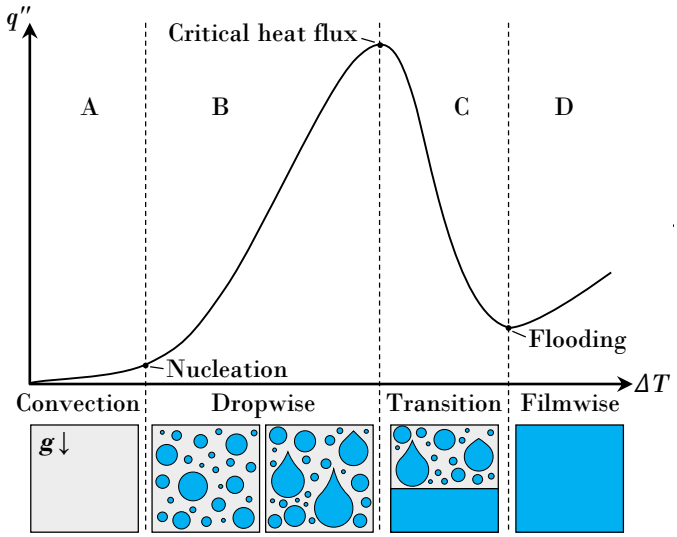

Figure 5.1: A typical heat transfer curve for a condensation phase change process plotting heat flux (q'') versus surface subcooling (ΔT). The various heat transfer regimes associated with Labels A, B, C, and D are pictorially depicted below the plot. Gravity vector g is also labeled.

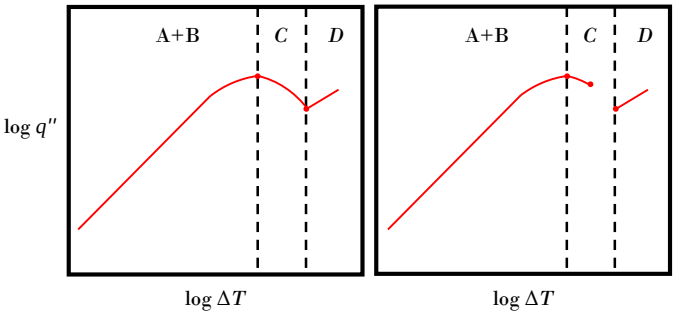

Figure 5.2: Condensation heat transfer curves showing (left) smooth and (right) abrupt transitions from the dropwise to filmwise mode. Labels A, B, C, and D correspond to the regimes identified in Figure 5.1. Sketch based on the experimental observation of Utaka et al. (1988).

rent study seeks to derive a cusp-type potential function for the condensation process, which can then be used to predict condensation heat transfer curves at various system parameters for eventual comparison to literature data.

5.3 Potential Function

Nucleation of drops is a fundamental process during dropwise condensation. Via classical nucleation theory, the critical radius of drop nucleation (r^*) can be derived as[34]

$$r^* = \frac{2T_{sat}\sigma_{lv}}{h_{fg}\rho_l\Delta T} \tag{5.1}$$

where T_{sat} is vapor saturation temperature, σ_{lv} is liquid-vapor surface tension, h_{fg} is latent heat of vaporization, ρ_l is liquid density, and ΔT is surface subcooling. Equivalently, r^* is also defined by classical nucleation theory as[227]

$$r^* = \frac{-2\sigma_{lv}}{\Delta G_v} \tag{5.2}$$

where ΔG_v is the volumetric free energy difference. By setting (5.1) and (5.2) equal, ΔT can be isolated as

$$\Delta T = \left(\frac{-T_{sat}}{h_{fg}\rho_l}\right)\Delta G_v. \tag{5.3}$$

Following a method analogous to the boiling process[228], (5.3) can be rewritten as

$$(\Delta T)^2 - \left(\frac{T_{sat}}{h_{fg}\rho_l}\right)^2 (\Delta G_v)^2 = 0 \tag{5.4}$$

which is recognized as being of similar form to the second derivative of the potential function for a cusp-type catastrophe. For a cusp-type catastrophe, the potential function is of the form $U = \frac{1}{4}x^4 - \frac{1}{2}px^2 - qx$ such that $\nabla^2 U = 3x^2 - p$.

By assuming[228] that one can replace ΔT with $\Delta T = \sqrt{3}\,(\Delta T - \Delta T_0)$, where the subscript 0 indicates a reference state, it can then be written that

$$\frac{\partial^2 U}{\partial \Delta T^2} = 3\,(\Delta T - \Delta T_0)^2 - \left(\frac{T_{sat}}{h_{fg}\rho_l}\right)^2 (\Delta G_v)^2 \tag{5.5}$$

where the bifurcation and catastrophe characteristics are independent of the topological transformation. As a first assumption, the dependence of h_{fg}, ρ_l, and ΔG_v on ΔT is neglected so (5.5) can be integrated to

$$\frac{\partial U}{\partial \Delta T} = (\Delta T - \Delta T_0)^3 - \left(\frac{T_{sat}}{h_{fg}\rho_l}\right)^2 (\Delta G_v)^2\,(\Delta T - \Delta T_0) - (q'' - q_0''). \tag{5.6}$$

The integration constant is assumed to be a function of q" since heat flux is a control parameter of surface subcooling. Finally, (5.6) is integrated to give the potential function for the condensation process as

$$U = \frac{1}{4}(\Delta T - \Delta T_0)^4 - \frac{1}{2}\left(\frac{T_{sat}}{h_{fg}\rho_l}\right)^2 (\Delta G_v)^2\,(\Delta T - \Delta T_0)^2 - (q'' - q_0'')\,(\Delta T - \Delta T_0). \tag{5.7}$$

with the integration constant neglected as it will not affect the catastrophe features. Utilizing

$$(\Delta G_v)^2 = \frac{16\,\pi\,\sigma_{lv}^3\,f(\theta_0)}{3\,\Delta G_{het}^*} \tag{5.8}$$

the potential function can be recast as

$$U = \frac{1}{4}(\Delta T - \Delta T_0)^4 - \frac{1}{2}\left(\frac{T_{sat}}{h_{fg}\rho_l}\right)^2 \frac{16\,\pi\,\sigma_{lv}^3\,f(\theta_0)}{3\,\Delta G_{het}^*}\,(\Delta T - \Delta T_0)^2 - (q'' - q_0'')\,(\Delta T - \Delta T_0) \tag{5.9}$$

where ΔG_{het}^* is the free energy of formation of a nucleating drop embryo, θ_0 is static contact angle, and $f(\theta_0) = \frac{1}{4}(2 - 3\cos\theta_0 + \cos^3\theta_0)$ is a drop shape factor. Again, (5.9) is a cusp-type catastrophe of the form $U = \frac{1}{4}x^4 - \frac{1}{2}px^2 - qx$ where x is $(\Delta T - \Delta T_0)$, p is a control variable accounting for various thermophysical properties of the system, and q is $(q'' - q_0'')$.

MATLAB and AUTO Continuation and Bifurfaction Software are used cooperatively to examine the derived potential function. First, the potential function

is plotted for fixed $p = 0$ and q varied from -2 to 2 to illustrate a smooth response in x (Figure 5.3). Conversely, Figure 5.4 illustrates a catastrophic response in x for fixed $p = 2$ and q varied from -2 to 2. These behaviors are confirmed in AUTO by solving $\nabla U = x^3 - px - q = 0$ for fixed p while q is varied. Figure 5.5 shows that for $p = 0$ there is no hysteresis in the x versus q plot, thus smooth behavior is expected. Comparatively, Figure 5.6 shows that for $p = 2$ there is obvious hysteresis in the x versus q plot so jump behavior is expected. Figure 5.7 plots the surface of equilibrium solutions, showing the expected pleat for a cusp-type catastrophe. The projecting curve in the q-p plane is also shown in Figure 5.8 to indicate the three-solution bifurcation regime. Here, both AUTO and MATLAB plots are shown so as to build confidence in the equilibrium curve presented in Figure 5.7.

In an attempt to explain the physical basis for the results presented, it can be argued that as p increases the liquid-vapor interface is becoming increasingly stabilized which leads to the appearance of a distinct transition regime. This follows with the thermophysical parameters contained in p; for example, increased surface tension increases p while also acting to physically restabilize the liquid-vapor interface to disturbances. Decreasing ρ_l reduces the ability of gravity to induce unstable waves, and that follows with the accompanying increase in p. Analogous arguments can also be made for $\frac{\Delta G^*_{het}}{f(\theta_0)}$ and h_{fg}. Other system parameters not included in the model can be analyzed as well. For example, velocity of saturated vapor over the cooled substrate would act to destabilize the interface when increased so it is predicted that this would act to reduce p.

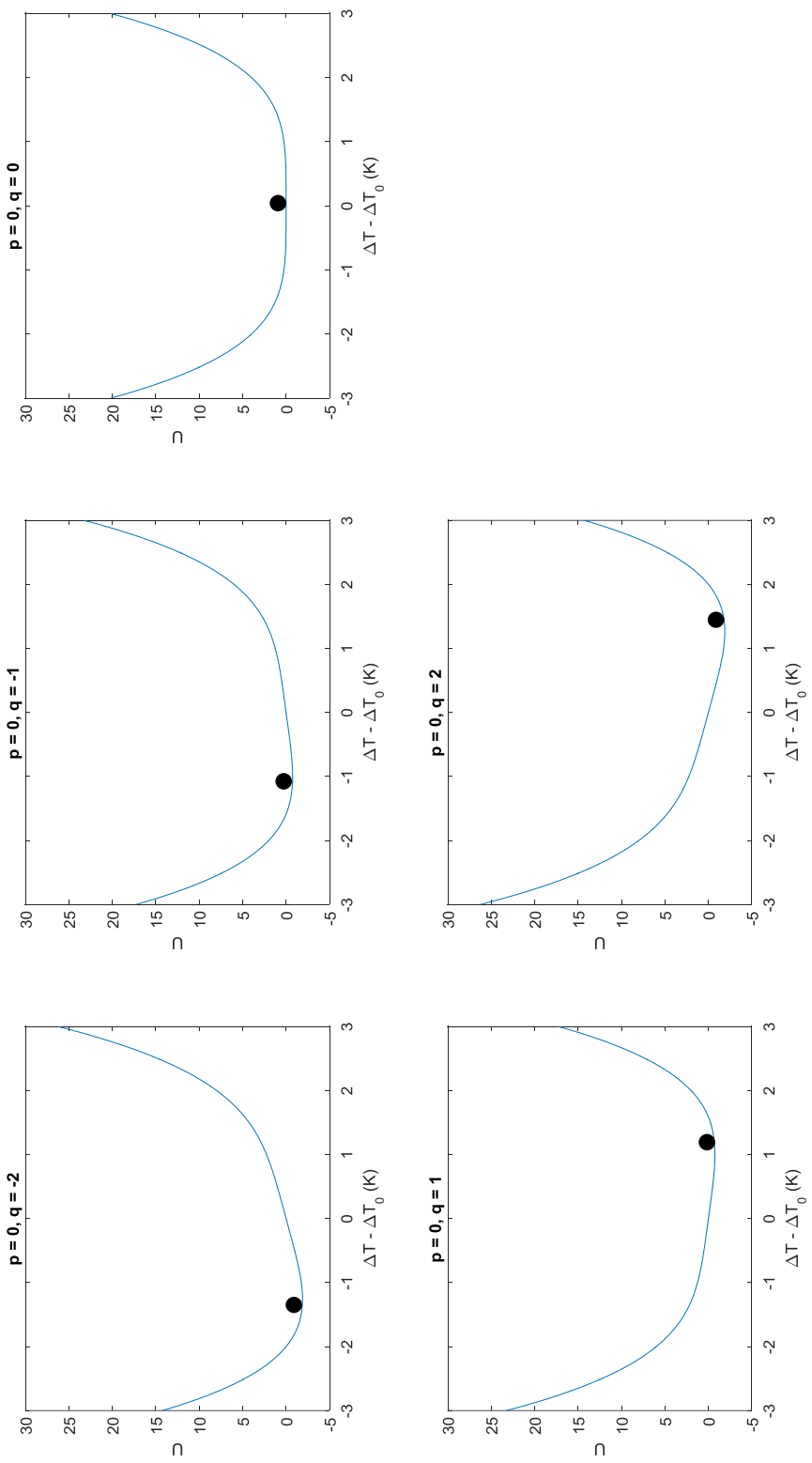

Figure 5.3: The evolving potential function U for $p = 0$ and q = [-2, 2] illustrating a smooth response in $x \equiv \Delta T - \Delta T_0$.

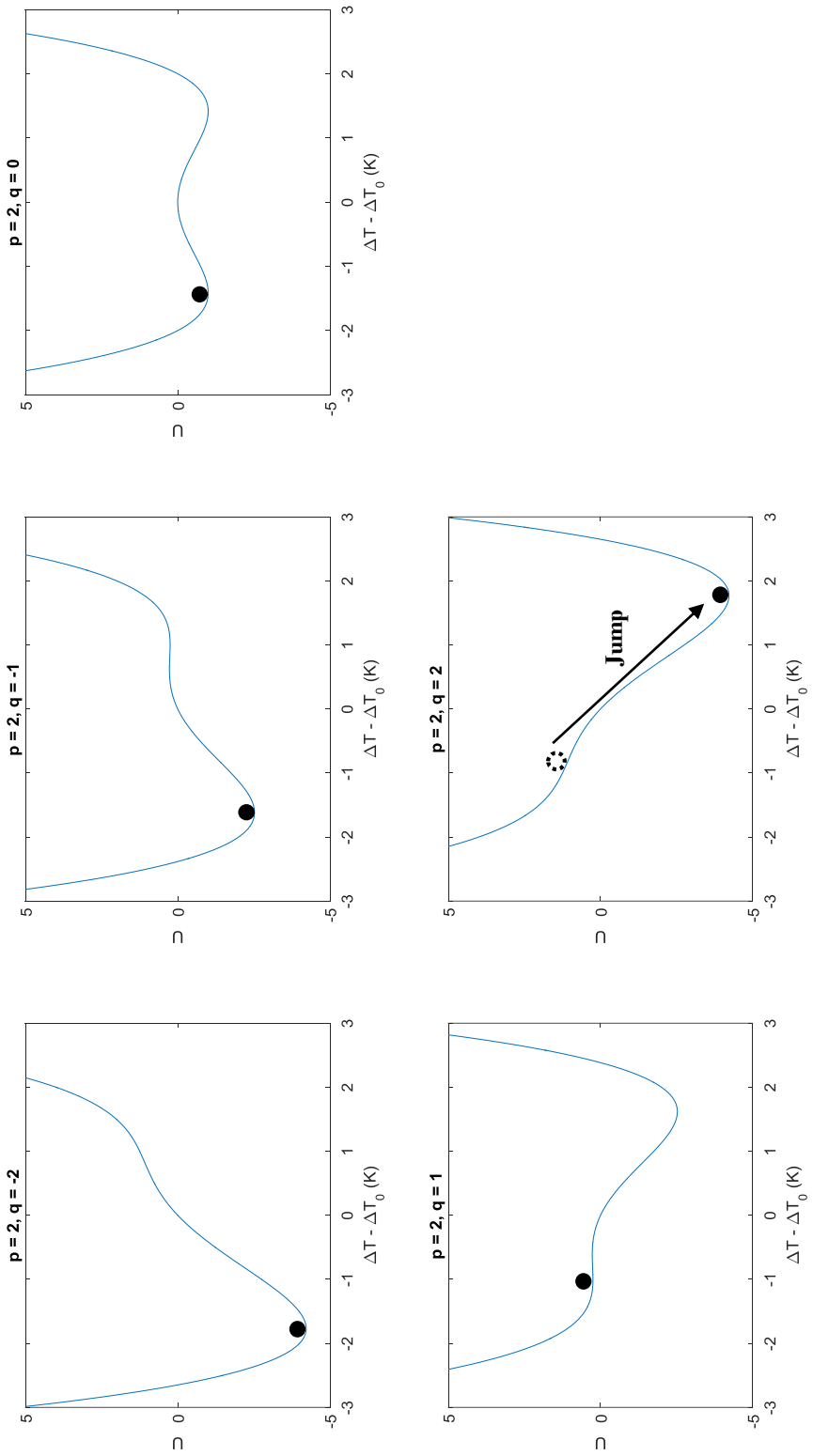

Figure 5.4: The evolving potential function U for p = 2 and q = [-2, 2] illustrating a catastrophic response in $x \equiv \Delta T - \Delta T_0$.

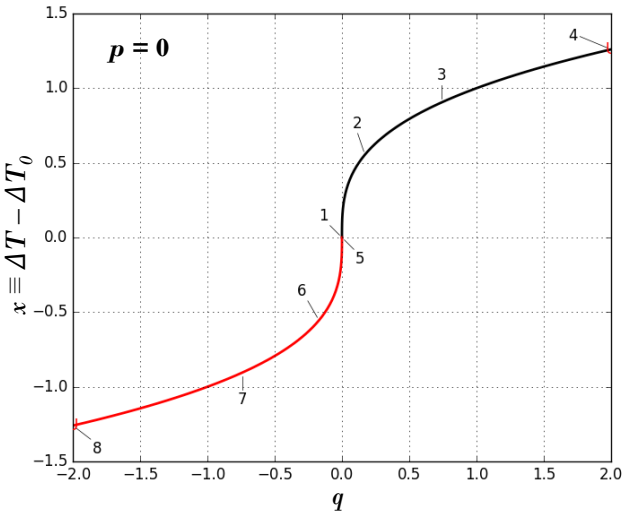

Figure 5.5: ($p = 0$ case) As the control parameter q is smoothly varied, there is a smooth response in x.

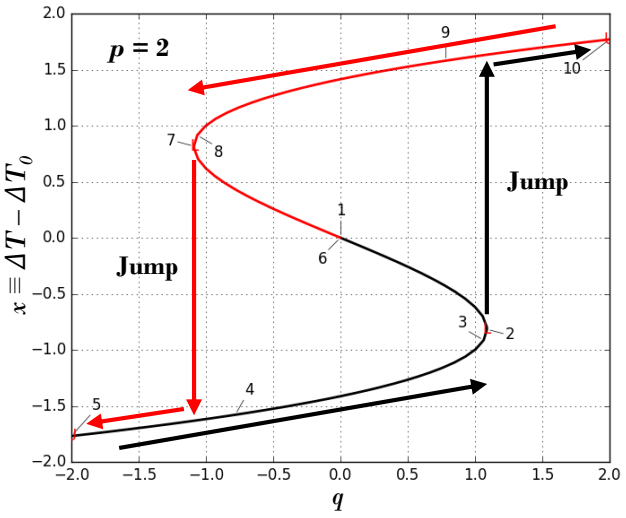

Figure 5.6: ($p = 2$ case) As the control parameter q is smoothly varied, there is a catastrophic response in x.

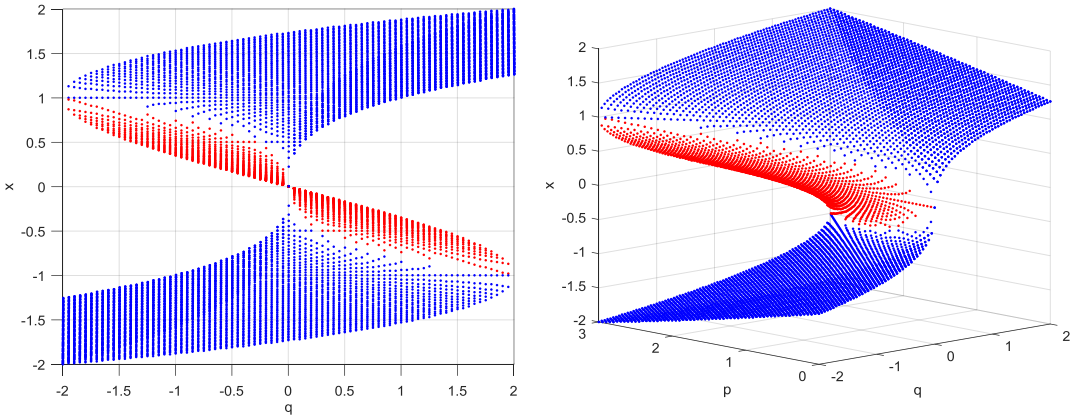

Figure 5.7: Two views of the equilibrium surface for the derived potential function showing the characteristic pleat for a cusp-type catastrophe. The red dots are unstable, while the blue dots are stable equilibria.

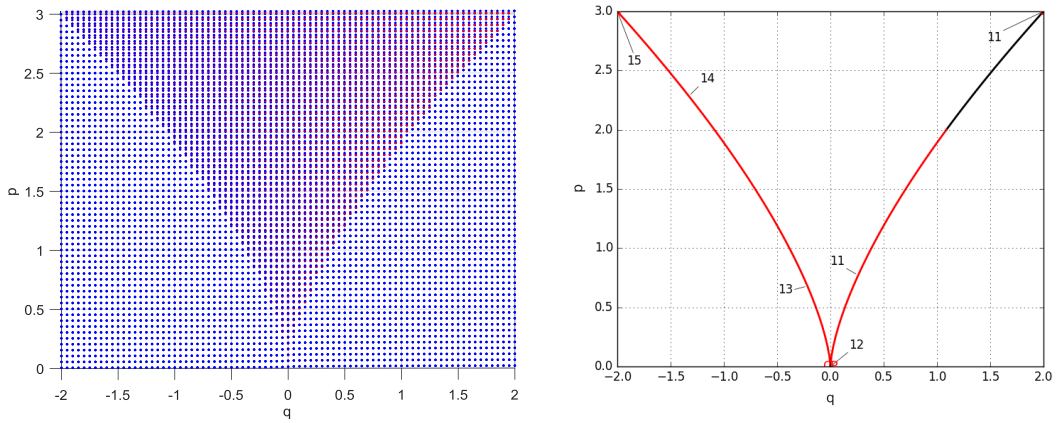

Figure 5.8: (left) MATLAB and (right) AUTO plots of the projecting curve in the q-p plane showing the three-solution bifurcation regime. The AUTO plot confirms the equilibrium curve presented in Figure 5.7.

5.4 Comparison to Experiments

Experimental condensation heat transfer curves are shown in Figure 5.9, representing both smooth and jump type transitions from dropwise to filmwise condensation. These can be compared qualitatively to heat transfer curves generated from the derived potential function with reasonable agreement (cf. Figure 5.10). For the smooth case, the model has difficulty capturing the decreasing

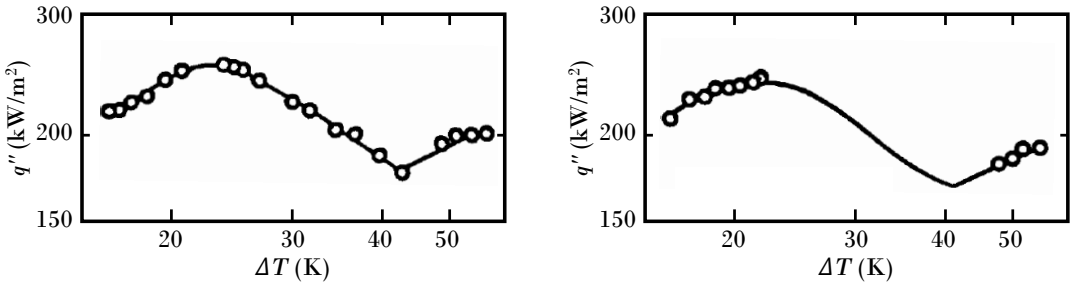

Figure 5.9: Experimental condensation heat transfer curves for a polytetrafluoroethylene coated surface showing (left) smooth and (right) abrupt transitions from the dropwise to filmwise modes. Condensing vapor is propylene glycol at saturation temperature $T_{sat} \approx 365K$. Data from Utaka et al. (1988).

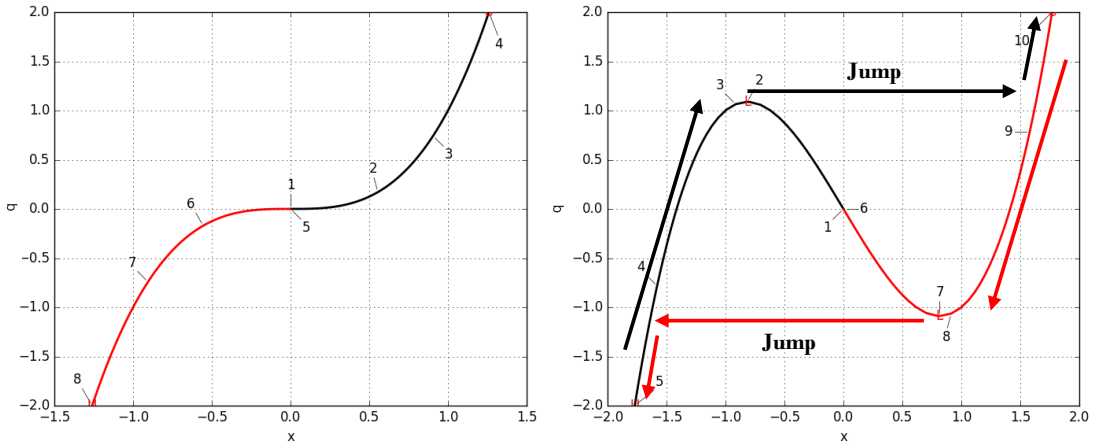

Figure 5.10: Potential function-predicted condensation heat transfer curves showing (left) smooth and (right) abrupt transitions from the dropwise to filmwise modes.

heat flux with increased surface subcooling in the stable transition regime. It is noted that quantitative comparisons are currently difficult to make due to a lack information about the energy barrier for heterogeneous nucleation. In future work, an estimation could be made using the nucleation rate $J = J_0 \exp(\frac{-\Delta G^*_{het}}{k_b T_{sat}})$ where J_0 is a pre-exponential factor and k_b is the Boltzmann constant.

5.5 Conclusions and Future Work

In this study, a cusp-type potential function for the condensation process was derived via the critical nucleation radius prescribed by classical nucleation theory. The potential function was then characterized in a variety of ways, including the equilibrium surface, bifurcation diagrams, hysteresis plots, and the potential function landscape. It was observed that as the control parameter p increased, a transition regime between the condensation modes became more apparent. An attempt was made to relate this observation to the increased stability of the liquid-vapor interface to disturbances as p increases. Finally, qualitative comparisons of the model-predicted condensation heat transfer curves to experiments were made with reasonable agreement. Future studies have been proposed that aim at a quantitative comparison by estimating a nucleation rate and thus an energy barrier for nucleation. In terms of additional future work, the derived potential function contains some relevant thermophysical properties of the condensation system in the control parameter p, but others are missing. Perhaps a potential function that contains other pertinent properties, such as those in the Condensation number $Co = \frac{h_c}{k_l}(\frac{\mu_l^2}{g\rho_l^2})^{1/3}$, can be developed. Conceivably, it may look like $U = \frac{1}{4}q''^4 - \frac{1}{2}(\Delta T)q''^2 - (Co)\,q''$.

CHAPTER 6

UNMASKING CONTACT LINE MOBILITY FOR INERTIAL-CAPILLARY SPREADING USING DROP VIBRATION AND COALESCENCE

(experiments associated with this National Science Foundation grant, Award #1637960, are expected to be performed on the International Space Station in 2020)

6.1 Abstract

On the International Space Station (ISS), liquids held by surface tension enjoy exceptionally large capillary lengths owing to the microgravity condition. That is, much larger liquid objects are shaped by surface tension on the ISS versus on Earth. Additionally, the larger capillary volumes respond on longer timescales. For this reason, inertial-capillary contact line motions that are small-scale and fast on Earth become larger-scale and slower on the ISS making them more accessible to observation there. Upcoming ISS experiments will enable a contact line mobility parameter M to be estimated for cases of inertial-capillary spreading. Mobility is considered a material-like phenomenological parameter that captures out-of-equilibrium dynamical responses of a moving contact line and, once determined for a solid-liquid-gas system, can be used in predictions of inertial-capillary spreading in other situations. The first experimental setup on the ISS will determine M by periodically forcing the contact line motion of a substrate attached drop via a mechanical shaker. The second experimental setup will induce a transient drop-drop coalescence event with consequent sweeping by contact lines. Using the calculated value of M to make predictions about the

coalescence dynamics, experiments will be compared with modeling to verify the utility of the mobility parameter.

6.2 Introduction

Inertial-capillary spreading occurs when a liquid moves across a solid surface displacing gas in such a way that liquid inertia and surface tension are the dominant competitors (Weber number, We = $O(1)$; Ohnesorge number, Oh $\ll 1$). Spreading typically means a partially wetting liquid with an advancing contact line, as just described. However, also considered here is the receding contact line case, where gas displaces liquid, as long as capillarity and inertia are the competitors. Over the past 50+ years, much work has been done on viscous spreading and the associated contact line singularity[11,229–233]. In contrast, relatively little work concerns inertial-capillary spreading[234–236] despite it being more common in applications. Two examples of industrial processes that exploit inertial-capillary spreading are illustrated in Figure 6.1: (left) immersion lithography[237] and (right) planar flow spin casting[238].

Challenges in predicting inertial-capillary spreading behavior arise from the deformable liquid-gas interface, the moving contact line, and the multi-scale nature of the contact line influence on bulk behavior[14]. Consequently, computational solutions to the full Navier-Stokes equations are difficult to obtain even at modest contact line speeds[239]. Furthermore, in experiment, fast events on sufficiently small scales near the contact line are problematic to observe. However, recent modeling progress points towards a breakthrough in predictions of inertial-capillary spreading by utilization of a contact line mobility parameter

M which can be measured in one context and applied in another[240].

The contact line mobility parameter was first introduced by Davis in the context of liquid rivulet stability[241]. It is sometimes mistakenly referred to as the Hocking condition, as Hocking has attributed credit to Davis[242]. The mobility parameter characterizes how contact line speed (U_{CL}) responds to the contact angle deviation from equilibrium ($\Delta\alpha$). According to theory, mobility parameter enters the dynamic contact line boundary condition as

$$M\Delta\alpha = U_{CL}. \tag{6.1}$$

Here, $M = 0$ corresponds to a pinned contact line whereas $M = \infty$ corresponds to no resistance to contact line motion or perfect slip. Even for the simplest contact line configurations, the challenge has been to solve the inviscid equations of motion for $M > 0$. Lyubimov et al.[243] solved for the contact line motions of the natural modes of vibration of a hemispherical drop for $M > 0$ and Fayzrakhmanova et al.[244] have extended this special case to forced oscillations. More recent progress has led to solutions for the natural frequencies and mode shapes of an arbitrary spherical cap configuration disturbed from equilibrium

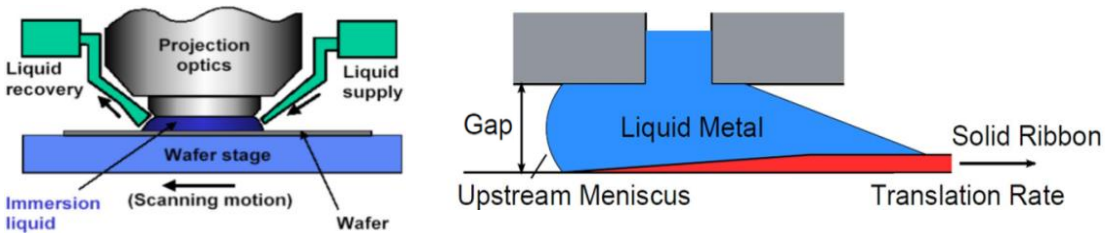

Figure 6.1: Small gap (< 1 mm) applications having inertial-capillary spreading: (left) immersion lithography with advancing and receding contact lines, wherein the wafer scans at speeds nearly 1 m/s underneath the immersion liquid. Figure from Clarke et al. (2006); (right) planar flow melt-spinning with an advancing contact line, wherein liquid metal solidifies against a substrate moving at speeds upwards of 10 m/s.

with general mobility M[245]. In order to estimate M from experimental observations, it is necessary to resolve disturbance quantities near the contact line (that is, contact line displacement and contact angle deviation from equilibrium). Recently, Xia and Steen have provided the first experimental measurements of M via drop vibration experiments[138]. For reference and comparison, other commonly employed dynamic contact angle models are described in Appendix D.

This work hypothesizes that M may be treated as a material parameter, say like viscosity, measured in one context and then applied in another. Here, it is proposed to measure M in the context of vibrated drops (Figure 6.2, left) and apply it to the configuration of drop coalescence (Figure 6.2, right). For vibrated drops, a mechanical shaker will be employed to periodically force a drop in a plane-normal fashion at a specific frequency and amplitude[137,246]. The dynamical response will be imaged and the mobility parameter will be estimated from measured disturbances around the contact line. For drop coalescence, the slow volumetric growth of a trigger drop will initiate a drop coalescence event with a second stationary drop to generate an inertial-capillary spreading transient. Predictions of the coalescence dynamics using the calculated value of M will then be compared to the experiments. The microgravity condition aboard the

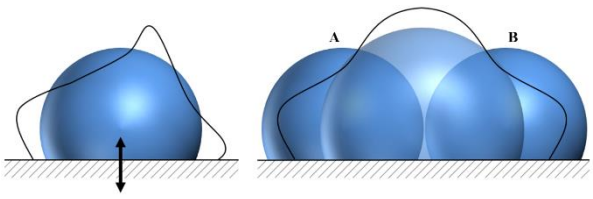

Figure 6.2: Contact line disturbances: (left) induced by support-normal oscillation; (right) induced by coalescence of drop A and drop B, evolving to a final shape (shadow).

International Space Station (ISS) is critical to imaging the contact line motions in both experiments by offering two benefits. First, the increased capillary length scale on the ISS allows for the use of larger drop sizes; this provides an effective spatial magnification and is especially important for hydrophobic drops where the contact line diameter is a fraction of the drop diameter. Second, the increased capillary timescale associated with larger drops makes corresponding liquid motions slower.

In summary, conducting the proposed shaken drop and coalescing drop experiments on the ISS instead of on Earth will allow for a critical study of inertial-capillary spreading dynamics via length and timescale enhancements. This unmasking will enable characterization of the contact line mobility parameter for various solid-liquid-gas systems (shaken drop), and then probe its utility in simulating inertial-capillary spreading generated by independent means (coalescing drops). That is, measurement will occur in one context and validated in another. The ISS microgravity will additionally open parameter ranges inaccessible on Earth for extended validation of theory predictions[137,240,247]. Finally, the ISS platform will deliver a valuable data set for anyone wishing to perform computational or model benchmarking for inertial-capillary spreading.

6.3 The ISS Advantage

On Earth, inertial-capillary contact line motions are fast and small scale. On the ISS, owing to the greater capillary length scale, inertial-capillary spreading takes place more slowly and at a larger scale. This well-known enhancement of the capillary length in low gravity is illustrated in Figure 6.3[248]. For water

Figure 6.3: Water blobs under low gravity conditions during a parabolic flight. These liquid shapes are unearthly in that they are held by surface tension at exceptionally large scales due to the increased capillary length. Images from Weislogel and Lichter (1998).

in air, the terrestrial capillary length scale is approximately 3 mm, whereas on the ISS it is over 3 m. That is, the capillary length scale is three orders of magnitude larger on the ISS than on Earth. In principal, meter scale water drops undergoing inertial-capillary spreading could be observed on the ISS. In practice, however, drop sizes are limited by the volume of the containing apparatus. The upcoming ISS experiments will be housed in the Microgravity Science Glovebox, with drops up to 3 cm in diameter accommodated. As such, ISS microgravity will yield an effective 10-times spatial magnification ($\frac{30\,mm}{3\,mm}$) over terrestrial experiments. More striking than the length scale enhancement is the benefit to timescales. Resonant inertial motions vibrate on an inertial-capillary timescale, $\tau = \sqrt{\frac{\rho_l R^3}{\sigma_{lg}}}$, where ρ_l is liquid density, R is drop radius, and σ_{lg} is liquid-gas surface tension. That is, since the ISS accommodates a 10x increase in length scale, inertial-capillary timescales will increase by $10^{3/2} \approx 30$. Stated differently, on the ISS, resonant frequencies of drops will scale down by nearly 30-fold. For the mechanical shaker experiments, this brings inaccessible drop vibration modes on Earth into reach on the ISS.

It is noted that common ground-based approaches used to achieve increased

capillary length scales (e.g. parabolic flight or drop tower experiments) do not provide long enough exposure to reduced gravity for the required contact line observations. The sustained microgravity environment provided by the ISS is necessary to track motions of dynamical drops. Also, there have been remarkable efforts to improve spatial resolution and frame rate for Earth-based observations of small and fast events. For example, the Brandaris 128 high-speed camera operates at 25 million frames per second but is limited in image storage[249]. We are unaware of any scientific breakthroughs owing to this camera. Another favored approach for examining small and fast inertial-capillary behavior has been to make use of event reproducibility[250], for example drop impact[251]. Here, frame rate is controlled by pulsed duration of the flash illumination source but the approach depends crucially on reproducibility of the phenomena studied.

6.4 Technical Impacts

Applications ranging from medicine to manufacturing to agriculture depend on understanding the inertial spreading of liquids, including that of drops. Drop impact and spreading are central to inkjet printing[252] and forensic blood splats[253] (Figure 6.4, left). 3D-additive manufacturing relies on and is limited by the action of surface tension in forming shapes from drops that eventually solidify[254]. Inertial spreading is fundamental to immersion lithography that yields state-of-the-art nanometer line widths in electronic chip fabrication[255] and to planar flow spin casting by which amorphous metallic alloys are formed for ultra-efficient energy conversion devices[256]. Condensation heat transfer devices depend on the continual exposure of fresh substrate to vapor where

nucleation and growth of condensate can occur[45]. In this application, coalescence sweeping of smaller drops is an effective means to refresh the substrate and enhance device performance (Figure 6.4, middle). Coating a solid sphere by immersion in a liquid bath provides another example[257] (Figure 6.4, right). In agriculture, the spray application of pesticides often depends on the inertial spreading of drops on a leafy substrate[258]. Finally, in the realm of space vehicles, inertial spreading of liquid fuel along vanes is important to fuel tank design[259]. In summary, many relevant processes and equipment operate in regimes with inertial spreading and depend on the nature of liquid movement across a solid. As such, characterization of the contact line mobility parameter is of benefit for understanding inertial-capillary spreading in these application areas and to enhance predictive capabilities.

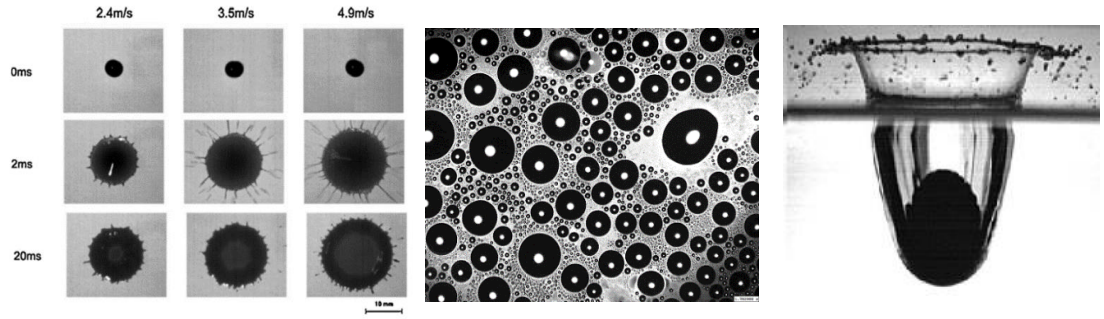

Figure 6.4: Additional applications with inertial-capillary contact line motion: (left) drop impact on a substrate yields different splat patterns depending on Weber number, relevant to crime scene forensics and ink-jet printing (scale bar = 1 cm). Image from Hulse-Smith and Illes (2007); (middle) dropwise condensation on a cold plate, relevant to phase change heat transfer (1 x 1 cm view); (right) a solid sphere (2.54 cm diameter) enters a liquid bath from air, relevant to immersion coating processes. Image from Aristoff et al. (2010).

6.5 ISS Experiments

As previously outlined, a substrate-attached drop will be vibrated via a mechanical shaker (SF-9324, PASCO Scientific) to induce cyclic contact line motions (Figure 6.5). The drop will primarily be driven at the [2,0] resonance mode for maximum contact line deflection, with two high-speed cameras (Prosilica GX1050C, Allied Vision & i-SPEED 220, iX Cameras) used to record the dynamical motions. M will then be extracted via post-processing analysis of the experimental observations, see technique described in Xia and Steen[138]. After determining M for a specific solid-liquid-gas system via the shaker experiments, it will be used to predict contact line transients during a drop-drop coalescence event to assess its utility. Triggered drop-drop coalescence experiments will also be performed on the ISS and recorded with two high-speed cameras. Coalescence will be induced by slowly growing a drop via a small diameter through-hole in the surface ($\phi \approx 0.5$ mm) until it touches a second pre-positioned drop (Figure 1.4). Post-processing of the high-speed images will then compare the experimental transients to the fluid dynamics modeling. All ex-

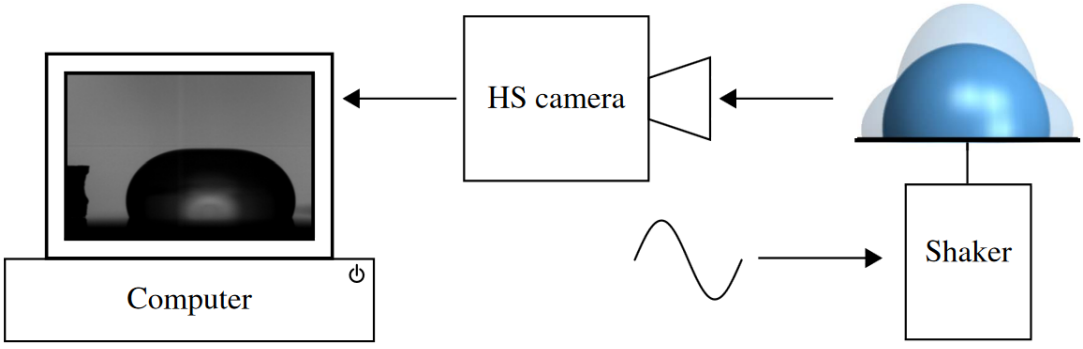

Figure 6.5: Vibration experiment setup: a sinusoidal input signal drives the mechanical shaker as a high-speed camera images dynamic drop shapes for analysis. Figure from Xia and Steen (2018).

Table 6.1: Experimental surfaces and water contact angle data.

No.	Surface	θ_0 (°)	θ_a (°)	θ_r (°)	$\Delta\theta$ (°)
1	Teflon	115	116	77	39
2	Sanded Teflon, version 1	130	155	100	55
3	Sanded Teflon, version 2	151	163	126	37
4	Sanded Teflon, version 3	155	162	153	9
5	Polydimethylsiloxane on silicon	105	109	98	11
6	(heptadecafluoro-1,1,2,2-tetrahydrodecyl) trichlorosilane on silicon	116	122	92	30
7	Polydimethylsiloxane on glass	105	108	93	15
8	(heptadecafluoro-1,1,2,2-tetrahydrodecyl) trichlorosilane on glass	117	124	83	41
9	3 cm diameter circular pinning site	Varies	180	0	180

periments will be performed inside the Microgravity Science Glovebox aboard the ISS, which is held at ambient conditions similar to those on Earth. Liquid drops will be water with sizes of diameter $D \approx 3$ cm (volumes $V \approx 10$ - 15 mL, depending on the static wettability of the surface) and deployed via a pipette (HandyStep 705110, BrandTech Scientific). Various solid surfaces with differing wettability will be employed during the experiments, see Table 6.1. Both vibration and coalescence experiments will be performed on surfaces 1 - 4, while only vibration experiments will be performed on surfaces 5 - 9. Sanded Teflon is prepared via a technique analogous to Nilsson et al.[25], (heptadecafluoro-1,1,2,2-tetrahydrodecyl)trichlorosilane via a technique analogous to Macner et al.[45], polydimethylsiloxane via a technique analogous to Krumpfer and Mc-

Carthy[219], and circular pinning site via a technique analagous to Chang et al.[137]. The value of θ_0 for the pinning site surface depends on the volume of liquid employed inside the hydrophilic (pinning) region. Surfaces 1 - 4 are approximately 10 cm x 10 cm (length x width), while surfaces 5 - 9 are approximately 8 cm x 8 cm.

6.6 Expected Outcomes and Future Outlook

As discussed in Xia and Steen[138], the procedure for measuring M developed by our research group constitutes the first direct experimental measurement of mobility parameter for rapid inertial-capillary contact line motions. This initial study has provided M for a limited set of solid-liquid-gas systems; the upcoming ISS work will act to expand this data set. The plan is then to use the mobility parameter measured in the shaker experiments to predict by computer simulation the coalescence-induced sweeping motions which can then be compared against the ISS coalescence observations. This testing will inform if M is a material parameter, as hypothesized. Our experiments will establish a scientific foundation for the engineering of processes involving fast-moving liquids. The ISS provides a unique environment whereby features of inertial-capillary contact line motions that are fast and small on Earth become slower and larger on the ISS, hence making them resolvable through imaging on temporal and spatial scales unmatched on Earth. By way of the principle of hydrodynamic similitude, observations from the ISS will inform our limited understanding of rapidly moving contact lines on Earth, vital to current fabrication of semiconductor chips, for example, and to the future discovery of new processes that depend on rapid wetting and spreading. The ISS experimental data and images

will also be uploaded to the National Aeronautics and Space Administration (NASA) Physical Science Informatics (PSI) data repository so other researchers can data mine and expand upon the work performed, which fulfills the President's Open Data Policy.

Utilizing the computational fluid dynamics model outlined in Section 1.3, sessile drop coalescence behavior on the ISS is simulated for surface nos. 1 - 4 in Table 6.1. In these computations, coalescence is performed between two identical drops with initial diameter D = 3 cm and wettability conditions as specified in Table 6.1; dynamic contact angles are implemented via Kistler's method[119]. The drops have no impact velocity at coalescence initiation and the gravity vector is enforced in the negative z-axis direction with magnitude 10^{-6} m/s^2. Depending on the wettability conditions employed, the simulations predict a range of dynamical behaviors, both in the bulk fluid and at the three-phase contact line. With increasing θ_0 and decreasing $\Delta\theta$, the merging process becomes more dynamical due to a larger interfacial energy release and reduced dissipation.

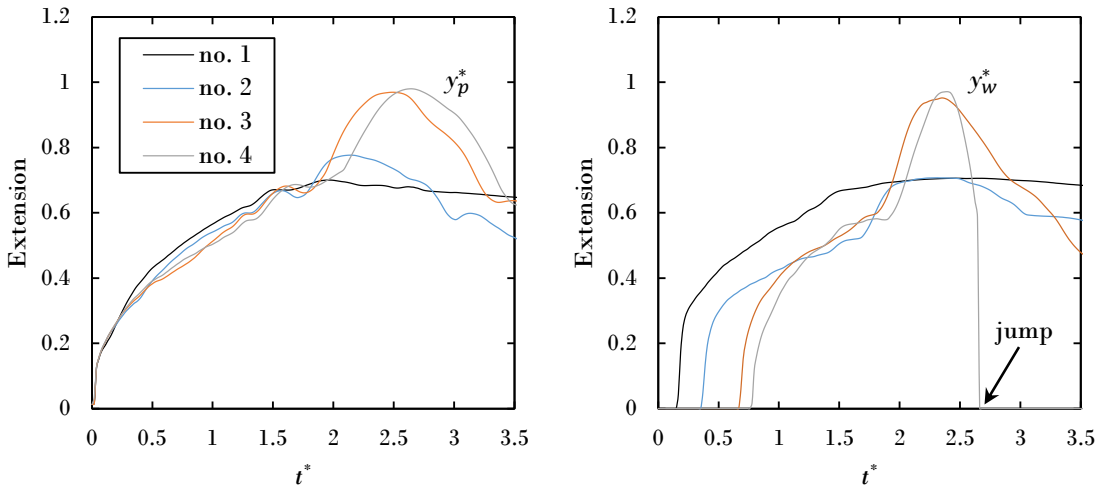

Figure 6.6: ISS sessile drop coalescence simulations: y_p^* & y_w^* versus t^* for four cases of sessile drop coalescence (Table 6.1, nos. 1 - 4).

This, of course, increases kinetic energy availability for liquid deformations[54]; see Figure 6.6 for the transients in the non-dimensional projected and wetted y-axis extensions (y_p^* & y_w^*, respectively) during coalescence. For surface no. 4, coalescence induced out-of-plane drop jumping is predicted as upward liquid momentum overcomes substrate adhesion on this superhydrophobic surface. If experimentally achievable on the ISS, this would be the first example of coalescence jumping at such a large scale (centimeters), as far as we are aware. At the centimeter scale, equivalent jumping behavior is not obtainable on Earth as the capillary length scale is exceeded and gravity counteracts the upward lift thus keeping the liquid secured to the surface. Eventually, these simulations will be compared to the ISS experiments, in addition to simulations that employ the to be determined mobility parameter M in a Davis-Hocking type dynamic contact line boundary condition.

As a first test of the utility of the mobility parameter, Earth-based shaker experiments were performed for water drops on a silicon wafer treated with trimethylsiloxy-terminated polydimethylsiloxane, or PDMS. As reported in Xia and Steen[138], the wettability metrics are $M = 0.24$ m/s $\cdot$ rad, $\theta_a = 102°$, and $\theta_r = 100°$. These parameters were implemented into a Davis-Hocking type dynamic contact angle model in OpenFOAM where, for advancing and receding contact lines,

$$\theta = \theta_a + U_{CL}/M \ for \ U_{CL} > 0, \tag{6.2}$$

$$\theta = \theta_r + U_{CL}/M \ for \ U_{CL} < 0, \tag{6.3}$$

respectively. Sessile drop coalescence between two identical drops was then simulated and compared to experiments. Pairwise coalescence between drops of diameter $D \approx 1.65$ mm was performed on a PDMS treated glass slide with comparable wettability to the silicon wafer. Transients in the non-dimensional

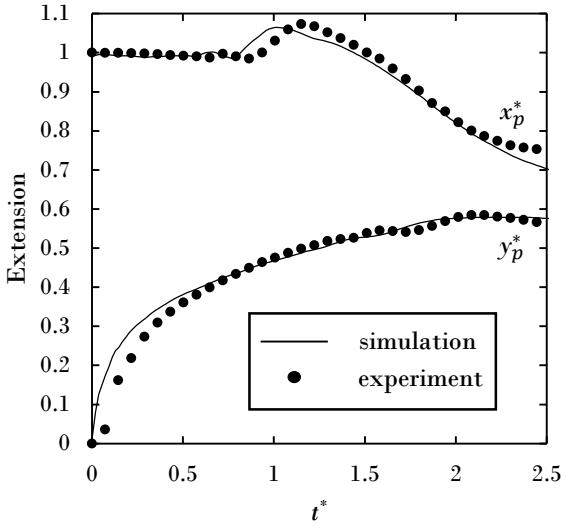

Figure 6.7: Coalescence transients, simulation versus experiment, for identical water drops merging on a PDMS treated surface. The simulation employs a Davis-Hocking type dynamic contact angle model which utilizes the measured mobility parameter M.

projected x- and y-axis extensions (x_p^* & y_p^*, respectively) are compared in Figure 6.7. Through dimensionless time $t^* = 2.5$, the simulation and experiment transients compare quite favorably. Correspondingly, metrics such as the non-dimensional maximum projected x- and y-axis extensions ($max(x_p^*)$ & $max(y_p^*)$, respectively) are also quite similar, in addition to the non-dimensional cumulative projected swept area ($\mathcal{P}^*$). This formative test provides initial confidence in utilizing M as a predictive tool for inertial-capillary spreading and further motivates the ISS experiments to be run in 2020.

Author Contributions: PHS conceived the initial idea of the research. YX and JML refined the research scope. PHS, SD, YX, and JML wrote the grant proposal. JML carried out the coalescence simulations and experiments.

PHS = Paul H. Steen, SD = Susan Daniel, YX = Yi Xia, JML = Jonathan M. Ludwicki

CHAPTER 7

IS MOBILITY A MATERIAL-LIKE PARAMETER?

7.1 Abstract

Numerous models exist to predict the dynamic contact angle θ response to velocity of the contact line U_{CL}. One such model introduced by Davis (1980) and popularized by Hocking (1987) employs a mobility parameter M as a proportionality constant to relate θ to U_{CL}. The so-called Davis-Hocking model is noteworthy for its simplicity, but has historically been limited in application as M must be indirectly determined by fitting model results to experiment for a particular solid-liquid-gas system. However, a recent experimental discovery by Xia & Steen (2018) has led to the first direct measurement technique for M in the inertial-capillary spreading regime. This opens up exciting possibilities for anticipating rapid wetting and dewetting behaviors, as M is believed to be a material-like parameter: measured in one context and used to predict in another. Here, we investigate the extent to which M is a material-like parameter via its application to sessile drop coalescence. This preliminary characterization provides initial insights as to the utility of the mobility parameter for predictive extension.

7.2 Introduction

The three-phase solid-liquid-gas contact line sets the boundary between wet and unwet support[230]. For a spreading liquid, the contact line advances across

the solid with liquid displacing gas. Conversely, for a receding contact line, retreating liquid is displaced by gas. In real systems, the contact line begins to advance or recede at an advancing contact angle θ_a or a receding contact angle θ_r, respectively[9]. Generally, comparable values $\theta_{a'}$ and $\theta_{r'}$ are obtained by instead slowing the contact line to a static configuration[11]. The difference in advancing and receding contact angles is often defined as contact angle hysteresis $\Delta\theta \equiv \theta_a - \theta_r$ and specifies the stick-slip behavior of the contact line. For non-moving contact lines with contact line velocity $U_{CL} = 0$, static contact angles obey $\theta_r < \theta_0 < \theta_a$. When $U_{CL} \neq 0$, the dynamic contact angle θ begins to deviate from θ_a (advancing case, $U_{CL} > 0$) or θ_r (receding case, $U_{CL} < 0$). Figure 7.1 provides an example of typical θ versus U_{CL} behavior[130].

Contact line motion, be it advancing or receding, has garnered significant research attention over the years due to its broad relevance in natural[63,260], industrial[238,255], and technological[261,262] areas. One outcome of this research has been the development of a number of models that predict θ response to motion of the contact line, as highlighted in several reviews[12–14]. Prominently used models include those based on classical hydrodynamic theory (e.g. Voinov[231]; Cox[263]), molecular kinetic theory (e.g. Blake & Haynes[264]), integrated hydro-

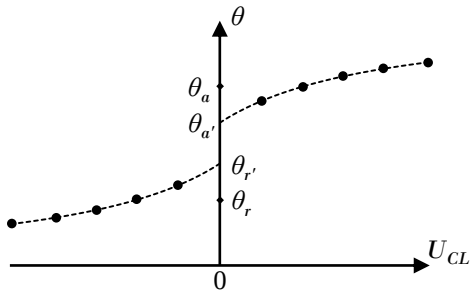

Figure 7.1: Traditional dynamic contact angle θ response to contact line velocity U_{CL}.

dynamic/molecular kinetic theory (e.g. Petrov & Petrov[265]), and empirical correlation (e.g. Kistler[119]). Typically θ is related to U_{CL}, along with other parameters which the dynamic contact angle is known to depend on (e.g. surface tension σ_{lg}, viscosity μ, density ρ)[266]. These models often find utility in computational fluid dynamics simulations where two immiscible fluids, say water-air, interact with a solid surface[123,125,126].

Of interest in this work is the so-called Davis-Hocking model, as motivated by a recent experimental development that could facilitate its implementation for predictive application in rapid wetting and dewetting regimes[138]. First Davis[241] and, later, Hocking[242] viewed contact line behavior as a single-valued function $g(U_{CL}) = \Delta\alpha$ where $\Delta\alpha \equiv \theta - \theta^*$ and $g(0) = 0$. Linearization about the rest state $\Delta\alpha = 0$ yields the Davis-Hocking condition,

$$M\Delta\alpha = U_{CL}, \tag{7.1}$$

where M is the mobility parameter. Equivalently, Equation (7.1) can be written as $\Delta\alpha = \Lambda U_{CL}$ where $\Lambda \equiv M^{-1}$ is the resistance to contact line motion. In previous literature works, M has also been referred to as a 'phenomenological parameter'[267], a 'wetting parameter'[243], and the 'Hocking coefficient'[244]. Equation (7.1) can be modified to accommodate systems with contact angle hysteresis, yielding the dynamic contact angle for advancing and receding motions, respectively, as

$$\theta = \theta_a + U_{CL}/M \quad for\ U_{CL} > 0, \tag{7.2a}$$

$$\theta = \theta_r + U_{CL}/M \quad for\ U_{CL} < 0. \tag{7.2b}$$

The Davis-Hocking approach allows for contact line behavior to be modeled without the complications associated with possible contact angle multiplicity at a particular contact line velocity. This, along with its simplicity, makes it attrac-

tive for application in modeling. However, determining the appropriate value of M for a particular solid-liquid-gas system is less straightforward. Previous methods are indirect in that M is varied in a simulation until a match to experiment is found, analogous to the contact line friction factor tuning in Carlson et al.[268]. That is, M is determined via its application as a fitting parameter. Until recently, no direct technique for measuring M was available.

In 2018, Xia & Steen[138,269] introduced a cyclically-dynamic contact angle goniometer for measuring M in the inertial-capillary regime. As the name implies, contact line motions in this regime are dictated by a competition between liquid inertia and surface tension, characteristic of rapid wetting and dewetting phenomena. We note that over the past 50+ years, much work has been done on viscous spreading and the associated contact line singularity[11,229–231,233,270,271]. However, in contrast, relatively little work concerns inertial-capillary spreading[234–236] despite it being more common in applications[237,272]. In a recent review article, Snoeijer & Andreotti[14] remark that, in terms of future issues related to understanding contact line behavior, 'new challenges for moving contact lines emerge from the influence of additional mechanisms, such as the inclusion of liquid inertia'.

To measure M, the experimental approach of Xia & Steen uses a mechanical shaker to drive the contact line of a sessile drop via a plane-normal vibration of the drop's support. As the contact line cyclically oscillates during the experiment (i.e. advancing and receding motions), measurements of $\Delta\alpha$, U_{CL}, and contact line displacement η are collected in time. A plot of $\eta\Delta\alpha$ versus ηU_{CL} reveals a regime where $\Delta\alpha$ is proportional to U_{CL}. This regime corresponds to inertial-capillary contact line motions with the slope yielding $\Lambda \equiv M^{-1}$. In-

deed, Fernández-Toledano et al. independently found that the uncompensated Young-Laplace force is linear in contact line velocity via molecular dynamics simulations[273]. It is further conjectured by Xia & Steen that, for a particular solid-liquid-gas system, M is a material-like parameter that can be first measured and then used to predict contact line behaviors in other contexts, for example during drop-solid impacts or drop sliding. However, the utility of M has yet to be confirmed. As an analogy, one can think of viscosity which is measured with a rheometer and then used to predict, say, a pressure drop in laminar pipe flow.

In this paper, we evaluate M and its utility. First, using the cyclically-dynamic contact angle goniometer, M is measured for four separate solid-water-air systems. To assess the predictive capabilities of the mobility parameter, sessile water drop coalescence is chosen due to the important role of both advancing and receding inertial-capillary contact line motions during the merging process[54,61]. Coalescence provides a challenging test of the mobility parameter for several reasons: (i) the occurrence of simultaneous advancing and receding motions, along with transitions between the two; (ii) the presence of contact line motions that are not strictly inertial-capillary; (iii) the significant degree of contact line motion and range of dynamic contact angle excursion during drop merging, c.f. Table 7.1 and Figure 7.3. For the pairwise coalescence of identical sessile drops, experiments are compared to numerical simulations that employ the Davis-Hocking model with the experimentally determined M values. We also contrast the performance of the Davis-Hocking model with the Kistler dynamic contact angle model[119], see Chapter 1 or Appendix D for a detailed description and definition. Ultimately, we comment on the validity of M as a material-like parameter.

Table 7.1: Coalescence as a test of the mobility parameter: comparison to alternative drop-surface experiments with inertial-capillary contact line motions.

Experiment	Simultaneous advancing and receding motions	Transitions between advancing and receding motions	Significant range of contact line motion and θ excursion	Presence of non inertial-capillary motions
Coalescence	✓	✓	✓	✓
Touching	✗	✗	✗	✗
Impact	✗	✓	✓	✓
Sliding	✓	✗	✓	✗
Vibration	✗	✓	✓	✓

7.3 Experimental Method and Numerical Model

Binary sessile water drop coalescence was performed on four separate surfaces, as summarized in Table 7.2 along with the corresponding wettability metrics. Note that the reported M values are measured via the method of Xia & Steen[138]. This assessment of the mobility parameter investigates two hydrophobic surfaces ($\theta_0 \approx 110°$) and two superhydrophobic surfaces ($\theta_0 \approx 150°$). Further, in each wetting regime, one surface has low contact angle hysteresis ($\Delta\theta \approx 5°$) and the other high ($\Delta\theta \approx 50°$). Trimethylsilyl-terminated linear poly(dimethylsiloxane), or PDMS (DMS-T22, Gelest Inc.), was deposited on soda-lime glass (16004-422, VWR International) according to the technique of Krumpfer & McCarthy[219], while various Teflon samples (PTFENAT0, Ridout Plastics) were sanded using silicon carbide sandpaper of different grits (Starcke Abrasives). For the drop merging experiments, coalescence was induced via one of three methods. For PDMS on glass, coalescence was generated via the controlled blowing of one drop into a stationary second drop by depressing the plunger of an empty plastic syringe, analogous to the technique of Nils-

Table 7.2: Experimental surfaces and wettability by water: initial θ_0, advancing θ_a, and receding θ_r contact angles, contact angle hysteresis $\Delta\theta$, and mobility M.

Surface	θ_0 (°)	θ_a (°)	θ_r (°)	$\Delta\theta$ (°)	M (m/rad·s)	M (Ca/rad)
PDMS on glass	109	109	106	3	0.24	0.003
Teflon (unsanded)	110	120	75	45	0.15	0.002
Sanded Teflon, 240 grit	151	152	148	4	0.31	0.004
Sanded Teflon, 120 grit	151	159	102	57	0.32	0.004

son & Rothstein[61]. For unsanded Teflon and Teflon 120, coalescence was produced via surface through-hole growth of one drop until it touched a second pre-positioned drop, see Ludwicki & Steen[54]. Finally, for Teflon 240, a trigger drop was pushed laterally into a second drop via a superhydrophobic wire, comparable to the method of Wang et al.[96]. In all cases, care was taken to impose a minimal impact velocity at coalescence initiation. For each coalescence experiment performed, the drops were of approximately equal diameter D at the time of coalescence (within 10% of each other) with sizes in the range of 1.5 mm $< D <$ 2.1 mm. Top and side view video cameras (Redlake MotionPro HS-3 and Redlake MotionXtra HG-XL, respectively) simultaneously recorded the coalescence dynamics at a frame rate of at least 1,000 frames per second.

OpenFOAM computational fluid dynamics software[121] is employed to simulate the pairwise coalescence of identical sessile drops. The computational method is fully described in a previous work[54], however a brief overview is provided here for completeness. The interFoam volume of fluid (VOF) solver, applicable to incompressible, laminar, and two-phase fluid flow, is utilized. The solver is modified from its original state to remove artificial anti-diffusive surface fluxes; this has been previously shown to improve transient behaviors in

Table 7.3: Simulation fluid properties: water (subscript l) and air (subscript g).

ρ_l (kg/m^3)	ρ_g (kg/m^3)	μ_l (mPa · s)	μ_g (mPa · s)	σ_{lg} (J/m^2)
998.0	1.204	0.998	0.0181	0.072

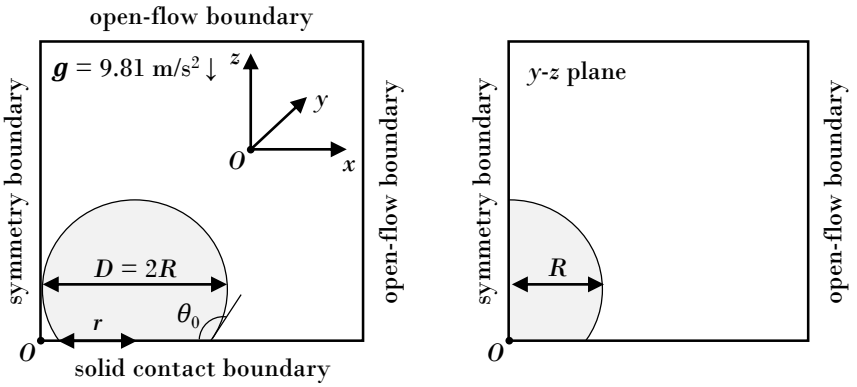

Figure 7.2: 3D computational domain for simulating binary sessile drop coalescence, with two symmetry planes as indicated.

capillary-dominated flows[54,102]. Material advection, momentum, and continuity equations are solved subject to a particular dynamic contact angle model (Davis-Hocking or Kistler). Binary sessile drop coalescence is simulated via a 2.6 mm x 2.6 mm x 2.6 mm computational domain comprised of cubic cells with edge length $\epsilon = 20\ \mu$m (Figure 7.2). Drops are initialized with diameters D and static contact angles θ_0 that correspond to the experimental conditions. At the no-slip solid contact boundary, a dynamic contact angle model is imposed with the experimentally measured values of θ_a, θ_r, and, if necessary, M. The open-flow boundaries are initialized as fixed pressure and zero velocity gradient. Fluid properties are for a water-air system at room temperature, see Table 7.3. Finally, the gravity vector $\boldsymbol{g}$ is enforced in the negative z-axis direction with magnitude 9.81 m/s^2 to match the experimental conditions. Relevant non-dimensional numbers for the simulations are presented in Table 7.4. As

Table 7.4: Non-dimensional characterization: Reynolds ($Re = \rho_l U_{CL} D/\mu_l$), Capillary ($Ca = \mu_l U_{CL}/\sigma_{lg}$), and Ohnesorge ($Oh = \mu_l/\sqrt{\rho_l \sigma_{lg} D}$) numbers for the simulations of binary sessile drop coalescence. Note that, here, U_{CL} is the maximum magnitude of contact line velocity in the x-axis for $y = 0$ and $z = 0$.

	Davis-Hocking			Kistler		
Surface	*Re*	*Ca*	*Oh*	*Re*	*Ca*	*Oh*
PDMS on glass	493	0.004	0.003	1491	0.012	0.003
Teflon (unsanded)	264	0.002	0.003	972	0.009	0.003
Sanded Teflon, 240 grit	851	0.006	0.003	1475	0.010	0.003
Sanded Teflon, 120 grit	615	0.004	0.003	1229	0.009	0.003

consistent with inertial-capillary spreading, both the Davis-Hocking and Kistler models produce $Re \gg 1$, $Ca \ll 1$, and $Oh \ll 1$ in all cases.

To compare simulation against experiment, several metrics are employed. First, time progressions of the projected extensions in the x-and y-axes (x_p & y_p, respectively) are tracked, Figure 7.3. In later discussions, projected extensions are normalized by $2R$ while time t is non-dimensionalized by the inertial-capillary timescale $\tau \equiv (\rho_l R^3/\sigma_{lg})^{1/2}$. Here, $R \equiv {}^1/_2\, D$ is the initial radius of a drop. Henceforth, all normalized and non-dimensional parameters are indicated by an asterisk superscript (*). A final cumulative projected swept area $\mathcal{P}_\infty$ is also outlined as drops coalesce and progress to a rest state, Figure 7.3. It is further normalized by the initial projected area of the coalescing drops, $\mathcal{P}_0 \equiv 2\pi R^2$, yielding $\mathcal{P}^* = \mathcal{P}_\infty/\mathcal{P}_0$. These metrics, together with the predicted coalescence dynamics, inform the efficacy of the contact line models in anticipating experimental behaviors.

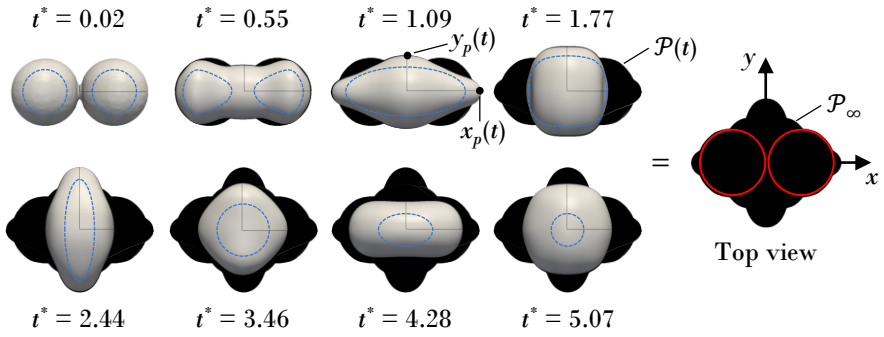

Figure 7.3: Coalescence extensions and swept areas: evolution of the x-axis and y-axis projected extensions ($x_p(t)$ & $y_p(t)$, respectively) during sessile drop coalescence. The contact line position (dashed blue line) is superimposed on the top view coalescence dynamics. Instantaneous cumulative projected swept areas $\mathcal{P}(t)$ are indicated by the black silhouettes, with the final cumulative projected swept area $\mathcal{P}_\infty$ at the right. The circles on $\mathcal{P}_\infty$ (red dashed) represent the initial projected drop areas.

7.4 Results and Discussion

7.4.1 Limits of the Davis-Hocking Model

For the Davis-Hocking model, Equations (7.2a) and (7.2b) can yield non-physical dynamic contact angles as determined by the combination of U_{CL}, M, and θ_a (advancing case) or θ_r (receding case). That is, at a high enough contact line velocity, it is possible for the model to produce $\theta > 180°$ for an advancing contact line or $\theta < 0°$ for a receding contact line. For the surfaces utilized in this work, Table 7.5 provides the range of U_{CL} values that maintain a physical dynamic contact angle where $0° \leq \theta \leq 180°$. In the results presented next, we assess Davis-Hocking model performance when the dynamic contact angle is constrained within $0° \leq \theta \leq 180°$ as, otherwise, non-realistic dynamics could evolve during coalescence. For constraining the dynamic contact angle, if the

Table 7.5: Davis-Hocking model limits: range of U_{CL} values that produce a valid dynamic contact angle where $0° \leq \theta \leq 180°$ for the parameter values presented in Table 7.2.

Surface	U_{CL} Range
PDMS on glass	-0.45 m/s < U_{CL} < 0.30 m/s
Teflon (unsanded)	-0.19 m/s < U_{CL} < 0.15 m/s
Sanded Teflon, 240 grit	-0.79 m/s < U_{CL} < 0.15 m/s
Sanded Teflon, 120 grit	-0.56 m/s < U_{CL} < 0.12 m/s

Davis-Hocking model calculates $\theta > 180°$ for $U_{CL} > 0$, then the dynamic contact angle is arbitrarily set to $\theta = 175°$, Equation (7.3a). Correspondingly, when the model calculates $\theta < 0°$ for $U_{CL} < 0$, the dynamic contact angle is arbitrarily set to $\theta = 5°$, Equation (7.3b):

$$\text{For } U_{CL} > 0: \quad \theta = \theta_a + U_{CL}/M \quad \text{if} \quad \theta \leq 180°, \quad \text{otherwise} \quad \theta = 175° \tag{7.3a}$$

$$\text{For } U_{CL} < 0: \quad \theta = \theta_r + U_{CL}/M \quad \text{if} \quad \theta \geq 0°, \quad \text{otherwise} \quad \theta = 5° \tag{7.3b}$$

This allows for a preliminarily assessment of the Davis-Hocking model performance. Figure 7.4 depicts θ versus $Ca \equiv \mu_l U_{CL}/\sigma_{lg}$ response for the family of contact angle models examined in this work. It is noted that, here, the Kistler model behaves closely to perfect slip for the range of Ca values observed during coalescence. A perfect slip or 'quasi-dynamic' model has $\theta = \theta_a$ for advancing contact lines and $\theta = \theta_r$ for receding contact lines, see Appendix D.

7.4.2 Experiment versus Simulation

As a first comparison of the experiments to the simulations, Figure 7.5 contrasts the evolution of the side view (x-z plane) coalescence dynamics on the four

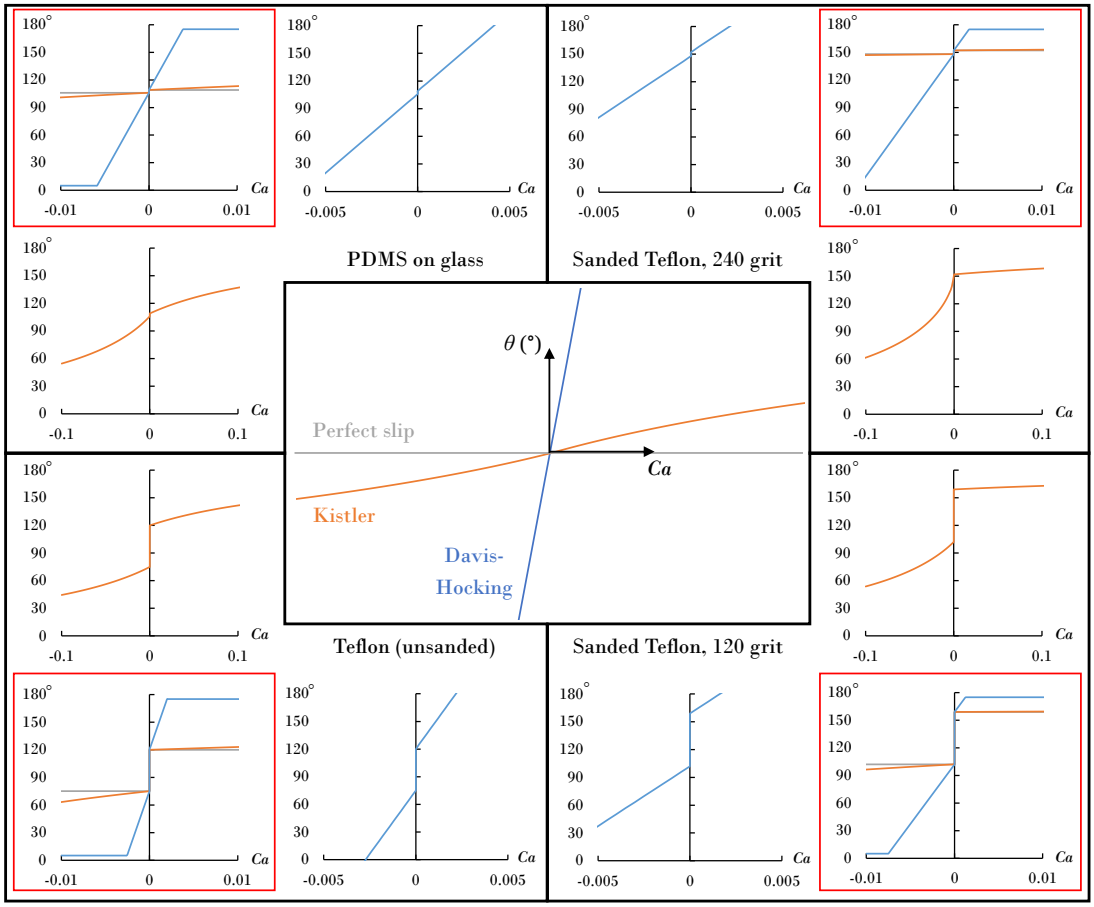

Figure 7.4: Family of contact angle models: (core) sketch of θ response to Ca for the Davis-Hocking, Kistler, and perfect slip models, no contact angle hysteresis case. (perimeter) model response, incorporating contact angle hysteresis, for the four surfaces investigated in this study. The corners, red squared, indicate model behavior for the Ca range probed by the simulations.

surfaces. It is noted that, here, we focus on time points $t^* \geq 1$ since, for the side view, this is when the contact line begins to move. Specifically, during binary sessile drop coalescence, $t^* \approx 1$ corresponds to the time it takes for the capillary wave to traverse along the top of the liquid to one of the drop ends. In terms of the dynamics, for the lower contact angle hysteresis surfaces (PDMS and Teflon 240), the Kistler model produces an overly mobile contact line and the experimental results are poorly captured. Conversely, the Davis-Hocking model more

accurately matches the apparent contact angle and contact line position of the experiments, along with the bulk dynamics. However, when applied to the higher hysteresis surfaces (Teflon and Teflon 120), the Davis-Hocking model restricts the mobility of the receding contact line to excess and the bulk coalescence dynamics are better captured by the Kistler model. Additionally, at these later times where contact line recession is occurring, the Kistler model more appropriately predicts the apparent contact angle and contact line position.

Moving to the coalescence metrics defined at the end of Section 7.3, the time evolutions of the projected x- and y-axis extensions are compared in Figure 7.6 for the four surfaces. In all cases, the Davis-Hocking model is able to accurately predict the time evolution of the projected y-axis extensions (y_p^*) for $0 \leq t^* \leq 3$. For the time evolution of the projected x-axis extensions (x_p^*), the Davis-Hocking model performs best for the Teflon 240 and Teflon 120 surfaces, of moderate ac-

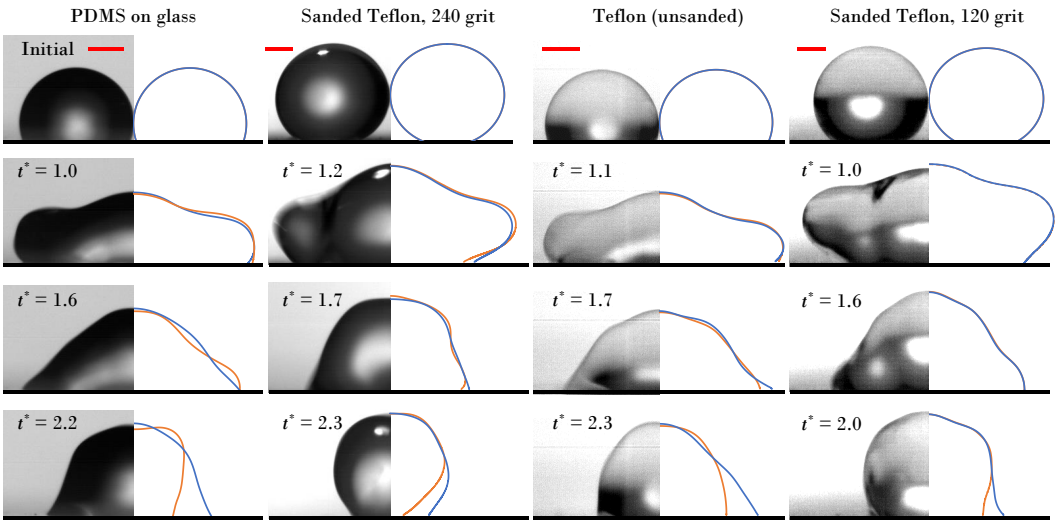

Figure 7.5: Comparison of side view coalescence dynamics (x-z plane): experiments (left) versus simulations (right). The Davis-Hocking model is represented by the blue line, while the Kistler model by the orange line. Scale bar (red line) is 0.5 mm in all cases.

curacy for PDMS, and poorly for Teflon. Based solely on x_p^* & y_p^* versus t^* behavior, the Davis-Hocking model appears to provide superior or comparable performance for three out of the four surfaces versus the Kistler model (specifically: PDMS, Teflon 240, and Teflon 120). This is confirmed by the coalescence dynamics comparison (Figure 7.5), although for the Teflon 120 surface, the Davis-Hocking contact line behavior begins to deviate from the experiment at $t^* = 2$ while the Kistler model still performs adequately. The Davis-Hocking model

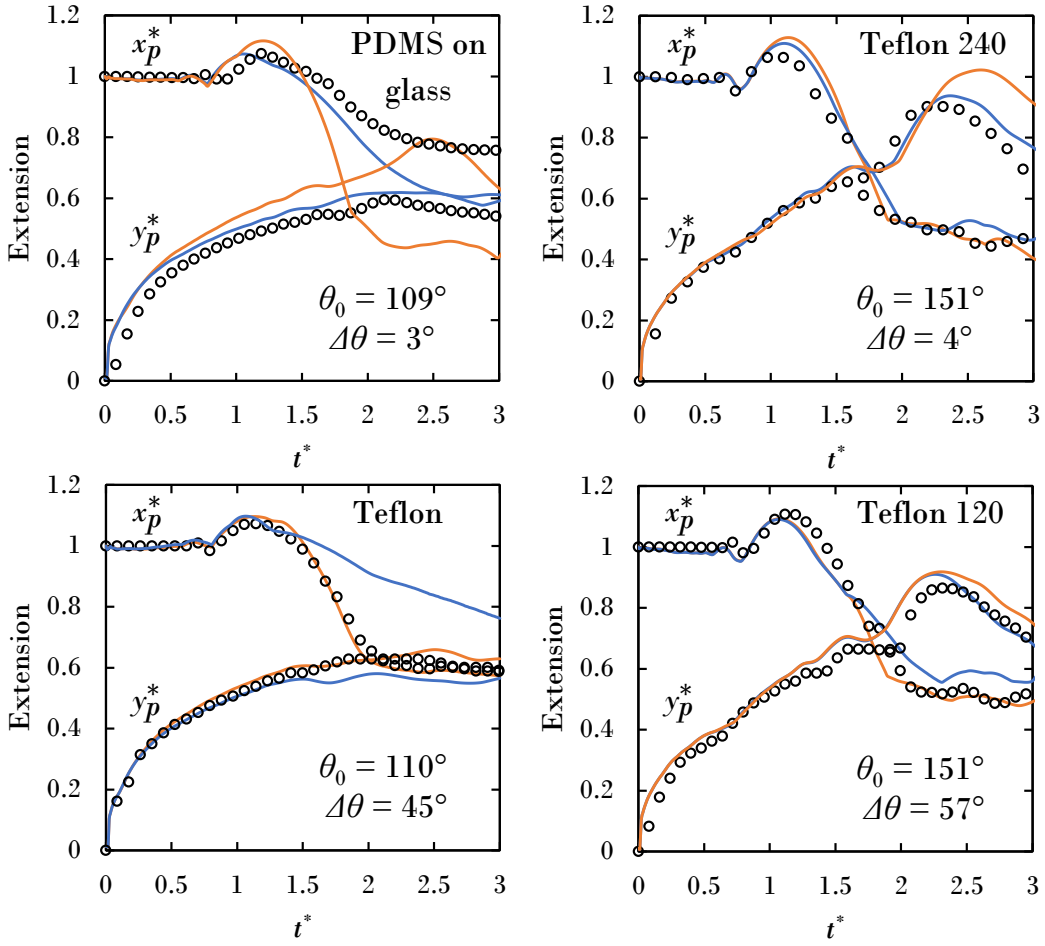

Figure 7.6: Time evolution of projected extensions: experiments (open circles) versus simulations (solid lines). The Davis-Hocking model is represented by the blue lines, while the Kistler model by the orange lines.

Table 7.6: Cumulative projected swept areas (normalized): experiment versus simulation.

Surface	$\mathcal{P}^*$, Experiment	$\mathcal{P}^*$, Davis-Hocking	$\mathcal{P}^*$, Kistler
PDMS on glass	1.27	1.24	1.39
Teflon (unsanded)	1.31	1.26	1.30
Sanded Teflon, 240 grit	1.51	1.55	1.63
Sanded Teflon, 120 grit	1.50	1.51	1.53

also better predicts the normalized cumulative projected swept areas ($\mathcal{P}^*$), Table 7.6, for the same three surfaces. Overall, the comparison of the side view dynamics gives the best indication of model performance versus experiment, with the coalescence metrics generally confirming.

7.4.3 Commentary

It is noteworthy that the Davis-Hocking model, despite using an M value strictly appropriate for inertial-capillary contact line motions, is able to reasonably approximate the experimental dynamics and contact line behavior in several of the cases. As to why the Davis-Hocking model performs less optimally in predicting the receding contact line motions on the higher contact angle hysteresis surfaces (Teflon and Teflon 120), it is possible that the M value employed during this time is inappropriate. That is, on the higher hysteresis surfaces, it may be the case that the advancing and receding motions have different associated M values. Recall that the single M value employed in the simulations was determined via a technique that averaged contributions from both advancing and receding contact line behavior. Although not performed in this work,

we remark that it is theoretically possible to extract different M values for the advancing and receding motions using the cyclically-dynamic contact angle goniometer of Xia & Steen. Going forward, it would be valuable to understand if using different M values for advancing and receding contact lines significantly increases the accuracy of the simulations.

Additional future studies should investigate when the linearity between the dynamic contact angle and contact line velocity breaks in the inertial-capillary regime, as the cyclically-dynamic contact angle goniometer presented by Xia & Steen is limited in the maximum velocity of the contact line excursions that can be tested. For example, the Teflon surface exhibited contact line velocities of -0.05 m/s $< U_{CL} <$ 0.08 m/s during the experimental determination of the mobility parameter. Of course, it is possible for a contact line to move with a velocity beyond this range which puts stress on the model in terms of the validity of the M value used for predicting dynamic contact angles. As the bounds of the dynamic contact angle ($0° \leq \theta \leq 180°$) are approached at higher contact line velocities, the linearity of $\eta\Delta\alpha$ versus ηU_{CL} cannot continue indefinitely.

Finally, the application of M to other fluid systems and types of dynamics would provide more confidence in its utility, specifically those that lie solely in the inertial-capillary regime (e.g. short-time dynamic wetting of a drop touching a surface). Sessile drop coalescence, with simultaneous advancing and receding motions (and transitions between the two), provides a demanding test of the mobility parameter especially given that all of the contact line motions are not strictly inertial-capillary in regime. However, the results are sufficiently promising to suggest that the mobility parameter is a value that can be measured independently and then applied to predict. We hope that these results

encourage other researchers to explore use of the mobility parameter for modeling rapid wetting and dewetting behaviors via the Davis-Hocking model.

7.5 Conclusion

In this work, we numerically simulate binary sessile water drop coalescence and compare the performance to experiments. The primary focus of the study is to investigate if an independently measured mobility parameter for the inertial-capillary regime can be utilized in a Davis-Hocking type dynamic contact angle model to accurately predict experimental behaviors. It is observed that a Davis-Hocking model utilizing the measured mobility parameter adequately anticipates the bulk coalescence dynamics and contact line behavior for several different surface types. This gives some indication that mobility is indeed a material-like parameter that can be measured in one context and then used to predict in another. Further, the Davis-Hocking model is able to outperform the widely used Kistler dynamic contact angle model in many cases. Additional experiments pertaining to this work, planned for launch to the International Space Station in late 2020, will soon provide further insights as to the mobility parameter and its overall versatility for predictive application in the realm of inertial-capillary contact line motions.

Author Contributions: PHS conceived the initial idea of the research. JML carried out the coalescence experiments and simulations, VRK performed the vibration experiments, and PHS guided the work. JML analyzed the coalescence data, while VRK analyzed the vibration data. JML and PHS wrote the paper.

PHS = Paul H. Steen, JML = Jonathan M. Ludwicki, VRK = Vanessa R. Kern

CHAPTER 8

FUTURE DIRECTIONS

8.1 Sessile Drop Coalescence and Sweeping

It is of interest to characterize coalescence sweeping behavior in applications and to understand how it assists in determining overall device behavior. For example, how does extent of coalescence sweeping affect liquid collection rates on water harvesting surfaces? As a second example, how does extent of sweeping affect heat transfer coefficients during dropwise condensation? Preliminary studies reported here show that surface temperature can affect the extent of coalescence sweeping during dropwise condensation, Figure 8.1. Could these sweeping differences lead to disparate surface refreshment rates for nucleation, which could in turn produce a shift in heat transfer coefficient? To answer, follow-up condensation heat transfer studies are thus necessary.

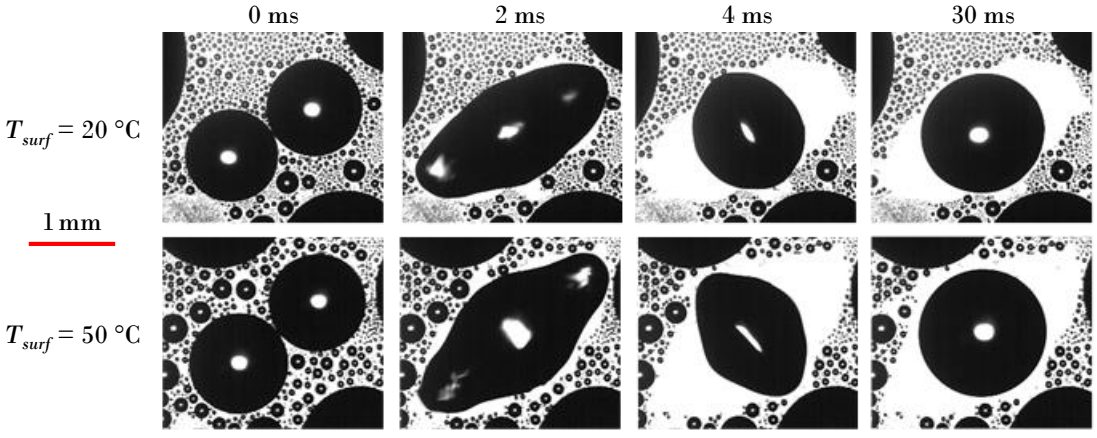

Figure 8.1: Top-view time progressions of sessile drop coalescence during steam dropwise condensation onto a quartz surface vapor silanized with dodecyltrichlorosilane ($\theta_0 \sim 100°$). Condenser surface temperatures are (top) 20 °C and (bottom) 50 °C.

For hydrophobic surfaces undergoing dropwise condensation, drop size (R) versus time (t) behavior has been characterized for coalescence growth with $R \sim t$ power-law behavior reported in the literature[65]. Can superhydrophobic surfaces surpass this $R \sim t$ behavior given their increased coalescence sweeping versus hydrophobic surfaces? This remains an open question.

Can multiple drops (say 10+ of identical size) be placed on a surface in such a fashion that upon coalescence of two of the drops, chain-reaction dynamics are able to capture all of the other drops on the surface? If feasible, one could think of engineering a condensing surface with selective nucleation sites that could then achieve this full surface sweeping upon growth of the trigger drops to sufficient size. This reliable turnover could lead to enhanced heat transfer performance during condensation.

Lastly, for real surfaces, surface roughness is always present at one or multiple length scales. As an example, micro- and/or nano-scale roughness is necessary to achieve superhydrophobicity. In this dissertation, simulations of sessile drop coalescence omit details related to surface texturing by enforcing wetting conditions on a flat surface. As additional designer substrates continue to be produced by researchers, it is necessary to understand how various surface features influence liquid behaviors during coalescence and when/if they are important to model so as to accurately capture the fluid dynamics. A preliminary study has recently been performed in this area by Attarzadeh and Dolatabadi[97].

8.2 Condensation Heat Transfer and Switchable Wettability

For flow condensers employing switchable wettability surfaces, a main challenge will be in transitioning between the filmwise and dropwise condensation modes as this requires the disruption of a continuous liquid film. One possibility is to employ local vibrations to atomize the film into drops which can then be entrained into the two-phase flow[274]. Also, for space applications, it is necessary to understand the effects of low-gravity on condensation processes. This is particularly true for the dropwise mode where data is extremely limited[156]. An issue that arises with dropwise condensation in reduced gravity is the removal of drops from the condensing surface. If drops are not cleared from the condensing surface at a sufficient rate, dropwise condensation transitions to filmwise condensation which reduces the heat transfer coefficient. In the absence of gravitational forces, it is suspected that drop movement can be accomplished by means of wettability gradients[45] or temperature gradients[275], among other methods[47,48]. In flow condensers, vapor flow shear-stress could also potentially influence drop motion[276]. In summary, open questions are:

- Is it possible to transition from filmwise to dropwise condensation during continual operation of a condenser?

- How do condensation heat transfer processes behave differently in low-gravity environments?

- Can dropwise mode condensation be sustained in a reduced gravity environment?

APPENDIX A

APPENDIX FOR CHAPTER 1

A.1 Effect of Artificial Interface Compression in OpenFOAM

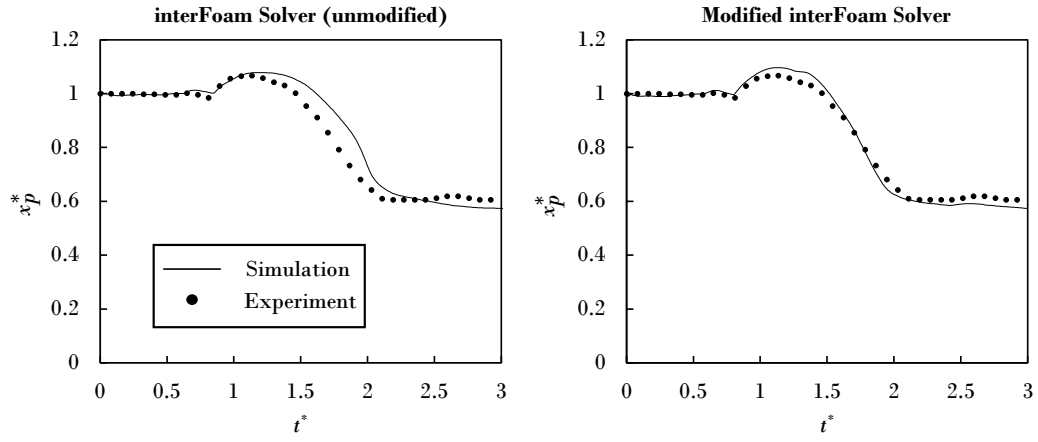

Figure A.1: Time response of the non-dimensional projected x-axis extension for the (left) unmodified interFoam solver with artificial anti-diffusive surface fluxes and (right) modified interFoam solver without artificial anti-diffusive surface fluxes. It is noted that the modified solver resolves the time lag between simulation and experiment. The system tested is Teflon-water-air where $\theta_0 = 110°$, $\theta_a = 120°$, and $\theta_r = 75°$.

A.2 Description of Supplemental Videos

Video A.1: Comparison of the top view fluid dynamics for experiment versus simulation. Left: Teflon-water-air system where $\theta_0 = 110°$, $\theta_a = 120°$, and $\theta_r = 75°$. Right: Sanded Teflon (120 grit)-water-air system where $\theta_0 = 151°$, $\theta_a = 159°$, and $\theta_r = 102°$.

Video A.2: Evolution of the non-dimensional projected swept area in time for θ_0 = 101°, θ_a = 106°, and θ_r = 91°.

Video A.3: Evolution of the non-dimensional projected swept area in time for θ_0 = 141°, θ_a = 146°, and θ_r = 131°.

Video material is available for download at https://www.proquest.com.

APPENDIX B

APPENDIX FOR CHAPTER 2

B.1 Dimensional Analysis of Sessile Drop Coalescence

The number of dimensionless groups relevant to sweeping by sessile drop coalescence sweeping can be determined via the Buckingham π theorem as:

No. of dimensionless groups = No. of variables - No. of fundamental units.

· Variables (11): arbitrary coalescence trajectory $\hat{x}$ (dependent variable), time t (independent variable), drop size D, initial contact angle θ_0, advancing contact angle deviation from the initial contact angle $\Delta\theta^+ \equiv \theta_a - \theta_0$, receding contact angle deviation from the initial contact angle $\Delta\theta^- \equiv \theta_0 - \theta_r$, liquid-gas surface tension σ_{lg}, liquid density ρ_l, gas density ρ_g, liquid viscosity μ_l, and gas viscosity μ_g.

· Fundamental units (3): length, mass, and time.

· Dimensionless groups ($11 - 3 = 8$): $\hat{x}^* = x/D$, $t^* = t/(\rho_l D^3/8\sigma_{lg})^{1/2}$, θ_0, $\Delta\theta^+$, $\Delta\theta^-$, $\rho^* = \rho_l/\rho_g$, $\mu^* = \mu_l/\mu_g$, and $\mathrm{Oh} = \mu_l/(\rho_l\sigma_{lg}D)^{1/2}$.

Then, $\hat{x}^* = f(t^*; \theta_0, \Delta\theta^+, \Delta\theta^-, \rho^*, \mu^*, \mathrm{Oh})$. For constant θ_0, $\Delta\theta^+$, $\Delta\theta^-$, ρ^*, μ^*, & Oh but different μ_l, μ_g, ρ_l, ρ_g, σ_{lg}, & D one checks if $\hat{x}^*$ vs. t^* collapses. Figure B.1 plots x_p^* & y_p^* vs. t^* for three cases, see Table B.1. At any t^*, for both x_p^* and y_p^*, the maximum percent difference between any of the two cases is less than 2%. That is, the collapse is excellent. This test provides another verification of the simulation fidelity.

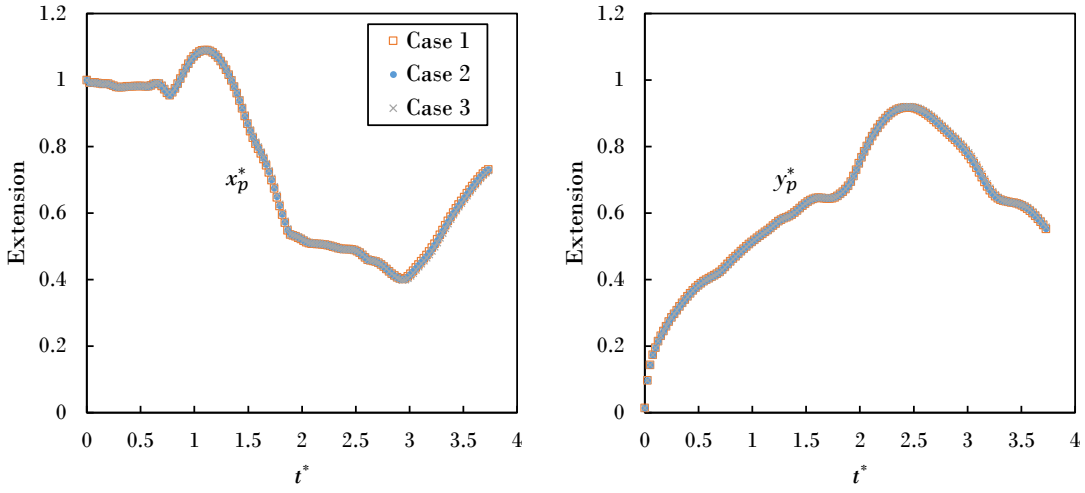

Figure B.1: Non-dimensional collapse in OpenFOAM: x_p^* & y_p^* versus t^* for three cases of sessile drop coalescence (Table B.1).

Table B.1: Simulation parameters relevant to the three cases of sessile drop coalescence reported in Figure B.1. In all cases, $\theta_0 = 141°$, $\Delta\theta^+ = 5°$, and $\Delta\theta^- = 10°$.

Case	ρ_l (kg/m^3)	ρ_g (kg/m^3)	μ_l (cP)	μ_g (cP)	σ_{lg} (J/m^2)	D (mm)
1	998	1.204	0.998	0.0181	0.072	0.72
2	998	1.204	0.998	0.0181	0.72	0.072
3	99,800	120.4	9.98	0.181	0.72	0.072

APPENDIX C

APPENDIX FOR CHAPTER 3

C.1 Condensation Chamber

A custom stainless steel vacuum chamber (internal dimensions 0.4 m x 0.4 m x 0.4 m) with a windowed door and multiple apertures is used as the condensation chamber (Kurt J. Lesker Co.), Figure C.1. Three resistive heater lines (DHT052060LD, Omega Engineering Inc.) are wrapped around the exterior of the chamber and used to heat the internal chamber walls above the saturation temperature of the vapor to prevent unwanted condensation. Cooling fluid is circulated through an interior-exterior flow loop via a recirculating chiller (NESLAB ThermoFlex 900, Thermo Fisher Scientific), with fluid passed into and out of the chamber via a pair of ConFlat (CF) liquid feedthroughs (Kurt J. Lesker Co.). A flow meter (104-8, McMillan Co.) is integrated along the inflow line to monitor the volumetric flowrate of the cooling fluid. Vapor is fed into the chamber via a stainless steel tube welded to an external reservoir. A bellows valve is integrated into the vapor line for metering the vapor input into the chamber. The vapor line is wrapped with a rope heater (HTC-030, Omega Engineering Inc.), while the reservoir is wrapped with a second rope heater (HTC-060, Omega Engineering Inc.). Type T thermocouples (Omega Engineering Inc.) are attached to the vacuum chamber, vapor line, and reservoir to monitor their temperatures. Each of the temperatures is fed back to an individual process controller (CNi16D, Omega Engineering Inc.) which regulates the electrical output to the resistive heater lines to maintain a particular setpoint temperature. A combination of roughing and turbomolecular vacuum pumps (Anest Iwata

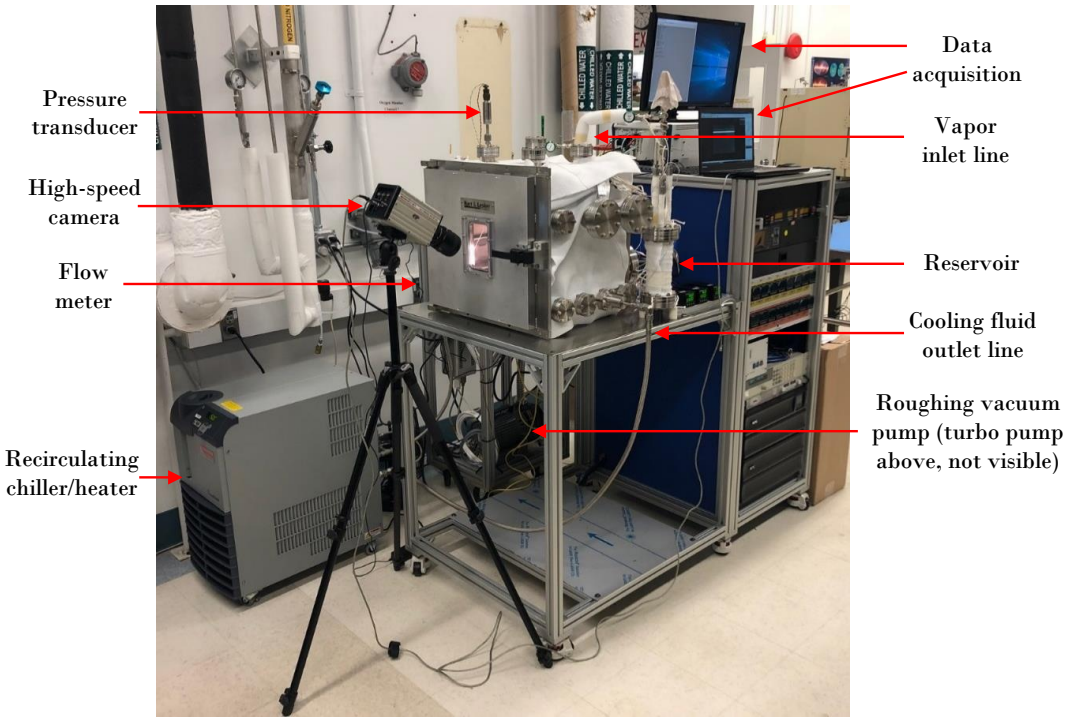

Figure C.1: Experimental setup: condensation chamber and exterior equipment.

Air Engineering Inc. and Pfeiffer Vacuum Technology AG, respectively) provide vacuum conditions within the chamber, while a pressure transducer (UNIK 5000, Druck Ltd.) monitors the chamber pressure. The chamber can be isolated from the vacuum pumps by way of a Klein Flansche (KF) manual butterfly valve (Kurt J. Lesker Co.). A gaseous nitrogen line with a bellows valve is attached to the chamber to serve as a means to bring the chamber back up to pressure after vacuum pump down. Electrical signals from resistance temperature detector (RTD) probes (Class 1/10DIN, Omega Engineering Inc.) within the chamber are passed to a digital multimeter (PXIe-4081, National Instruments Co.) outside the chamber via a CF multi-pin push-on feedthrough (Kurt J. Lesker Co.). RTD probes are operated in the four-wire configuration and have outer diameter 3.175 mm. The digital multimeter, which interfaces with a computer for

data recording, also accepts electrical signals from the pressure transducer and flow meter. Images of condensation on the sample surfaces are taken with a high-speed camera (Redlake MotionPro HS-3, DEL Imaging Systems LLC) via the windowed door. A fiber optic illuminator (41723-30, Cole Parmer Instrument Company LLC) is employed to provide back lighting for the high-speed camera. See Figure C.1 for an image of the exterior experimental setup.

C.2 Flow Loop

Inside the chamber, stainless steel tubing (6.35 mm outer diameter) and Swagelok compression fittings are employed to integrate with the sample section. RTD probes are fed into the flow loop to measure inlet & outlet cooling fluid temperatures to & from the sample section. See Figure C.2 for an image of the flow loop interior to the condensation chamber without any insulation.

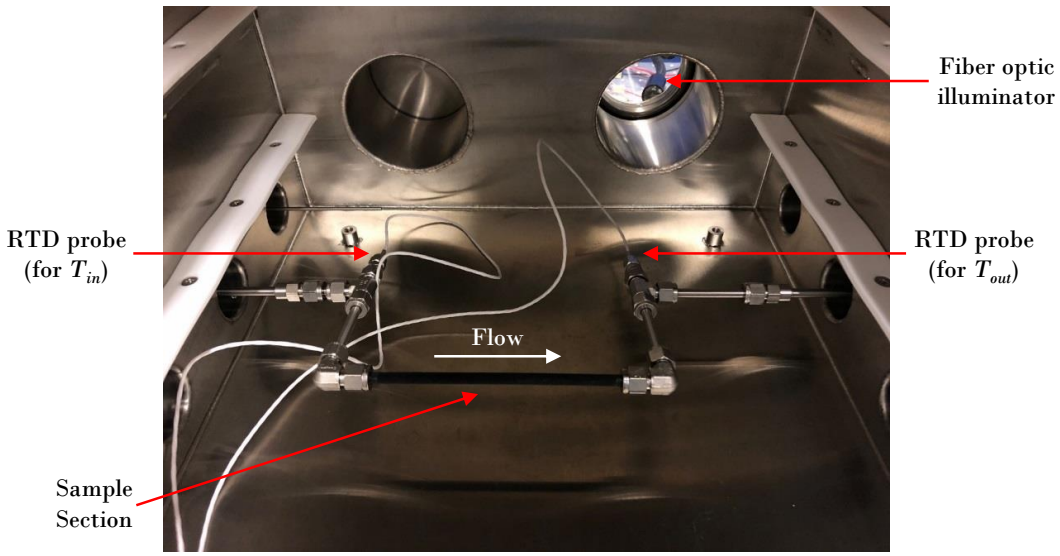

Figure C.2: Condensation chamber interior: flow loop with sample section and temperature probes.

During experiments, the interior stainless steel fixtures are insulated with buna-N/polyvinyl chloride foam insulation tubes (12.7 mm thick wall, McMaster-Carr Supply Co.). Outside the chamber, a combination of stainless steel tubing, flex hoses, and Swagelok compression fittings are used for the feed and return of fluid from the recirculating chiller.

C.3 Condensation Operational Procedure

To perform condensation experiments, the chamber is first isolated from the reservoir and nitrogen purge line by closing the associated bellows valves. The chamber is then evacuated to a pressure less than 0.1 Pa via the roughing and turbomolecular vacuum pumps to remove non-condensable gases. This pressure is verified via measurement by a second pressure transducer (Series 910, MKS Instruments Inc.) located just upstream of the turbomolecular pump. In parallel, during vacuum pump down, the fluid in the reservoir is boiled via heating by the rope heater under open atmosphere to remove dissolved gases. Additionally, the chamber walls are heated above the maximum anticipated vapor saturation temperature to prevent extraneous condensation at the inside chamber walls. Once the appropriate vacuum conditions are reached, the chamber is isolated from the vacuum pumps by closing the KF manual butterfly valve while the reservoir containing vapor is sealed from ambient air. Vapor is then released into the evacuated chamber by opening the associated bellows valve. By opening this valve to a certain extent, the operating pressure can be controlled to a particular steady-state; data is collected at the steady-state for at least one minute. The bellows valve is then adjusted to obtain a new steady-state pressure. During experiments, the inlet temperature of the cooling fluid into the

sample section, the outlet temperature of the cooling fluid from the sample section, the volumetric flowrate in the inflow line, and the chamber pressure are logged at a rate of ~ 0.3 Hz. These measurements are subsequently used to calculate relevant heat transfer information. For investigating condensation behavior below the lower critical solution temperature of the sample, the cooling fluid inlet temperature was set to T_{in} = 15°C with steam saturation temperatures of 20°C < T_s < 27.5°C. Analogously, for condensation above the lower critical solution temperature of the sample, an inlet temperature T_{in} = 35°C was utilized with steam saturation temperatures of 37.5°C < T_s < 42.5°C.

C.4 Uncertainty Analysis

The uncertainty in various calculated parameters (e.g. $\bar{U}$, q'', h) was determined by propagating the uncertainty of the experimentally measured variables (T_{in}, T_{out}, $\dot{Q}$, and T_s) according to the standards presented by the International Bureau of Weights and Measures[181]. Each experimentally measured variable has uncertainty arising from Type A and Type B contributions. Type A uncertainty accounts for the random variation of an experimental observation under the same conditions of measurement. Type B uncertainty accounts for the manufacturer's specification of accuracy related to a measurement device and/or data acquisition system. Typical uncertainties for the experimentally measured variables are reported in the paper. For the Gnielinski correlation, an uncertainty of ±10% was employed in accordance with other condensation studies where similar tube sizes (length and diameter) and flow conditions were used[190,215]. The Gnielinski correlation is often quoted as having an accuracy within ±15% of the calculated value[277], with some authors reporting an accu-

racy as tight as ±5% of the calculated value[6].

C.5 Electrical Potential-Responsive Wettability

As an alternative to temperature-responsive wettability, preliminary experiments have been performed relative to the fabrication of surfaces with electrical potential-responsive wettability. The goal was to produce a surface monolayer on copper that contains an acyclic alkyl chain terminated with an acyloxy group (that is, BG$-(CH_2)_x-COO^-$) where BG is a binding group and x is an integer) as these have been previously shown to exhibit switchable wettability in response to electrical potential[159]. The mechanism of switchable wettability is:

- When a negative electrical potential is applied to the surface, the chains straighten and expose the hydrophilic acyloxy groups

- When a positive electrical potential is applied to the surface, the chains bend and expose the hydrophobic alkyl chains

To fabricate a surface monolayer on copper that contains an acyclic alkyl chain terminated with an acyloxy group, the following scheme was proposed and followed:

(i) Remove the native oxide film on the copper surface via immersion in 2.0 M hydrochloric acid solution (10 minutes at room temperature)

(ii) Form a thin (i.e. hundreds of nm) copper (i) oxide layer on the copper surface via immersion in 50 wt% hydrogen peroxide solution (20 minutes at room temperature)

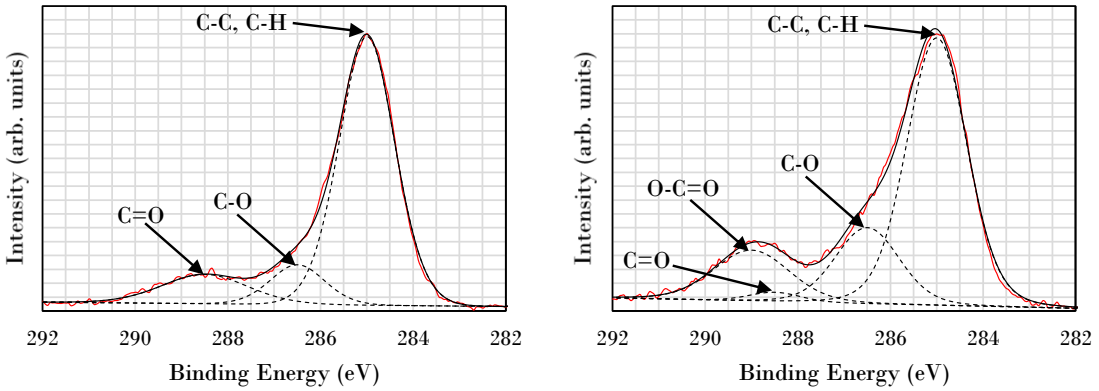

Figure C.3: C1s XPS spectra*: (left) post-TESUD deposition and (right) post-aldehyde oxidation to carboxylic acid.

(iii) Self-assemble a monolayer of 11-(triethoxysilyl)undecanal, or TESUD, onto the oxidized copper surface via vapor phase processing (60 minutes at room temperature; samples heated to ≈ 65 °C prior to processing to facilitate improved bonding of the silane to the surface)

(iv) Chemically oxidize the aldehyde functionality to a carboxylic acid group via immersion in dipropylene glycol dimethyl ether (10 hours at 80 °C)[278]

(v) Deprotonate the carboxylic acid groups using 0.1 M potassium hydroxide solution to form acyloxy functionalities (1 hour at room temperature)

After each processing step, water static contact angles were measured as an indirect way of confirming the appropriate chemical modification. In addition to contact angle measurements, X-ray photoelectron spectroscopy (XPS) was performed after selected steps to verify the chemical makeup of the surface. Figure C.3 shows the C1s XPS spectra post-TESUD deposition (left) and post-aldehyde oxidation to carboxylic acid (right). The C=O peak at 288.5 eV almost completely disappears after the oxidation processing step and a new peak is present at 289.0 eV corresponding to the presence of O–C=O groups. This lends

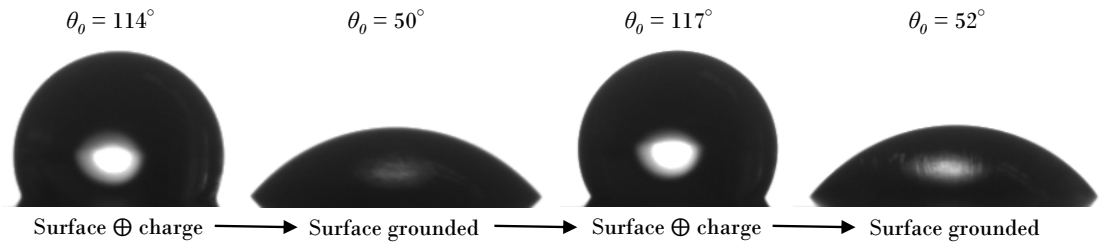

Figure C.4: Water static wettability: copper surface coated with an electrical potential-responsive monolayer for two switching cycles.

confidence that the aldehyde-termination has been converted to a carboxylic acid-termination. Additionally, an XPS survey scan taken post-TESUD deposition (not shown) exhibits a copper peak at ~933.0 eV indicating that the film is likely a monolayer since XPS analysis has a maximum X-ray penetration depth of ~10 nm. When grounded, the final surface exhibits a water static contact angle of 50° (hydrophilic). Conversely, when the surface is positively charged by induction, the water static contact angle increases to 115° (hydrophobic). Figure C.4 shows the wettability behavior for two switching cycles. This procedure worked successfully on high-purity copper tabs (15 mm x 15 mm x 1 mm). However, there was difficulty in scaling to a larger copper tube ($L \approx 13.5$ cm, D_o = 6.35 mm , D_i = 3.86 mm) for unknown reasons, but perhaps due to old chemicals. As such, the manipulation of condensation heat transfer was not tested on the electrical potential-responsive surfaces.

* The XPS work was performed at the Cornell Center for Materials Research (CCMR) Shared Facilities which are supported by the National Science Foundation's Materials Research Science and Engineering Center Program (DMR-1719875).

APPENDIX D

APPENDIX FOR CHAPTERS 6 & 7

D.1 Dynamic Contact Angle Models

A number of models exist for predicting the dynamic contact angle response to motion of the three-phase contact line. These models often find utility in computational fluid dynamics simulations where fluid is in contact with a solid. Here, some of the regularly utilized models by researchers are highlighted. The dynamic contact angle is known to depend on several variables[119], $\theta = f(\theta_a, \theta_r; Ca, We, Bo; \mu_l/\mu_g, \rho_l/\rho_g; ...)$, which these models capture to some degree or another. Additional dynamic contact angle models that are not emphasized here, such as the Shikhmurzaev model[279–281], are discussed by Blake[12].

Quasi-Dynamic or Perfect Slip Model[266,282]

The dynamic contact angle is based solely on whether the contact line is advancing or receding,

$$\theta = \theta_a \quad for\ U_{CL} > 0, \tag{D.1a}$$

$$\theta = \theta_r \quad for\ U_{CL} < 0. \tag{D.1b}$$

Note that the dynamic contact angle shows no dependence on the contact line velocity in the governing equations. Thus, contact angle hysteresis is captured but not the influence of the moving contact line on the dynamic contact angle.

Kistler Model[119]

The Kistler model estimates the dynamic contact angle response to contact line velocity via an empirical function $f(x)$ deduced from a systematic study of sil-

icone oils displacing air in glass capillaries, as performed by Hoffman[128]. In Hoffman's study, he showed a universal collapse of experimental data to a master curve, $\theta = f(Ca \equiv \mu U_{CL}/\sigma_{lg})$, for liquids that completely wet a solid surface covering capillary numbers 4 x $10^{-5} < Ca < 36$. Kistler provided an explicit and accurate mathematical equation for the curve as

$$f(x) = \cos^{-1}\left\{1 - 2\tanh\left[5.16\left(\frac{x}{1 + 1.31x^{0.99}}\right)^{0.706}\right]\right\}.$$

Kistler's model can be extended to partially wettable solid surfaces via the use of a shift factor $f^{-1}(\theta^*)$ where θ^* is a characteristic contact angle of the system (e.g. static, advancing, or receding contact angle). The modified Kistler model is then defined as

$$\theta = f[f^{-1}(\theta_a) + \frac{\mu U_{CL}}{\sigma_{lg}}] \quad for\ U_{CL} > 0, \tag{D.2a}$$

$$\theta = f[f^{-1}(\theta_r) + \frac{\mu U_{CL}}{\sigma_{lg}}] \quad for\ U_{CL} < 0. \tag{D.2b}$$

Davis-Hocking Model[241,242]

For deviations from a rest state contact angle $\Delta\alpha \equiv \theta - \theta^*$, dynamic contact angle response to contact line velocity is taken as linear yielding $M\Delta\alpha = U_{CL}$ where M is the mobility parameter. The Davis-Hocking model can be further modified to accommodate surfaces with hysteresis giving dynamic contact angles as

$$\theta = \theta_a + U_{CL}/M \quad for\ U_{CL} > 0, \tag{D.3a}$$

$$\theta = \theta_r + U_{CL}/M \quad for\ U_{CL} < 0. \tag{D.3b}$$

Cox-Voinov Model[231,263]

The Cox-Voinov model introduces slip at the contact line to remove the stress singularity[283] that occurs when one fluid displaces a second immiscible fluid

(for example, water-air) at a solid. Solving the associated governing equations via matched asymptotic expansion yields

$$\theta = g^{-1}\left(g(\theta^*) + Ca \ln (L/l)\right) \tag{D.4}$$

where g is a function, L is a characteristic macroscopic length, and l is a microscopic slip length. Polynomial approximations of g and g^{-1} are reported elsewhere[139].

APPENDIX E

DATA ARCHIVING FOR FEDERAL GRANTS

Note: the data referenced in this Appendix, for work performed on federally funded grants, is stored on the Steen Group Server at Cornell University.

Chapter 1: Sweeping by Sessile Drop Coalescence (NSF #1637960)

· Simulation data: g_phs\Jon Ludwicki\OpenFOAM

· Experimental data: g_phs\Jon Ludwicki\Drop Coalescence

Chapter 2: Sweeping by Sessile Drop Coalescence. Part 2: Effect of Contact Angle Hysteresis (NSF #1637960)

· Simulation data: g_phs\Jon Ludwicki\OpenFOAM

· Experimental data: n/a

Chapter 3: Switchable Wettability for Condensation Heat Transfer (NASA #80NSSC17K0144)

· Simulation data: n/a

· Experimental data: g_phs\Jon Ludwicki\NSTRF and g_phs\Jon Ludwicki\Contact Angle Measurement\Nanostructured CuO - PNIPAAm

Chapter 6: Unmasking Contact Line Mobility for Inertial-Capillary Spreading using Drop Vibration and Coalescence (NSF #1637960)

· Simulation data: g_phs\Jon Ludwicki\OpenFOAM

· Experimental data: g_phs\Jon Ludwicki\Close Out\ISVWC and g_phs\Jon

Ludwicki\Contact Angle Measurement\ISS Work

Chapter 7: Is Mobility a Material-Like Parameter? (NSF #1637960)

· Simulation data: g_phs\Jon Ludwicki\OpenFOAM

· Experimental data: g_phs\Jon Ludwicki\Drop Coalescence

REFERENCES

[1] Lester Haar, John S. Gallagher, and George S. Kell. *NBS/NRC Steam Tables*. Hemisphere Publishing Corporation, 1984.

[2] Thomas Young. An essay on the cohesion of fluids. *Phil. Trans. R. Soc.*, 95: 65–87, 1805.

[3] Pierre-Gilles de Gennes, Françoise Brochard-Wyart, and David Quéré. *Capillarity and Wetting Phenomena*. Springer, 2004.

[4] T. Onda, S. Shibuichi, N. Satoh, and K. Tsujii. Super-Water-Repellent Fractal Surfaces. *Langmuir*, 12:2125–2127, 1996.

[5] Chris J. Evans and James B. Bryan. "Structured", "Textured" or "Engineered" Surfaces. *CIRP Annals*, 48:541–556, 1999.

[6] Nenad Miljkovic, Ryan Enright, Youngsuk Nam, Ken Lopez, Nicholas Dou, Jean Sack, and Evelyn N. Wang. Jumping-Droplet-Enhanced Condensation on Scalable Superhydrophobic Nanostructured Surfaces. *Nano Lett.*, 13:179–187, 2013.

[7] Youmin Hou, Miao Yu, Xuemei Chen, Zuankai Wang, and Shuhuai Yao. Recurrent Filmwise and Dropwise Condensation on a Beetle Mimetic Surface. *ACS Nano*, 9:71–81, 2015.

[8] C. Antonini, M. Innocenti, T. Horn, M. Marengo, and A. Amirfazli. Understanding the effect of superhydrophobic coatings on energy reduction in anti-icing systems. *Cold Reg. Sci. Technol.*, 67:58–67, 2011.

[9] P. G. de Gennes. Wetting: statics and dynamics. *Rev. Mod. Phys.*, 57:827–863, 1985.

[10] Michel Y. Louge. Statistical mechanics of the triple contact line. *Phys. Rev. E*, 95:032804, 2017.

[11] E. B. Dussan V. On the Spreading of Liquids on Solid Surfaces: Static and Dynamic Contact Lines. *Annu. Rev. Fluid Mech.*, 11:371–400, 1979.

[12] Terence D. Blake. The physics of moving wetting lines. *J. Colloid Interface Sci.*, 299:1–13, 2006.

[13] Daniel Bonn, Jens Eggers, Joseph Indekeu, Jacques Meunier, and Etienne Rolley. Wetting and spreading. *Rev. Mod. Phys.*, 81:739–805, 2009.

[14] Jacco H. Snoeijer and Bruno Andreotti. Moving Contact Lines: Scales, Regimes, and Dynamical Transitions. *Annu. Rev. Fluid Mech.*, 45:269–292, 2013.

[15] URL `https://apps.webofknowledge.com`.

[16] Y. L. Chen, C. A. Helm, and J. N. Israelachvili. Molecular Mechanisms Associated with Adhesion and Contact Angle Hysteresis of Monolayer Surfaces. *J. Phys. Chem.*, 95:10736–10747, 1991.

[17] Mike Wei, Robert S. Bowman, John L. Wilson, and Norman R. Morrow. Wetting Properties and Stability of Silane-Treated Glass Exposed to Water, Air, and Oil. *J. Colloid Interface Sci.*, 157:154–159, 1993.

[18] C. W. Extrand and Y. Kumagai. An Experimental Study of Contact Angle Hysteresis. *J. Colloid Interface Sci.*, 191:378–383, 1997.

[19] Alexander Y. Fadeev and Thomas J. McCarthy. Trialkylsilane Monolayers Covalently Attached to Silicon Surfaces: Wettability Studies Indicat-

ing that Molecular Topography Contributes to Contact Angle Hysteresis. *Langmuir*, 15:3759–3766, 1999.

[20] C. W. Extrand. Contact Angles and Hysteresis on Surfaces with Chemically Heterogeneous Islands. *Langmuir*, 19:3793–3796, 2003.

[21] R. Narhe, D. Beysens, and V. S. Nikolayev. Contact Line Dynamics in Drop Coalescence and Spreading. *Langmuir*, 20:1213–1221, 2004.

[22] Nikil Kapur and Philip H. Gaskell. Morphology and dynamics of droplet coalescence on a surface. *Phys. Rev. E*, 75:056315, 2007.

[23] Bharat Bhushan and Eun Kyu Her. Fabrication of Superhydrophobic Surfaces with High and Low Adhesion Inspired from Rose Petal. *Langmuir*, 26:8207–8217, 2010.

[24] Bharat Bhushan and Michael Nosonovsky. The rose petal effect and the modes of superhydrophobicity. *Phil. Trans. R. Soc. A*, 368:4713–4728, 2010.

[25] Michael A. Nilsson, Robert J. Daniello, and Jonathan P. Rothstein. A novel and inexpensive technique for creating superhydrophobic surfaces using Teflon and sandpaper. *J. Phys. D.*, 43:045301, 2010.

[26] Liming Wang, Jingjing Wei, and Zhaohui Su. Fabrication of Surfaces with Extremely High Contact Angle Hysteresis from Polyelectrolyte Multilayer. *Langmuir*, 27:15299–15304, 2011.

[27] Nenad Miljkovic, Ryan Enright, and Evelyn N. Wang. Modeling and Optimization of Superhydrophobic Condensation. *J. Heat Transfer*, 135:111004, 2013.

[28] Youngsuk Nam, Donghyun Seo, Choongyeop Lee, and Seungwon Shin. Droplet coalescence on water repellant surfaces. *Soft Matter*, 11:154–160, 2015.

[29] Hyeongyun Cha, Jae Min Chun, Jesus Sotelo, and Nenad Miljkovic. Focal Plane Shift Imaging for the Analysis of Dynamic Wetting Processes. *ACS Nano*, 10:8223–8232, 2016.

[30] Fuqiang Chu, Xiaomin Wu, Yi Zhu, and Zhiping Yuan. Relationship between condensed droplet coalescence and surface wettability. *Int. J. Heat Mass Transf.*, 111:836–841, 2017.

[31] Jonathan M. Ludwicki, Franklin L. Robinson, and Paul H. Steen. Switchable Wettability for Condensation Heat Transfer. *ACS Appl. Mater. Interfaces*, 12:22115–22119, 2020.

[32] E. Schmidt, W. Schurig, and W. Sellschopp. Versuche über die Kondensation von Wasserdampf in Film- und Tropfenform. *Tech. Mech. Thermodyn.*, 1:53–63, 1930.

[33] E. J. Le Fevre and J. W. Rose. An Experimental Study of Heat Transfer by Dropwise Condensation. *Int. J. Heat Mass Transf.*, 8:1117–1133, 1965.

[34] Sunwoo Kim and Kwang J. Kim. Dropwise Condensation Modeling Suitable for Superhydrophobic Surfaces. *J. Heat Transfer*, 133:081502, 2011.

[35] Nicholas Fatica and Donald L. Katz. Dropwise Condensation. *Chem. Eng. Prog.*, 45:661–674, 1949.

[36] Takashi Nishino, Masashi Meguro, Katsuhiko Nakamae, Motonori Matsushita, and Yasukiyo Ueda. The Lowest Surface Free Energy Based on $-CF_3$ Alignment. *Langmuir*, 15:4321–4323, 1999.

[37] Robert N. Wenzel. Resistance of Solid Surfaces to Wetting by Water. *Ind. Eng. Chem.*, 28:988–994, 1936.

[38] A. B. D. Cassie and S. Baxter. Wettability of Porous Surfaces. *Trans. Faraday Soc.*, 40:546–551, 1944.

[39] Guangming Liu, Lan Fu, Andrei V. Rode, and Vincent S. J. Craig. Water Droplet Motion Control on Superhydrophobic Surfaces: Exploiting the Wenzel-to-Cassie Transition. *Langmuir*, 27:2595–2600, 2011.

[40] Nenad Miljkovic, Ryan Enright, and Evelyn N. Wang. Effect of Droplet Morphology on Growth Dynamics and Heat Transfer during Condensation on Superhydrophobic Nanostructured Surfaces. *ACS Nano*, 6:1776–1785, 2012.

[41] J. W. Rose and L. R. Glicksman. Dropwise condensation—The distribution of drop sizes. *Int. J. Heat Mass Transf.*, 16:411–425, 1973.

[42] Wen Hai Wu and Jer Ru Maa. On the Heat Transfer in Dropwise Condensation. *Chem. Eng. J.*, 12:225–231, 1976.

[43] P. Dimitrakopoulos and J. J. L. Higdon. On the gravitational displacement of three-dimensional fluid droplets from inclined solid surfaces. *J. Fluid Mech.*, 395:181–209, 1999.

[44] J. R. Maa. Drop size distribution and heat flux of dropwise condensation. *Chem. Eng. J.*, 16:171–176, 1978.

[45] Ashley M. Macner, Susan Daniel, and Paul H. Steen. Condensation on Surface Energy Gradient Shifts Drop Size Distribution toward Small Drops. *Langmuir*, 30:1788–1798, 2014.

[46] Yoshio Utaka and Tomoki Kamiyama. Condensate drop movement in Marangoni condensation by applying bulk temperature gradient on heat transfer surface. *Heat Transf. - Asian Res.*, 37:387–397, 2008.

[47] Mingxiang Luo, Rohini Gupta, and Joelle Frechette. Modulating Contact Angle Hysteresis To Direct Fluid Droplets along a Homogenous Surface. *ACS Appl. Mater. Interfaces*, 4:890–896, 2012.

[48] Srinivas Mettu and Manoj K. Chaudhury. Motion of Liquid Drops on Surfaces Induced by Asymmetric Vibration: Role of Contact Angle Hysteresis. *Langmuir*, 27:10327–10333, 2011.

[49] Jonathan B. Boreyko and Chuan-Hua Chen. Self-Propelled Dropwise Condensate on Superhydrophobic Surfaces. *Phys. Rev. Lett.*, 103:184501, 2009.

[50] Hiroaki Tanaka. A Theoretical Study of Dropwise Condensation. *J. Heat Transfer*, 97:72–78, 1975.

[51] Clark Graham and Peter Griffith. Drop Size Distributions and Heat Transfer in Dropwise Condensation. *Int. J. Heat Mass Transf.*, 16:337–346, 1973.

[52] A. W. Neumann, A. H. Abdelmessih, and A. Hameed. The Role of Contact Angles and Contact Angle Hysteresis in Dropwise Condensation Heat Transfer. *Int. J. Heat Mass Transf.*, 21:947–953, 1978.

[53] H. Jeremy Cho, Daniel J. Preston, Yangying Zhu, and Evelyn N. Wang. Nanoengineered materials for liquid-vapour phase-change heat transfer. *Nat. Rev. Mater.*, 2:16092, 2016.

[54] J. M. Ludwicki and P. H. Steen. Sweeping by Sessile Drop Coalescence. *Eur. Phys. J. Special Topics*, 2020. Accepted.

[55] Koji Takeda, Akira Nakajima, Yuji Murata, Kazuhito Hashimoto, and Toshiya Watanabe. Control of Water Droplets on Super-Hydrophobic Surfaces by Static Electric Field. *Jpn. J. Appl. Phys.*, 41:287–291, 2002.

[56] Peichun Tsai, Sergio Pacheco, Christophe Pirat, Leon Lefferts, and Detlef Lohse. Drop impact upon micro- and nanostructured superhydrophobic surfaces. *Langmuir*, 25:12293–12298, 2009.

[57] Golrokh Heydari, Esben Thormann, Mikael Järn, Eric Tyrode, and Per M. Claesson. Hydrophobic surfaces: Topography effects on wetting by supercooled water and freezing delay. *J. Phys. Chem. C*, 117:21752–21762, 2013.

[58] Susmita Dash and Suresh V. Garimella. Droplet evaporation on heated hydrophobic and superhydrophobic surfaces. *Phys. Rev. E*, 89:042402, 2014.

[59] Faryar Tavakoli and H. Pirouz Kavehpour. Cold-induced spreading of water drops on hydrophobic surfaces. *Langmuir*, 31:2120–2126, 2015.

[60] A. Menchaca-Rocha, A. Martínez-Dávalos, R. Núñez, S Popinet, and S. Zaleski. Coalescence of liquid drops by surface tension. *Phys. Rev. E*, 63:046309, 2001.

[61] Michael A. Nilsson and Jonathan P. Rothstein. The effect of contact angle hysteresis on droplet coalescence and mixing. *J. Colloid Interface Sci.*, 363: 646–654, 2011.

[62] H. Pirouz Kavehpour. Coalescence of Drops. *Annu. Rev. Fluid Mech.*, 47: 245–268, 2015.

[63] Katrina M. Wisdom, Jolanta A. Watson, Xiaopeng Qu, Fangjie Liu, Gregory S. Watson, and Chuan-Hua Chen. Self-cleaning of superhydropho-

bic surfaces by self-propelled jumping condensate. *Proc. Natl. Acad. Sci. U.S.A.*, 110:7992–7997, 2013.

[64] Jonathan B. Boreyko and C. Patrick Collier. Delayed frost growth on jumping-drop superhydrophobic surfaces. *ACS Nano*, 7:1618–1627, 2013.

[65] Daniel Beysens. Dew nucleation and growth. *Comptes Rendus Phys.*, 7: 1082–1100, 2006.

[66] Paul Meakin. Droplet deposition growth and coalescence. *Reports Prog. Phys.*, 55:157–240, 1992.

[67] Jens Eggers, John R. Lister, and Howard A. Stone. Coalescence of liquid drops. *J. Fluid Mech.*, 401:293–310, 1999.

[68] L. Duchemin, J. Eggers, and C. Josserand. Inviscid coalescence of drops. *J. Fluid Mech.*, 487:167–178, 2003.

[69] W. D. Ristenpart, P. M. McCalla, R. V. Roy, and H. A. Stone. Coalescence of spreading droplets on a wettable substrate. *Phys. Rev. Lett.*, 97:064501, 2006.

[70] Mathieu Sellier and Emmanuel Trelluyer. Modeling the Coalescence of Sessile Droplets. *Biomicrofluidics*, 3:022412, 2009.

[71] Min Wook Lee, Dong Kyun Kang, Sam S. Yoon, and Alexander L. Yarin. Coalescence of two drops on partially wettable substrates. *Langmuir*, 28: 3791–3798, 2012.

[72] J. F. Hernández-Sánchez, L. A. Lubbers, A. Eddi, and J. H. Snoeijer. Symmetric and asymmetric coalescence of drops on a substrate. *Phys. Rev. Lett.*, 109:184502, 2012.

[73] Yi Sui, Marco Maglio, Peter D. M. Spelt, Dominique Legendre, and Hang Ding. Inertial coalescence of droplets on a partially wetting substrate. *Phys. Fluids*, 25:101701, 2013.

[74] A. Eddi, K. G. Winkels, and J. H. Snoeijer. Influence of Droplet Geometry on the Coalescence of Low Viscosity Drops. *Phys. Rev. Lett.*, 111:144502, 2013.

[75] Surjyasish Mitra and Sushanta K. Mitra. Symmetric drop coalescence on an under-liquid substrate. *Phys. Rev. E*, 92:033013, 2015.

[76] Shripad J. Gokhale, Sunando DasGupta, Joel L. Plawsky, and Peter C. Wayner, Jr. Reflectivity-based evaluation of the coalescence of two condensing drops and shape evolution of the coalesced drop. *Phys. Rev. E*, 70:051610, 2004.

[77] Q. Liao, X. Zhu, S. M. Xing, and H. Wang. Visualization study on coalescence between pair of water drops on inclined surfaces. *Exp. Therm. Fluid Sci.*, 32:1647–1654, 2008.

[78] Yu-Hsuan Lai, Miao-Hsing Hsu, and Jing-Tang Yang. Enhanced mixing of droplets during coalescence on a surface with a wettability gradient. *Lab Chip*, 10:3149–3156, 2010.

[79] Hong Wang, Qiang Liao, Xun Zhu, Jun Li, and Xin Tian. Experimental Studies of Liquid Droplet Coalescence on the Gradient Surface. *J. Supercond. Nov. Magn.*, 23:1165–1168, 2010.

[80] Guiping Zhu, Hui Fan, Hulin Huang, and Fei Duan. Coalescence of droplets on micro-structure patterned hydrophobic planar solid surfaces. *RSC Adv.*, 7:23954–23960, 2017.

[81] Praveen M. Somwanshi, K. Muralidhar, and Sameer Khandekar. Coalescence dynamics of sessile and pendant liquid drops placed on a hydrophobic surface. *Phys. Fluids*, 30:092103, 2018.

[82] C. Andrieu, D. A. Beysens, V. S. Nikolayev, and Y. Pomeau. Coalescence of sessile drops. *J. Fluid Mech.*, 453:427–438, 2002.

[83] R. Narhe, D. Beysens, and V. S. Nikolayev. Dynamics of Drop Coalescence on a Surface: The Role of Initial Conditions and Surface Properties. *Int. J. Thermophys.*, 26:1743–1757, 2005.

[84] D. A. Beysens and R. D. Narhe. Contact Line Dynamics in the Late-Stage Coalescence of Diethylene Glycol Drops. *J. Phys. Chem. B*, 110:22133–22135, 2006.

[85] R. D. Narhe, D. A. Beysens, and Y. Pomeau. Dynamic Drying in the Early-Stage Coalescence of Droplets Sitting on a Plate. *Europhys. Lett.*, 81:46002, 2008.

[86] R. D. Narhe, M. D. Khandkar, P. B. Shelke, A. V. Limaye, and D. A. Beysens. Condensation-induced jumping water drops. *Phys. Rev. E*, 80: 031604, 2009.

[87] Jonathan B. Boreyko and Chuan-Hua Chen. Self-propelled jumping drops on superhydrophobic surfaces. *Phys. Fluids*, 22:091110, 2010.

[88] Feng-Chao Wang, Fuqian Yang, and Ya-Pu Zhao. Size effect on the coalescence-induced self-propelled droplet. *Appl. Phys. Lett.*, 98:053112, 2011.

[89] Benli Peng, Sifang Wang, Zhong Lan, Wei Xu, Rongfu Wen, and Xuehu

Ma. Analysis of droplet jumping phenomenon with lattice Boltzmann simulation of droplet coalescence. *Appl. Phys. Lett.*, 102:151601, 2013.

[90] Youngsuk Nam, Hyunsik Kim, and Seungwon Shin. Energy and hydrodynamic analyses of coalescence-induced jumping droplets. *Appl. Phys. Lett.*, 103:161601, 2013.

[91] Xiuliang Liu, Ping Cheng, and Xiaojun Quan. Lattice Boltzmann simulations for self-propelled jumping of droplets after coalescence on a superhydrophobic surface. *Int. J. Heat Mass Transf.*, 73:195–200, 2014.

[92] Fangjie Liu, Giovanni Ghigliotti, James J. Feng, and Chuan-Hua Chen. Numerical simulations of self-propelled jumping upon drop coalescence on non-wetting surfaces. *J. Fluid Mech.*, 752:39–65, 2014.

[93] Ryan Enright, Nenad Miljkovic, James Sprittles, Kevin Nolan, Robert Mitchell, and Evelyn N. Wang. How Coalescing Droplets Jump. *ACS Nano*, 8:10352–10362, 2014.

[94] Xiuliang Liu and Ping Cheng. 3D multiphase lattice Boltzmann simulations for morphological effects on self-propelled jumping of droplets on textured superhydrophobic surfaces. *Int. Commun. Heat Mass Transf.*, 64: 7–13, 2015.

[95] Samaneh Farokhirad, Jeffrey F. Morris, and Taehun Lee. Coalescence-induced jumping of droplet: Inertia and viscosity effects. *Phys. Fluids*, 27:102102, 2015.

[96] Kai Wang, Qianqing Liang, Rui Jiang, Yi Zheng, Zhong Lan, and Xuehu Ma. Self-enhancement of droplet jumping velocity: the interaction of liquid bridge and surface texture. *RSC Adv.*, 6:99314–99321, 2016.

[97] Reza Attarzadeh and Ali Dolatabadi. Coalescence-induced jumping of micro-droplets on heterogeneous superhydrophobic surfaces. *Phys. Fluids*, 29:012104, 2017.

[98] Kai Wang, Qianqing Liang, Rui Jiang, Yi Zheng, Zhong Lan, and Xuehu Ma. Numerical Simulation of Coalescence-Induced Jumping of Multidroplets on Superhydrophobic Surfaces: Initial Droplet Arrangement Effect. *Langmuir*, 33:6258–6268, 2017.

[99] Qiang Sheng, Jie Sun, Wen Wang, Hua Sheng Wang, and Colin G. Bailey. How solid surface free energy determines coalescence-induced nanodroplet jumping: A molecular dynamics investigation. *J. Appl. Phys.*, 122:245301, 2017.

[100] Timothée Mouterde, Thanh-Vinh Nguyen, Hidetoshi Takahashi, Christophe Clanet, Isao Shimoyama, and David Quéré. How merging droplets jump off a superhydrophobic surface: Measurements and model. *Phys. Rev. Fluids*, 2:112001(R), 2017.

[101] Kai Wang, Ruixin Li, Qianqing Liang, Rui Jiang, Yi Zheng, Zhong Lan, and Xuehu Ma. Critical size ratio for coalescence-induced droplet jumping on superhydrophobic surfaces. *Appl. Phys. Lett.*, 111:061603, 2017.

[102] Joram Wasserfall, Patric Figueiredo, Reinhold Kneer, Wilko Rohlfs, and Philipp Pischke. Coalescence-induced droplet jumping on superhydrophobic surfaces: Effects of droplet mismatch. *Phys. Rev. Fluids*, 2: 123601, 2017.

[103] Peng Zhang, Yota Maeda, Fengyong Lv, Yasuyuki Takata, and Daniel Orejon. Enhanced Coalescence-Induced Droplet-Jumping on Nanostructured

Superhydrophobic Surfaces in the Absence of Microstructures. *ACS Appl. Mater. Interfaces*, 9:35391–35403, 2017.

[104] Y. Shi and G. H. Tang. Investigation of coalesced droplet vertical jumping and horizontal moving on textured surface using the lattice Boltzmann method. *Comput. Math. with Appl.*, 75:1213–1225, 2018.

[105] Fuqiang Chu, Zhiping Yuan, Xuan Zhang, and Xiaomin Wu. Energy analysis of droplet jumping induced by multi-droplet coalescence: The influences of droplet number and droplet location. *Int. J. Heat Mass Transf.*, 121: 315–320, 2018.

[106] Shan Gao, Quanwen Liao, Wei Liu, and Zhichun Liu. Coalescence-Induced Jumping of Nanodroplets on Textured Surfaces. *J. Phys. Chem. Lett.*, 9:13–18, 2018.

[107] Yan Chen and Yongsheng Lian. Numerical investigation of coalescence-induced self-propelled behavior of droplets on non-wetting surfaces. *Phys. Fluids*, 30:112102, 2018.

[108] Shan Gao, Quanwen Liao, Wei Liu, and Zhichun Liu. Self-Removal of Multiple and Multisize Coalescing Nanodroplets on Nanostructured Surfaces. *J. Phys. Chem. C*, 122:20521–20526, 2018.

[109] Zhiping Yuan, Renzhi Wu, and Xiaomin Wu. Numerical simulations of multi-hop jumping on superhydrophobic surfaces. *Int. J. Heat Mass Transf.*, 135:345–353, 2019.

[110] Hong Wang, Xun Zhu, Qiang Liao, and P. C. Sui. Numerical Simulation on Coalescence Between a Pair of Drops on Homogeneous Horizon-

tal Surface with Volume-of-Fluid Method. *J. Supercond. Nov. Magn.*, 23: 1137–1140, 2010.

[111] Majid Ahmadlouydarab and James J. Feng. Motion and coalescence of sessile drops driven by substrate wetting gradient and external flow. *J. Fluid Mech.*, 746:214–235, 2014.

[112] S. Moghtadernejad, M. Tembely, M. Jadidi, N. Esmail, and A. Dolatabadi. Shear driven droplet shedding and coalescence on a superhydrophobic surface. *Phys. Fluids*, 27:032106, 2015.

[113] Donghyun Seo, Seungtae Oh, Seungwon Shin, and Youngsuk Nam. Dynamic heat transfer analysis of condensed droplets growing and coalescing on water repellent surfaces. *Int. J. Heat Mass Transf.*, 114:934–943, 2017.

[114] Shahab Mirjalili, Christopher B. Ivey, and Ali Mani. Comparison between the diffuse interface and volume of fluid methods for simulating two-phase flows. *Int. J. Multiph. Flow*, 116:221–238, 2019.

[115] Shawn Dodds, Marcio S. Carvalho, and Satish Kumar. The dynamics of three-dimensional liquid bridges with pinned and moving contact lines. *J. Fluid Mech.*, 707:521–540, 2012.

[116] Chung-Hsuan Huang, Marcio S. Carvalho, and Satish Kumar. Electrostatic assist of liquid transfer between plates and cavities. *Phys. Rev. Fluids*, 4:044005, 2019.

[117] Yulii D. Shikhmurzaev. *Capillary Flows with Forming Interfaces, 1st Edition* . Taylor & Francis Group, 2007.

[118] Chen-Yu Liu, Eric Vandre, Marcio S. Carvalho, and Satish Kumar. Dynamic wetting failure and hydrodynamic assist in curtain coating. *J. Fluid Mech.*, 808:290–315, 2016.

[119] S. F. Kistler. Hydrodynamics of wetting. In J. C. Berg, editor, *Wettability*, pages 311–430. Marcel Dekker, New York, 1993.

[120] H. G. Weller, G. Tabor, H. Jasak, and C. Fureby. A tensorial approach to computational continuum mechanics using object-oriented techniques. *Comput. Phys.*, 12:620–631, 1998.

[121] URL `http://www.openfoam.com/`.

[122] J. U. Brackbill, D. B. Kothe, and C. Zemach. A Continuum Method for Modeling Surface Tension. *J. Comput. Phys.*, 100:335–354, 1992.

[123] Š Šikalo, H. D. Wilhelm, I. V. Roisman, S. Jakirlić, and C. Tropea. Dynamic contact angle of spreading droplets: Experiments and simulations. *Phys. Fluids*, 17:062103, 2005.

[124] I. V. Roisman, L. Opfer, C. Tropea, M. Raessi, J. Mostaghimi, and S. Chandra. Drop impact onto a dry surface: Role of the dynamic contact angle. *Colloids Surfaces A*, 322:183–191, 2008.

[125] Auro Ashish Saha and Sushanta K. Mitra. Effect of dynamic contact angle in a volume of fluid (VOF) model for a microfluidic capillary flow. *J. Colloid Interface Sci.*, 339:461–480, 2009.

[126] Percival J. Graham, Mehran M. Farhangi, and Ali Dolatabadi. Dynamics of droplet coalescence in response to increasing hydrophobicity. *Phys. Fluids*, 24:112105, 2012.

[127] Jinliang Xu, Yuanyuan Chen, and Jian Xie. Non-dimensional numerical study of droplet impacting on heterogeneous hydrophilicity/hydrophobicity surface. *Int. J. Heat Mass Transf.*, 116:951–968, 2018.

[128] Richard L. Hoffman. A study of the advancing interface. I. Interface shape in liquid-gas systems. *J. Colloid Interface Sci.*, 50:228–241, 1975.

[129] R. I. Issa. Solution of the Implicitly Discretized Fluid Flow Equations by Operator Splitting. *J. Comput. Phys.*, 62:40–65, 1986.

[130] E. B. Dussan V. and S. H. Davis. Stability in systems with moving contact lines. *J. Fluid Mech.*, 173:115–130, 1986.

[131] Hu Luo, Yao Lu, Shaohui Yin, Shuai Huang, Jinlong Song, Faze Chen, Fengjun Chen, Claire J. Carmalt, and Ivan P. Parkin. Robust platform for water harvesting and directional transport. *J. Mater. Chem. A*, 6:5635–5643, 2018.

[132] A. L. Yarin. Drop impact dynamics: Splashing, spreading, receding, bouncing... *Annu. Rev. Fluid Mech.*, 38:159–192, 2006.

[133] D. C. Vadillo, A. Soucemarianadin, C. Delattre, and D. C. D. Roux. Dynamic contact angle effects onto the maximum drop impact spreading on solid surfaces. *Phys. Fluids*, 21:122002, 2009.

[134] M. Strani and F. Sabetta. Free vibrations of a drop in partial contact with a solid support. *J. Fluid Mech.*, 141:233–247, 1984.

[135] Robert W. Smithwick III and Joseph A. M. Boulet. Vibrations of Microscopic Mercury Droplets on Glass. *J. Colloid Interface Sci.*, 130:588–596, 1989.

[136] G. McHale, S. J. Elliott, M. I. Newton, D. L. Herbertson, and K. Esmer. Levitation-Free Vibrated Droplets: Resonant Oscillations of Liquid Marbles. *Langmuir*, 25:529–533, 2009.

[137] Chun-Ti Chang, J. B. Bostwick, Susan Daniel, and P. H. Steen. Dynamics of sessile drops. Part 2. Experiment. *J. Fluid Mech.*, 768:442–467, 2015.

[138] Yi Xia and Paul H. Steen. Moving contact-line mobility measured. *J. Fluid Mech.*, 841:767–783, 2018.

[139] Jean-Baptiste Dupont and Dominique Legendre. Numerical simulation of static and sliding drop with contact angle hysteresis. *J. Comput. Phys.*, 229: 2453–2478, 2010.

[140] Pengfei Hao, Cunjing Lv, Zhaohui Yao, and Feng He. Sliding behavior of water droplet on superhydrophobic surface. *Europhys. Lett.*, 90:66003, 2010.

[141] Gulraiz Ahmed, Mathieu Sellier, Mark Jermy, and Michael Taylor. Modeling the effects of contact angle hysteresis on the sliding of droplets down inclined surfaces. *Eur. J. Mech. B*, 48:218–230, 2014.

[142] Zhiping Yuan, Xiaomin Wu, Fuqiang Chu, and Renzhi Wu. Numerical simulations of guided self-propelled jumping of droplets on a wettability gradient surface. *Appl. Therm. Eng.*, 156:524–530, 2019.

[143] Kaixuan Zhang, Zhen Li, Martin Maxey, Shuo Chen, and George Em Karniadakis. Self-Cleaning of Hydrophobic Rough Surfaces by Coalescence-Induced Wetting Transition. *Langmuir*, 35:2431–2442, 2019.

[144] Xukun He, Lei Zhao, and Jiangtao Cheng. Coalescence-Induced Swift

Jumping of Nanodroplets on Curved Surfaces. *Langmuir*, 35:9979–9987, 2019.

[145] Mostafa Moradi, Mohammad Hassan Rahimian, and Seyed Farshid Chini. Coalescence-induced droplet detachment on low-adhesion surfaces: A three-phase system study. *Phys. Rev. E*, 99:063102, 2019.

[146] Shaokang Li, Fuqiang Chu, Jun Zhang, David Brutin, and Dongsheng Wen. Droplet jumping induced by coalescence of a moving droplet and a static one: Effect of initial velocity. *Chem. Eng. Sci.*, 211:115252, 2020.

[147] C. Zhang, A. C. M. Sousa, and J. E. S. Venart. The Numerical and Experimental Study of a Power Plant Condenser. *J. Heat Transf.*, 115:435–445, 1993.

[148] T. Humplik, J. Lee, S. C. O'Hern, B. A. Fellman, M. A. Baig, S. F. Hassan, M. A. Atieh, F. Rahman, T. Laoui, R. Karnik, and E. N. Wang. Nanostructured materials for water desalination. *Nanotechnology*, 22:292001, 2011.

[149] Jian Wang, Baolong Wang, Wei Wu, Xianting Li, and Wenxing Shi. Performance analysis of an absorption-compression hybrid refrigeration system recovering condensation heat for generation. *Appl. Therm. Eng.*, 108:54–65, 2016.

[150] J. W. Rose. Dropwise condensation theory and experiment: a review. *Proc. Inst. Mech. Eng. A*, 216:115–128, 2002.

[151] Daniel J. Preston and Evelyn N. Wang. Jumping Droplets Push the Boundaries of Condensation Heat Transfer. *Joule*, 2:205–207, 2018.

[152] Yoshio Utaka, Akio Saito, and Hiroyuki Yanagida. On the mechanism

determining the transition mode from dropwise to film condensation. *Int. J. Heat Mass Transf.*, 31:1113–1120, 1988.

[153] Eugene K. Ungar. Spacecraft Radiator Freeze Protection Using a Regenerative Heat Exchanger with Bypass Setpoint Temperature Control. In *38th International Conference on Environmental Systems*, 2008.

[154] Jentung Ku. Operating Characteristics of Loop Heat Pipes. In *29th International Conference on Environmental Systems*, 1999.

[155] Yu. F. Maydanik. Loop heat pipes. *Appl. Therm. Eng.*, 25:635–657, 2005.

[156] National Aeronautics and Space Administration. NASA Technology Roadmaps TA 14: Thermal Management Systems. Technical report, 2015.

[157] Yin-Ning Zhou, Jin-Jin Li, Qing Zhang, and Zheng-Hong Luo. Light-Responsive Smart Surface with Controllable Wettability and Excellent Stability. *Langmuir*, 30:12236–12242, 2014.

[158] Wei Xiong, Jefferson Zhe Liu, Zhi-Liang Zhang, and Quan-Shui Zhen. Control of surface wettability via strain engineering. *Acta Mech. Sin.*, 29: 543–549, 2013.

[159] Joerg Lahann, Samir Mitragotri, Thanh-Nga Tran, Hiroki Kaido, Jagannathan Sundaram, Insung S. Choi, Saskia Hoffer, Gabor A. Somorjai, and Robert Langer. A Reversibly Switching Surface. *Science*, 299:371–374, 2003.

[160] Ben Wang, Zhiguang Guo, and Weimin Liu. pH-responsive smart fabrics with controllable wettability in different surroundings. *RSC Adv.*, 4: 14684–14690, 2014.

[161] Joannis S. Scarpa, Delbert D. Mueller, and Irving M. Klotz. Slow Hydrogen-Deuterium Exchange in a Non-α-helical Polyamide. *J. Am. Chem. Soc.*, 89:6024–6030, 1967.

[162] M. Heskins and J. E. Guillet. Solution Properties of Poly(N-isopropylacrylamide). *J. Macromol. Sci. A*, 2:1441–1455, 1968.

[163] H. G. Schild. Poly(N-isopropylacrylamide): experiment, theory and application. *Prog. Polym. Sci.*, 17:163–249, 1992.

[164] Al de Leon and Rigoberto C. Advincula. Reversible Superhydrophilicity and Superhydrophobicity on a Lotus-Leaf Pattern. *ACS Appl. Mater. Interfaces*, 6:22666–22672, 2014.

[165] D. K. Owens and R. C. Wendt. Estimation of the Surface Free Energy of Polymers. *J. Appl. Polym. Sci.*, 13:1741–1747, 1969.

[166] Taolei Sun, Guojie Wang, Lin Feng, Biqian Liu, Yongmei Ma, Lei Jiang, and Daoben Zhu. Reversible Switching between Superhydrophilicity and Superhydrophobicity. *Angew. Chem. Int. Ed.*, 43:357–360, 2004.

[167] Shuanhong Ma, Xiaoqin Zhang, Bo Yu, and Feng Zhou. Brushing up functional materials. *NPG Asia Mater.*, 11:24, 2019.

[168] Y. Zhang, S. Sinha-Ray, and A. L. Yarin. Mechanoresponsive polymer nanoparticles, nanofibers and coatings as drug carriers and components of microfluidic devices. *J. Mater. Chem.*, 21:8269–8281, 2011.

[169] Baolong Xue, Longcheng Gao, Yongping Hou, Zhiwen Liu, and Lei Jiang. Temperature Controlled Water/Oil Wettability of a Surface Fabricated by a Block Copolymer: Application as a Dual Water/Oil On-Off Switch. *Adv. Mater.*, 25:273–277, 2013.

[170] Linnea K. Ista, Vićtor H. Peŕez-Luna, and Gabriel P. López. Surface-Grafted, Environmentally Sensitive Polymers for Biofilm Release. *Appl. Environ. Microbiol.*, 65:1603–1609, 1999.

[171] Youngsuk Nam and Y. Sungtaek Ju. A comparative study of the morphology and wetting characteristics of micro/nanostructured Cu surfaces for phase change heat transfer applications. *J. Adhes. Sci. Technol.*, 27:2163–2176, 2013.

[172] Soumyadip Sett, Peter Sokalski, Kalyan Boyina, Longnan Li, Kazi Fazle Rabbi, Harpreet Auby, Thomas Foulkes, Allison Mahvi, George Barac, Leslie W. Bolton, and Nenad Miljkovic. Stable Dropwise Condensation of Ethanol and Hexane on Rationally Designed Ultrascalable Nanostructured Lubricant-Infused Surfaces. *Nano Lett.*, 19:5287–5296, 2019.

[173] E. Hoque, J. A. DeRose, R. Houriet, P. Hoffmann, and H. J. Mathieu. Stable Perfluorosilane Self-Assembled Monolayers on Copper Oxide Surfaces: Evidence of Siloxy-Copper Bond Formation. *Chem. Mater.*, 19:798–804, 2007.

[174] Krzysztof Matyjaszewski, Hongchen Dong, Wojciech Jakubowski, Joanna Pietrasik, and Andy Kusumo. Grafting from Surfaces for "Everyone": ARGET ATRP in the Presence of Air. *Langmuir*, 23:4528–4531, 2007.

[175] Phanindhar Shivapooja, Linnea K. Ista, Heather E. Canavan, and Gabriel P. Lopez. ARGET-ATRP Synthesis and Characterization of PNIPAAm Brushes for Quantitative Cell Detachment Studies. *Biointerphases*, 7:1–9, 2012.

[176] Xue-Hu Ma, Xing-Dong Zhou, Zhong Lan, Yi-Ming Li, and Yu Zhang.

Condensation heat transfer enhancement in the presence of non-condensable gas using the interfacial effect of dropwise condensation. *Int. J. Heat Mass Transf.*, 51:1728–1737, 2008.

[177] S. Lee, S. U.-S. Choi, S. Li, and J. A. Eastman. Measuring Thermal Conductivity of Fluids Containing Oxide Nanoparticles. *J. Heat Transf.*, 121: 280–289, 1999.

[178] Volker Gnielinski. New equations for heat and mass transfer in turbulent pipes and channels. *Forsch. Ing. A*, 41:8–16, 1975.

[179] Abulimiti Aili, QiaoYu Ge, and TieJun Zhang. How Nanostructures Affect Water Droplet Nucleation on Superhydrophobic Surfaces. *J. Heat Transf.*, 139:112401, 2017.

[180] Emre Ölçeroğlu, Chia-Yun Hsieh, Kenneth K. S. Lau, and Matthew McCarthy. Thin Film Condensation Supported on Ambiphilic Microstructures. *J. Heat Transf.*, 139:020910, 2017.

[181] Bureau International des Poids et Mesures. Evaluation of measurement data — Guide to the expression of uncertainty in measurement. Technical report, 2008.

[182] W. Nusselt. Die Oberflächenkondensation des Wasserdampfes. *Z. Ver. Dtsch. Ing.*, 60:541–546 & 569–575, 1916.

[183] P. J. Marto, D. J. Looney, J. W. Rose, and A. S. Wanniarachchi. Evaluation of organic coatings for the promotion of dropwise condensation of steam. *Int. J. Heat Mass Transf.*, 29:1109– 1117, 1986.

[184] Yiyun Zhang and Alexander L. Yarin. Stimuli-responsive copolymers of n-isopropyl acrylamide with enhanced longevity in water for micro- and

nanofluidics, drug delivery and non-woven applications. *J. Mater. Chem.*, 19:4732–4739, 2009.

[185] Y. Takata, S. Hidaka, J. M. Cao, T. Nakamura, H. Yamamoto, M. Masuda, and T. Ito. Effect of surface wettability on boiling and evaporation. *Energy*, 30:209–220, 2005.

[186] Marieke Ahlers, Alexander Buck-Emden, and Hans-Jörg Bart. Is dropwise condensation feasible? A review on surface modifications for continuous dropwise condensation and a profitability analysis. *J. Adv. Res.*, 16:1–13, 2019.

[187] Bachir El Fil, Girish Kini, and Srinivas Garimella. A review of dropwise condensation: Theory, modeling, experiments, and applications. *Int. J. Heat Mass Transf.*, 160:120172, 2020.

[188] Daniele Torresin, Manish K. Tiwari, Davide Del Col, and Dimos Poulikakos. Flow Condensation on Copper-Based Nanotextured Superhydrophobic Surfaces. *Langmuir*, 29:840–848, 2013.

[189] Adam T. Paxson, Jose L. Yagüe, Karen K. Gleason, and Kripa K. Varanasi. Stable Dropwise Condensation for Enhancing Heat Transfer via the Initiated Chemical Vapor Deposition (iCVD) of Grafted Polymer Films. *Adv. Mater.*, 26:418–423, 2014.

[190] Daniel J. Preston, Daniela L. Mafra, Nenad Miljkovic, Jing Kong, and Evelyn N. Wang. Scalable Graphene Coatings for Enhanced Condensation Heat Transfer. *Nano Lett.*, 15:2902–2909, 2015.

[191] J. Zhu, Y. Luo, J. Tian, J. Li, and X. Gao. Clustered ribbed-nanoneedle structured copper surfaces with high-efficiency dropwise condensation

heat transfer performance. *ACS Appl. Mater. Interfaces*, 7:10660–10665, 2015.

[192] Benli Peng, Xuehu Ma, Zhong Lan, Wei Xu, and Rongfu Wen. Experimental investigation on steam condensation heat transfer enhancement with vertically patterned hydrophobichydrophilic hybrid surfaces. *Int. J. Heat Mass Transf.*, 83:27–38, 2015.

[193] Rongfu Wen, Qian Li, Jiafeng Wu, Gensheng Wu, Wei Wang, Yunfei Chen, Xuehu Ma, Dongliang Zhao, and Ronggui Yang. Hydrophobic copper nanowires for enhancing condensation heat transfer. *Nano Energy*, 33: 177–183, 2017.

[194] Rongfu Wen, Shanshan Xu, Dongliang Zhao, Yung-Cheng Lee, Xuehu Ma, and Ronggui Yang. Hierarchical Superhydrophobic Surfaces with Micropatterned Nanowire Arrays for High-Efficiency Jumping Droplet Condensation. *ACS Appl. Mater. Interfaces*, 9:44911–44921, 2017.

[195] Steve Q. Cai and Avijit Bhunia. Superhydrophobic Condensation Enhanced by Conical Hierarchical Structures. *J. Phys. Chem. C*, 121:10047–10052, 2017.

[196] Shufen Wang, Minsu Liu, Yuan Feng, Yanru Bu, So Hung Huynh, Tuck Wah Ng, Feng Gu, Aibing Yu, and Xuchuan Jiang. Bioinspired hierarchical copper oxide surfaces for rapid dropwise condensation. *J. Mater. Chem. A*, 5:21422–21428, 2017.

[197] Riccardo Parin, Alessandro Martucci, Marco Sturaro, Stefano Bortolin, Marco Bersani, Francesco Carraro, and Davide Del Col. Nano-structured

aluminum surfaces for dropwise condensation. *Surf. Coat. Tech.*, 348:1–12, 2018.

[198] Chander Shekhar Sharma, Christos Stamatopoulos, Reto Suter, Philipp Rudolf von Rohr, and Dimos Poulikakos. Rationally 3D-Textured Copper Surfaces for Laplace Pressure Imbalance-Induced Enhancement in Dropwise Condensation. *ACS Appl. Mater. Interfaces*, 10: 29127–29135, 2018.

[199] Yong Jin, Adnan Qamar, Yusuf Shi, and Peng Wang. Preferential water condensation on superhydrophobic nano-cones array. *Appl. Phys. Lett.*, 113:211601, 2018.

[200] Jaehwan Shim, Donghyun Seo, Seungtae Oh, Jinki Lee, and Youngsuk Nam. Condensation Heat Transfer Performance of Thermally Stable Superhydrophobic Cerium Oxide Surfaces. *ACS Appl. Mater. Interfaces*, 10: 31765–31776, 2018.

[201] Qi Peng, Li Jia, Jian Guo, Chao Dang, Yi Ding, Liaofei Yin, and Qiao Yan. Forced jumping and coalescence-induced sweeping enhanced the dropwise condensation on hierarchically microgrooved superhydrophobic surface. *Appl. Phys. Lett.*, 114:133106, 2019.

[202] D. Venkata Krishnan, G. Udaya Kumar, S. Suresh, M. Jubal, M. R. Thansekhar, and Ravi Ramesh. Wetting transition in laser-fabricated hierarchical surface structures and its impact on condensation heat transfer characteristics. *Int. J. Heat Mass Transf.*, 140:886–896, 2019.

[203] Jian Xie, Jinliang Xu, Xiang Li, and Huan Liu. Dropwise condensation

on superhydrophobic nanostructure surface, Part I: Long-term operation and nanostructure failure. *Int. J. Heat Mass Transf.*, 129:86–95, 2019.

[204] Dae-Yun Ji, Jeong-Won Lee, Woonbong Hwang, and Kwon-Yeong Lee. Experimental study of condensation heat transfer on a horizontal aluminum tube with superhydrophobic characteristic. *Int. J. Heat Mass Transf.*, 134:286–295, 2019.

[205] Yaqi Cheng, Bingang Du, Kai Wang, Yansong Chen, Zhong Lan, Zuankai Wang, and Xuehu Ma. Macrotextures-induced jumping relay of condensate droplets. *Appl. Phys. Lett.*, 114:093704, 2019.

[206] Taeyang Han, Ho Jae Kwak, Jong Hyun Kim, Jeong-Tae Kwon, and Moo Hwan Kim. Nanograssed Zigzag Structures To Promote Coalescence-Induced Droplet Jumping. *Langmuir*, 35:9093–9099, 2019.

[207] Xiaotong Chen, Peng Wang, and Dun Zhang. Designing a Superhydrophobic Surface for Enhanced Atmospheric Corrosion Resistance Based on Coalescence-Induced Droplet Jumping Behavior. *ACS Appl. Mater. Interfaces*, 11:38276–38284, 2019.

[208] Yizhou Shen, Yuehan Xie, Jie Tao, Haifeng Chen, Chunling Zhu, Mingming Jin, and Yang Lu. Rationally design nanostructure features on superhydrophobic surfaces for enhancing self-propelling dynamics of condensed droplets. *ACS Sustainable Chem. Eng.*, 7:2702–2708, 2019.

[209] Xiaochen Ma, Yang Wang, Heting Wu, Yuanhao Wang, and Ya Yang. Efficient water scavenging by cooling superhydrophobic surfaces to obtain jumping water droplets from air. *Sci. Rep.*, 9:13784, 2019.

[210] Sushant Anand, Adam T. Paxson, Rajeev Dhiman, J. David Smith, and Kripa K. Varanasi. Enhanced Condensation on Lubricant-Impregnated Nanotextured Surfaces. *ACS Nano*, 6:10122–10129, 2012.

[211] Rong Xiao, Nenad Miljkovic, Ryan Enright, and Evelyn N. Wang. Immersion Condensation on Oil-Infused Heterogeneous Surfaces for Enhanced Heat Transfer. *Sci. Rep.*, 3:1988, 2013.

[212] Konrad Rykaczewski, Adam T. Paxson, Matthew Staymates, Marlon L. Walker, Xiaoda Sun, Sushant Anand, Siddarth Srinivasan, Gareth H. McKinley, Jeff Chinn, John Henry J. Scott, and Kripa K. Varanasi. Dropwise Condensation of Low Surface Tension Fluids on Omniphobic Surfaces. *Sci. Rep.*, 4:4158, 2014.

[213] Patricia B. Weisensee, Yunbo Wanga, Qian Hongliang, Daniel Schultz, William P. King, and Nenad Miljkovic. Condensate droplet size distribution on lubricant-infused surfaces. *Int. J. Heat Mass Transf.*, 109:187–199, 2017.

[214] Hirotaka Tsuchiya, Mizuki Tenjimbayashi, Takeo Moriya, Ryohei Yoshikawa, Kaichi Sasaki, Ryo Togasawa, Taku Yamazaki, Kengo Manabe, and Seimei Shiratori. Liquid-Infused Smooth Surface for Improved Condensation Heat Transfer. *Langmuir*, 33:8950–8960, 2017.

[215] Daniel J. Preston, Zhengmao Lu, Youngsup Song, Yajing Zhao, Kyle L. Wilke, Dion S. Antao, Marcel Louis, and Evelyn N. Wang. Heat Transfer Enhancement During Water and Hydrocarbon Condensation on Lubricant Infused Surfaces. *Sci. Rep.*, 8:540, 2018.

[216] Hiroaki Tanaka. Measurements of Drop-Size Distributions During Transient Dropwise Condensation. *J. Heat Transfer*, 97:341–346, 1975.

[217] Van P. Carey. *Liquid-Vapor Phase Change Phenomena*. Hemisphere Publishing Company, 1992.

[218] Leon R. Glicksman and Andrew W. Hunt. Numerical Simulation of Dropwise Condensation. *Int. J. Heat Mass Transf.*, 15:2251–2269, 1972.

[219] Joseph W Krumpfer and Thomas J McCarthy. Contact angle hysteresis: a different view and a trivial recipe for low hysteresis hydrophobic surfaces. *Faraday Discuss.*, 146:103–111, 2010.

[220] Ryan Enright, Nenad Miljkovic, Ahmed Al-Obeidi, Carl V. Thompson, and Evelyn N. Wang. Condensation on Superhydrophobic Surfaces: The Role of Local Energy Barriers and Structure Length Scale. *Langmuir*, 28: 14424–14432, 2012.

[221] David Quéré. Non-sticking drops. *Reports Prog. Phys.*, 68:2495–2532, 2005.

[222] Ross Lundy, Conor Byrne, Justin Bogan, Kevin Nolan, Maurice N. Collins, Eric Dalton, and Ryan Enright. Exploring the Role of Adsorption and Surface State on the Hydrophobicity of Rare Earth Oxides. *ACS Appl. Mater. Interfaces*, 9:13751–13760, 2017.

[223] Keong Yong, Ali Ashraf, Pilgyu Kang, and SungWoo Nam. Rapid Stencil Mask Fabrication Enabled One-Step Polymer-Free Graphene Patterning and Direct Transfer for Flexible Graphene Devices. *Sci. Rep.*, 6:24890, 2016.

[224] S. A. Stylianou and J. W. Rose. Drop-to-Filmwise Condensation Transition: Heat Transfer Measurements for Ethanediol. *Int. J. Heat Mass Transf.*, 26:747–760, 1983.

[225] Xuehu Ma, Dunqi Xu, and Jifang Lin. Catastrophe characteristics of the condensation and pool boiling phenomena. *Int. J. Heat Mass Transf.*, 37: 533–535, 1994.

[226] Xuehu Ma, John W. Rose, Dunqi Xu, Jifang Lin, and Buxuan Wang. Advances in dropwise condensation heat transfer: Chinese research. *Chem. Eng. J.*, 78:87–93, 2000.

[227] N. H. Fletcher. Size Effect in Heterogeneous Nucleation. *J. Chem. Phys.*, 29:572–576, 1958.

[228] L. H. Chai and M. Shoji. Boiling curves – bifurcation and catastrophe. *Int. J. Heat Mass Transf.*, 44:4175–4179, 2001.

[229] Chun Huh and L. E. Scriven. Hydrodynamic Model of Steady Movement of a Solid/Liquid/Fluid Contact Line. *J. Colloid Interface Sci.*, 35:85–101, 1971.

[230] Elizabeth B. Dussan V. and Stephen H. Davis. On the motion of a fluid-fluid interface along a solid surface. *J. Fluid Mech.*, 65:71–95, 1974.

[231] O. V. Voinov. Hydrodynamics of wetting. *Fluid Dyn.*, 11:714–721, 1976.

[232] C. Huh and S. G. Mason. The steady movement of a liquid meniscus in a capillary tube. *J. Fluid Mech.*, 81:401–419, 1977.

[233] John A. Marsh, S. Garoff, and E. B. Dussan V. Dynamic Contact Angles and Hydrodynamics near a Moving Contact Line. *Phys. Rev. Lett.*, 70: 2778–2781, 1993.

[234] Anne-Laure Biance, Christophe Clanet, and David Quéré. First steps in the spreading of a liquid droplet. *Phys. Rev. E*, 69:016301, 2004.

[235] James C. Bird, Shreyas Mandre, and Howard A. Stone. Short-Time Dynamics of Partial Wetting. *Phys. Rev. Lett.*, 100:234501, 2008.

[236] Koen G. Winkels, Joost H. Weijs, Antonin Eddi, and Jacco H. Snoeijer. Initial spreading of low-viscosity drops on partially wetting surfaces. *Phys. Rev. E*, 85:055301(R), 2012.

[237] Michael E. Clarke, Annie Xia, Joseph Smith, and Bipin Parekh. Point-of-use ultra-pure water for immersion lithography. In *IEEE/SEMI 17th Annual Advanced Semiconductor Manufacturing Conference*, pages 238–243, 2006.

[238] Paul H. Steen and Christian Karcher. Fluid Mechanics of Spin Casting of Metals. *Annu. Rev. Fluid Mech.*, 29:373–397, 1997.

[239] Yi Sui, Hang Ding, and Peter D.M. Spelt. Numerical Simulations of Flows with Moving Contact Lines. *Annu. Rev. Fluid Mech.*, 46:97–119, 2014.

[240] J. B. Bostwick and P. H. Steen. Dynamics of sessile drops. Part 1. Inviscid theory. *J. Fluid Mech.*, 760:5–38, 2014.

[241] Stephen H. Davis. Moving contact lines and rivulet instabilities. Part 1. The static rivulet. *J. Fluid Mech.*, 98:225–242, 1980.

[242] L. M. Hocking. The damping of capillary-gravity waves at a rigid boundary. *J. Fluid Mech.*, 179:253–266, 1987.

[243] D. V. Lyubimov, T. P. Lyubimova, and S. V. Shklyaev. Non-Axisymmetric Oscillations of a Hemispherical Drop. *Fluid Dyn.*, 39:851–862, 2004.

[244] Irina S. Fayzrakhmanova and Arthur V. Straube. Stick-slip dynamics of an oscillated sessile drop. *Phys. Fluids*, 21:072104, 2009.

[245] J. B. Bostwick and P. H. Steen. Coupled oscillations of deformable spherical-cap droplets. Part 1. Inviscid motions. *J. Fluid Mech.*, 714:312–335, 2013.

[246] Chun-Ti Chang, Joshua B. Bostwick, Paul H. Steen, and Susan Daniel. Substrate constraint modifies the Rayleigh spectrum of vibrating sessile drops. *Phys. Rev. E*, 88:023015, 2013.

[247] J. B. Bostwick and P. H. Steen. Stability of Constrained Capillary Surfaces. *Annu. Rev. Fluid Mech.*, 47:539–568, 2015.

[248] M. M. Weislogel and S. Lichter. Water Balloon Rupture in Low-G. *Phys. Fluids*, 10:S4, 1998.

[249] Chien Ting Chin, Charles Lancée, Jerome Borsboom, Frits Mastik, Martijn E. Frijlink, Nico de Jong, Michel Versluis, and Detlef Lohse. Brandaris 128: A digital 25 million frames per second camera with 128 highly sensitive frames. *Rev. Sci. Instrum.*, 74:5026–5034, 2003.

[250] Michel Versluis. High-speed imaging in fluids. *Exp. Fluids*, 54:1458, 2013.

[251] Claas Willem Visser, Philipp Erhard Frommhold, Sander Wildeman, Robert Mettin, Detlef Lohse, and Chao Sun. Dynamics of high-speed micro-drop impact: numerical simulations and experiments at frame-to-frame times below 100 ns. *Soft Matter*, 11:1708–1722, 2015.

[252] Taewoong Lim, Sewoon Han, Jaewon Chung, Jin Taek Chung, Seunghwan Ko, and Costas P. Grigoropoulos. Experimental study on spreading and evaporation of inkjet printed pico-liter droplet on a heated substrate. *Int. J. Heat Mass Transf.*, 52:431–441, 2009.

[253] Lee Hulse-Smith and Mike Illes. A Blind Trial Evaluation of a Crime Scene Methodology for Deducing Impact Velocity and Droplet Size from Circular Bloodstains. *J. Forensic Sci.*, 52:65–69, 2007.

[254] Lawrence E. Murr and Wayne L. Johnson. 3D metal droplet printing development and advanced materials additive manufacturing. *J. Mater. Res. Technol.*, 6:77–89, 2017.

[255] Arun Kumar Gnanappa, Evangelos Gogolides, Fabrizio Evangelista, and Michel Riepen. Contact line dynamics of a superhydrophobic surface: application for immersion lithography. *Microfluid Nanofluid*, 10:1351–1357, 2011.

[256] Ryusuke Hasegawa and Daichi Azuma. Impacts of amorphous metal-based transformers on energy efficiency and environment. *J. Magn. Magn. Mater.*, 320:2451–2456, 2008.

[257] Jeffrey M. Aristoff, Tadd T. Truscott, Alexandra H. Techet, and John W. M. Bush. The water entry of decelerating spheres. *Phys. Fluids*, 22:032102, 2010.

[258] Michael D. Cloeter, Kuide Qin, Pramod Patil, and Billy Smith. Planar Laser Induced Fluorescence (PLIF) Flow Visualization applied to Agricultural Spray Nozzles with Sheet Disintegration; Influence of an Oil-in-Water Emulsion. In *ILASS-Americas 22nd Annual Conference on Liquid Atomization and Spray Systems*, 2010.

[259] Steven H. Collicott, William G. Lindsley, and David G. Frazer. Zero-gravity liquid-vapor interfaces in circular cylinders. *Phys. Fluids*, 18: 087109, 2006.

[260] Jan Genzer and Abraham Marmur. Biological and Synthetic Self-Cleaning Surfaces. *MRS Bull.*, 33:742–746, 2008.

[261] Michael J. Vogel and Paul H. Steen. Capillarity-based switchable adhesion. *Proc. Natl. Acad. Sci. U.S.A.*, 107:3377–3381, 2010.

[262] Dileep Mampallil and Sajan D. George. Microfluidics — a lab in your palm. *Resonance*, 17:682–690, 2012.

[263] R. G. Cox. The dynamics of the spreading of liquids on a solid surface. Part 1. Viscous flow. *J. Fluid Mech.*, 168:169–194, 1986.

[264] T. D. Blake and J. M. Haynes. Kinetics of Liquid/Liquid Displacement. *J. Colloid Interface Sci.*, 30:421–423, 1969.

[265] Peter G. Petrov and Jordan G. Petrov. A Combined Molecular-Hydrodynamic Approach to Wetting Kinetics. *Langmuir*, 8:1762–1767, 1992.

[266] Johan Göhl, Andreas Mark, Srdjan Sasic, and Fredrik Edelvik. An immersed boundary based dynamic contact angle framework for handling complex surfaces of mixed wettabilities. *Int. J. Multiph. Flow*, 109:164–177, 2018.

[267] Abhay Borkar and John Tsamopoulos. Boundary-layer analysis of the dynamics of axisymmetric capillary bridges. *Phys. Fluids A*, 3:2866–2874, 1991.

[268] A. Carlson, G. Bellani, and G. Amberg. Contact line dissipation in short-time dynamic wetting. *Europhys. Lett.*, 97:44004, 2012.

[269] Paul H. Steen and Yi Xia. Resonantly-driven drop contact-line mobility measurement, United States Patent Application US 2019/0025177 A1, January 24, 2019.

[270] V. A. Ogarev, T. N. Timonina, V. V. Arslanov, and A. A. Trapeznikov. Spreading of Polydimethylsiloxane Drops on Solid Horizontal Surfaces. *J. Adhes.*, 6:337–355, 1974.

[271] L. H. Tanner. The spreading of silicone oil drops on horizontal surfaces. *J. Phys. D*, 12:1473–1484, 1979.

[272] J. K. Carpenter and P. H. Steen. Planar-flow spin-casting of molten metals: process behaviour. *J. Mater. Sci.*, 27:215–225, 1992.

[273] J.-C. Fernández-Toledano, T. D. Blake, and J. De Coninck. Moving contact lines and Langevin formalism. *J. Colloid Interface Sci.*, 562:287–292, 2020.

[274] Frank Pyrtle, III. *Vibration Induced Droplet Generation from a Liquid Layer for Evaporative Cooling in a Heat Transfer Cell*. PhD thesis, Georgia Institute of Technology, 2005.

[275] Vikram Pratap, Nadjoua Moumen, and R. Shankar Subramanian. Thermocapillary Motion of a Liquid Drop on a Horizontal Solid Surface. *Langmuir*, 24:5185–5193, 2008.

[276] Yongping Chen, C. B. Sobhan, and G. P. Peterson. Review of Condensation Heat Transfer in Microgravity Environments. *J. Thermophys. Heat Transf.*, 20:353–360, 2006.

[277] Frank P. Incropera, David P. DeWitt, Theodore L. Bergman, and Adrienne S. Lavine. *Fundamentals of Heat and Mass Transfer, Sixth Edition*. John Wiley & Sons, 2006.

[278] Kai-Jian Liu, Yu-Ling Fu, Long-Yong Xie, Chao Wu, Wei-Bao He, Sha Peng, Zheng Wang, Wen-Hu Bao, Zhong Cao, Xinhua Xu, and Wei-Min He. Green and Efficient: Oxidation of Aldehydes to Carboxylic Acids and Acid Anhydrides with Air. *ACS Sustain. Chem. Eng.*, 6:4916–4921, 2018.

[279] Y. D. Shikhmurzaev. The moving contact line on a smooth solid surface. *Int. J. Multiph. Flow*, 19:589–610, 1993.

[280] Yulii D. Shikhmurzaev. Mathematical modeling of wetting hydrodynamics. *Fluid Dyn. Res.*, 13:45–64, 1994.

[281] Yulii D. Shikhmurzaev. Moving contact lines in liquid/liquid/solid systems. *J. Fluid Mech.*, 334:211–249, 1997.

[282] J. Fukai, Y. Shiiba, T. Yamamoto, O. Miyatake, D. Poulikakos, C. M. Megaridis, and Z. Zhao. Wetting effects on the spreading of a liquid droplet colliding with a flat surface: Experiment and modeling. *Phys. Fluids*, 7:236–247, 1995.

[283] Yulii D. Shikhmurzaev. Singularities at the moving contact line. Mathematical, physical and computational aspects. *Physica D*, 217:121–133, 2006.